COPING WITH SCATTER IN GALAXY CLUSTER SCALING RELATIONSHIPS

By

David A. Ventimiglia

A DISSERTATION

Submitted to
Michigan State University
in partial fulfillment of the requirements
for the degree of

DOCTOR OF PHILOSOPHY

Astrophysics and Astronomy

2012

ABSTRACT

COPING WITH SCATTER IN GALAXY CLUSTER SCALING RELATIONSHIPS

By

David A. Ventimiglia

Galaxy clusters exhibit regular scaling relations among their bulk properties, establishing vital links between halo mass and cluster observables. Therefore, precision cosmology studies depending on these links benefit from a better understanding of scatter in the mass-observable scaling relations. Here, we study the role of merger processes in introducing scatter into the mass-temperature (M-T_X) relation, using a sample of 121 galaxy clusters simulated with radiative cooling and supernova feedback, along with three morphological statistics previously proposed to measure X-ray surface brightness substructure. These are the centroid variation (w), the axial ratio (η), and the power ratios (P_{20}) and P_{30}). We also examine spectral statistics which do not require imaging. In particular we look at the ratio of hardband to broadband spectral-fit temperatures T_{HBR}, which is a measure of temperature inhomogeneity inferred from X-ray spectral properties. We find that in this set of simulated clusters, each substructure measure is correlated with a cluster's departures $\delta \ln T$ and $\delta \ln M$ from the mean M-T_X relation, both for emission-weighted temperatures T_{EW} and for spectroscopic-like temperatures T_{SL}, in the sense that clusters with more substructure tend to be cooler at a given halo mass. In all cases, a three-parameter fit to the M-T_X relation that includes substructure information has less scatter than a two-parameter fit to the basic M-T_X relation. In this work we also test the effectiveness of T_{HBR} as a measure of scatter using the 118 galaxy clusters from our sample for which we have simulated X-ray images using the X-MAS software. We find that, while T_{HBR} is correlated with clusters' departures $\delta \ln M$ from the mean M-T_X relation, the effect is modest. Finally, we present the CosmoSurvey software for efficiently evaluating simple flux-limited galaxy cluster survey models on commodity hardware, and discuss possible extensions.

To my parents, Patricia Jane and Phillip Anthony Ventimiglia, whose love and sacrifice are the source of their children's accomplishments.

ACKNOWLEDGMENTS

I would like to thank my advisor, Dr. G. Mark Voit, for his wisdom, his humor, and his incredible patience. I could not have asked for a better mentor, and whatever credit derives from this small accomplishment goes to him. Thanks, Mark.

TABLE OF CONTENTS

LIST OF TABLES

LIST OF FIGURES

Chapter 1

Introduction

Astronomers have known about clusters of galaxies for almost as long as they have known about galaxies. Though of course its roots stretch much deeper into the past, one could defensibly locate the birth of modern astronomy, like much of the physical sciences, in the Enlightenment of the eighteenth century. And by the end of that century astronomers like Charles Messier and William Herschel had noticed that galaxies, whatever they were, were concentrated in particular regions of the sky. As astronomy was placed on firm observational grounds in the nineteenth and twentieth centuries, galaxy clusters were added to the list of exotic celestial beasts to be cataloged, indexed, and studied. In the modern era, George Abell [Abell(1958)] defined what it means to identify a galaxy cluster, how to catalog them, and how to describe their relevant properties. Of course this was the era when "optical astronomy" *was* astronomy, so understandably the key observational property Abell identified for galaxy clusters was their "optical richness", i.e. simple a number count of the galaxies in a cluster, within certain constraints. Since then, galaxy clusters have been observed and cataloged in a variety of other ways, and especially in the X-ray band.

With the first generation of space-based astronomical observing platforms in the late 1960s and early 1970s, it became possible to see astrophysical phenomena in wave-bands that are absorbed by the Earth's atmosphere. The UHURU satellite (1970) was the first X-ray observing satellite, and quickly it was used to identify luminous diffuse X-ray emission from galaxy clusters [Forman et al.(1972)]. Since then, space-based X-ray observations have become one of the most productive ways to measure the important properties of galaxy clusters. This is especially true since the X-ray emission now is identified with thermal emission from a hot diffuse plasma that envelopes a galaxy cluster and dominates its non-Dark Matter mass.

Nowadays, galaxy clusters are being observed in greater and greater detail in the X-ray and other bands, and their numbers are being counted in surveys with greater and greater reach. They now provide one of the pillars of modern observational cosmology and will be critical in understanding Dark Energy. Dark Energy is the mysterious form of energy that dominates the contents of the Universe at the present epoch and is driving an accelerating Universal expansion. The characteristics of Dark Energy—its abundance, its evolution, and its equation of state, for instance—modulate the growth of structure in the Universe, and in particular, the Dark Matter halos that are the sites of galaxy and galaxy cluster formation. In this way, the population characteristics of galaxy clusters, especially their distribution in mass and that distribution's evolution with cosmic time, are critically linked to global properties of the Universe. This is why observing and measuring galaxy clusters is so important and exciting to modern cosmology.

A key feature in any such endeavors is measuring the mass of galaxy clusters. Like distance, measuring the mass of any astrophysical object is often a dicey proposition, and it is especially true of galaxy clusters. Like we do with other objects, we must infer a galaxy cluster's mass by relating it to its observable properties, such as its overall luminosity, the velocity dispersion of its galaxies, etc. While the theoretical understanding of the structure and dynamics of all the components of a galaxy cluster is indeed an exciting and important area of research, the corollary is that our understanding of the ways their properties relate is still evolving. Typically, we rely on simple scaling relationships between the observable properties of a galaxy cluster and its mass, bolstered by a theoretical foundation which, while incomplete, supports and explains the existence of these scaling relationships. The details we elide in this process inevitably introduce the notion of “scatter”.

At any given mass, observed clusters will be scattered across a distribution in any particular observable property, such as luminosity. Naturally, some of that is introduced in the act of observing. What this work focuses on is intrinsic scatter, which arises in part from the deficit in our understanding of how galaxy formation occurs, how clusters are assembled, and what role feedback processes play. As our models increase in sophistication and accuracy, intrinsic scatter simply becomes a feature of those models, but some always remains.

In this work, we look at two related ways of coping with scatter in galaxy cluster scaling relationships. We also present software to aid in the modeling of scatter in these scaling relationships and the effects it has on the kinds of large surveys of galaxy clusters that are being developed.

Chapter 2 of this work presents the results of a research program designed to evaluate the efficacy of galaxy cluster substructure in measuring scatter. Galaxy clusters come in a wide variety of shapes, ranging from relaxed spheres to very irregular aggregations of knots, lumps, and filaments, exhibiting the effects of energetic merging events and feedback processes. We adopt several methods of quantifying the morphological irregularity—or “substructure”—of galaxy clusters and apply it to a sample selected from a large-volume hydrodynamical simulation of a portion of the Universe. The particular component of the cluster whose substructure we are observing is the surface-brightness of the X-ray emission from the luminous intra-cluster medium (ICM). The virtue of simulations in this context is that we know the mass of the galaxy clusters precisely. In this controlled environment, we then measure the effectiveness of substructure as an approach to obtain more accurate mass estimates in cluster surveys. Chapter 2 is adapted from [Ventimiglia et al.(2008)], where the results of this research program first were published by this author.

Chapter 3 of this work presents the results of another, similar research program, designed to evaluate the efficacy of galaxy cluster temperature inhomogeneity in measuring scatter. As introduced above and discussed in subsequent chapters, the intra-cluster medium (ICM) is the diffuse, hot plasma that permeates a galaxy cluster and dominates its non-Dark Matter mass. While in chapter 2 we measure the morphological substructure of this gas, via imaging of its X-ray emission, in chapter 3 we measure the thermal substructure of this gas, via spectroscopy of that X-ray emission. This provides another, complementary way of, in principle, measuring and correcting for scatter in mass-observable scaling relationships. Again, we use the same sample of simulated clusters as in chapter 2, adopting several methods of quantifying thermal irregularity—or "inhomogeneity"—of galaxy clusters. We then measure their effectiveness in obtaining more accurate galaxy cluster mass estimates. Chapter 3 also is adapted from a journal article by this author [Ventimiglia et al.(2012)].

Chapter 4 of this work presents software for modeling the kinds of flux-limited large-area galaxy cluster surveys upon which the corrections discussed in the previous chapters would be brought to bear. Techniques for measuring and correcting for scatter are important, but it also is important to understand the effect that scatter ultimately will have on the cosmological goals of the planned surveys. After all, with an appropriate model for scatter and with large enough number statistics, scaling-relationship scatter could be "self-calibrated" in the model without resorting to other observables like substructure or temperature inhomogeneity. Making those judgments will require extensive modeling, numerical simulations, the application of Monte Carlo Markov Chain (MCMC) methods, etc. And that, in turn, will require fast, efficient, lightweight galaxy cluster survey models that are easily adapted. We present one first step in this direction, with the CosmoSurvey program and library. Chapter 4 largely deals with the theoretical underpinnings of CosmoSurvey's cosmological, structure, and survey models, and can serve in someways as a general introduction to these concepts. Finally, chapter 5 summarizes the results of this work and introduces possible next steps.

Chapter 2

Substructure and Scatter in the Mass-Temperature Relations of Simulated Clusters

2.1 Introduction

Clusters of galaxies play a critical role in our understanding of the Universe and its history and are potentially powerful tools for conducting precision cosmology. For example, large cluster surveys can discriminate between cosmological models with different dark-energy equations of state by providing complementary observations of the shape of the cluster mass function, evolution in the number density of clusters with redshift, and bias in the spatial distribution of clusters [Wang & Steinhardt(1998), Levine et al.(2002), Hu(2003), Majumdar & Mohr(2004), Voit(2005)]. However, this potential to put tight constraints on the properties of dark energy will be realized only if we can accurately measure the masses of clusters and can precisely characterize the scatter in our mass measurements.

Scatter in X-ray cluster properties is directly related to substructure in the intracluster medium. If clusters were all structurally similar, then there would be a one-to-one relationship between halo mass and any given observable property. Generally speaking, deviations from a mean mass-observable relationship are attributed to structural differences among clusters. One kind of structural difference is the presence or absence of a cool core, in which the central cooling time is less than the Hubble time at the cluster's redshift, and the prominence of a cool core is observed to be a source of scatter in scaling relationships [Fabian et al.(1994)]. We also expect structural differences to arise from substructure in the dark matter, galaxy, and gas distributions. For instance, there may be a spread in halo concentration at a given mass, variations in the incidence of gas clumps, differences in the level of AGN feedback, or various effects due to mergers. All of these deviations can be considered forms of substructure that produce scatter in the mass-observable relations one would like to use for cosmological purposes. While it may ultimately be possible to constrain the amount of scatter and its evolution with redshift using self-calibration techniques [Lima & Hu(2005)], such constraints would be improved by prior knowledge about the relationship between scatter and substructure.

Traditionally, the most worrisome form of substructure has been that due to the effects of merger events. Clusters are often identified as "relaxed" or "unrelaxed", with the former assumed to be nearly in hydrostatic equilibrium and the latter suspected of being far from equilibrium. Cosmological simulations of clusters indicate that the truth is somewhere in between. The cluster population as a whole appears to follow well-defined virial relations with log-normal scatter around the mean, showing that clusters do not cleanly separate into relaxed and unrelaxed systems [Evrard et al.(2008)]. Even the most relaxed-looking clusters are not quite in hydrostatic equilibrium [Kravtsov et al.(2006)]. Instead of simply being "relaxed" or "unrelaxed," clusters occupy a continuum of relaxation levels determined by their recent mass-accretion history.

Quantifying this continuum of relaxation offers opportunities for reducing scatter in the mass-observable relations. If mergers are indeed responsible for much of the observed scatter around a given scaling relation, then there may be correlations between a cluster's morphology and its degree of deviation from the mean relation. Once one identifies a morphological parameter that correlates with the degree of deviation, one can construct a new mass-observable relation with less scatter by including the morphological parameter in the relation. Such an approach would be analogous to the improvement of Type Ia supernovae as distance indicators by using light-curve stretch as a second parameter to indicate the supernova's luminosity [Phillips(1993), Riess et al.(1996)].

Here we investigate how merger-related substructure in simulated clusters affects the relationship between a simulated cluster's mass and the temperature of its intracluster medium, building upon [Buote & Tsai(1995)] and [O'Hara et al.(2006a)]. [Buote & Tsai(1995)] quantified the morphologies and dynamical states of observed clusters and found structure measures to be an indicator of the dynamical state of a cluster. [O'Hara et al.(2006a)] also examined morphological measurements, for both observed and simulated clusters, and found that simulations without cooling showed no correlation between substructure and scaling relation scatter. In this work we examine substructure for simulated clusters with radiative cooling and focus on the idea that merger processes introduce intrinsic scatter into the M-T_{X} relationship by displacing clusters in the M-T_{X} plane away from the mean X-ray temperature $\langle T_{\mathrm{X}} \rangle |_M$ at a given mass M, either to higher or lower average ICM temperature. We then adopt a set of statistics [Buote & Tsai(1995), O'Hara et al.(2006a)] for quantifying galaxy cluster substructure and merger activity in order to investigate this hypothesis. Section 2.2 discusses the M-T_{X} scaling relationship in our sample of simulated clusters and shows that disrupted-looking clusters in this sample tend to be cooler at a given cluster mass. In Section 2.3 we attempt to quantify the relationship between morphology and temperature using four different substructure statistics and compare it to similar studies. We then show that substructure in these simulated clusters indeed correlates with scatter in the M-T_{X} relationship and assess the prospects for using that correlation to reduce scatter in the M-T_{X} plane. Section 2.4 summarizes our results.

2.2 Mass-Temperature Relation in Simulated Clusters

This study is based on an analysis of 121 clusters simulated using the cosmological hydrodynamics TREE+SPH code GADGET-2 [Springel(2005)], which were simulated in a standard Dark Energy + cold dark matter (ΛCDM) universe with matter density $\Omega_M = 0.3$, $h = 0.7$, $\Omega_b = 0.04$, and $\sigma_8 = 0.8$. These are key cosmological parameters that bear directly on the growth of structure. The parameter h maps directly to the Hubble Constant H_0, and merely is the scaling of that value to 100 km/s/Mpc. The dimensionless parameter Ω_M, which accounts for the abundance of matter (both Dark Matter and ordinary baryonic matter) in the Universe, is the ratio of the matter density ρ_M to the critical density ρ_c. The critical density is the density of mass-energy that is needed geometrically to close the Universe via General Relativity and in this setting mainly provides a convenient scale factor for comparing the relative abundance of its various ingredients. Similarly, Ω_b is the density parameter for ordinary baryonic matter. Finally, σ_8 provides the normalization for the scale-free spectrum of in density fluctuations imprinted in the early Universe and that were the seeds of structure growth. Specifically, σ_8 is the variance in density contrast $\delta\rho/\rho$ for density fluctutions with a Gaussian distribution, sampled at a length scale of 8 Mpc (projected to the present epoch).

The simulation treats radiative cooling with an optically-thin gas of primordial composition, includes a time-dependent UV background from a population of quasars, and handles star formation and supernova feedback using a two-phase fluid model with cold star-forming clouds embedded in a hot medium. All but four of the clusters are from the simulation described in [Borgani et al.(2004)], who simulated a box $192\,h^{-1}\,$Mpc on a side, with 480^3 dark matter particles and an equal number of gas particles. The present analysis considers the 117 most massive clusters within this box at $z = 0$, which all have M_{200} greater than $5 \times 10^{13}\,h^{-1}M_{\odot}$. By convention, M_{Δ} refers to the mass contained in a sphere which has a mean density of Δ times the critical density ρ_c, and whose radius is denoted by R_{Δ}

That cluster set covers the ∼1.5-5 keV temperature range, but the $192\,h^{-1}\,$Mpc box is too small to contain significantly hotter clusters. We therefore supplemented it with four clusters with masses $> 10^{15}\,h^{-1}\,M_{\odot}$ and temperatures > 5 keV drawn from a dark-matter-only simulation in a larger $479\,h^{-1}\,$Mpc box [Dolag & Stasyszyn(2009)]. The cosmology for this simulation also was ΛCDM, but with $\sigma_8 = 0.9$. These were then re-simulated including hydrodynamics, radiative cooling, and star formation, again with GADGET-2 and using the zoomed-initial-conditions technique of [Tormen(1997)], with a fourfold increase in resolution. This is comparable to the resolution of the clusters in the smaller box. Adding these four massive clusters to our sample gives a total of 121 clusters with M_{200} in the interval $5 \times 10^{13}\,h^{-1}M_{\odot}$ to $2 \times 10^{15}\,h^{-1}M_{\odot}$.

We first need to specify our definitions for mass and temperature. In this chapter, cluster mass refers to M_{200}. For temperature, we use two definitions. The first is the emission-weighted temperature

$$T_{\rm EW} = \frac{\int T[n^2\Lambda(T)]\, d^3x}{\int n^2\Lambda(T)\, d^3x} \quad , \tag{2.1}$$

where n is the electron number density and $\Lambda(T)$ is the usual cooling function for intracluster plasma. The second is the spectroscopic-like temperature of [Mazzotta et al.(2004)],

$$T_{\rm SL} = \frac{\int T[n^2 T^{-3/4}]\, d^3x}{\int n^2 T^{-3/4}\, d^3x} \quad , \tag{2.2}$$

where the power-law weighting function replacing $\Lambda(T)$ is chosen so that $T_{\rm SL}$ approximates as closely as possible the temperature that would be determined from fitting a single-temperature plasma emission model to the integrated spectrum of the intracluster medium. The presence of metals in the ICM of real clusters introduces line emission that complicates the computation of $T_{\rm SL}$ for clusters <3 keV [Vikhlinin(2006)]. However, the simulated spectra for the clusters in our sample are modeled with zero metallicity, which eases this restriction in our analysis.

Figure 2.1 shows the mass-temperature relations based on these definitions for our sample of simulated clusters. The best fits to the power-law form

$$M = M_0 \left(\frac{T_{\rm X}}{3\,{\rm keV}} \right)^{\alpha} \tag{2.3}$$

have the coefficients $M_0 \simeq 5.9 \times 10^{13}\ h^{-1} M_{\odot}, \alpha \simeq 1.5$ for $T_{\rm X}$ corresponding to $T_{\rm SL}$ and $M_0 \simeq 4.4 \times 10^{13}\ h^{-1} M_{\odot}, \alpha \simeq 1.4$ for $T_{\rm X}$ corresponding to $T_{\rm EW}$. As is generally the case for simulated clusters, the power-law indices of the mass-temperature relations found here are consistent with cluster self-similarity and the virial theorem [Kaiser(1986), Navarro et al.(1995)]. These relationships have scatter, which we characterize by the standard deviation in log space $\sigma_{\ln M}$ about the best-fit mass at fixed temperature $T_{\rm X}$. When relating M to the emission-weighted temperature $T_{\rm EW}$, we find $\sigma_{\ln M} = 0.102$. When relating cluster mass M to the spectroscopic-like temperature $T_{\rm SL}$, the scatter is $\sigma_{\ln M} = 0.127$. That the scatter is larger for the spectroscopic-like temperature is not surprising, given the sensitivity of $T_{\rm SL}$ to the thermal complexity of the ICM.

Figure 2.1 also highlights two sub-samples for each definition of temperature, selected based on the clusters' deviations in $\ln T_{\rm X}$ space from the mean mass-temperature relation. In each panel, open circles represent the eight clusters that have the largest positive deviations and are therefore "hotter" than other clusters of the same mass, while filled circles represent the eight with the largest negative deviation and are "cooler" than other clusters of the same mass. In general, these temperature estimates are well correlated, so that hotter outliers in $T_{\rm EW}$ are also hotter outliers in $T_{\rm SL}$ and cooler outliers in $T_{\rm EW}$ are also cooler outliers in $T_{\rm SL}$. Since Figure 2.1 distinguishes the most extreme outliers for the two temperature estimates, this distinction may define slightly different sets, though they still overlap.

Figure 2.2 presents a gallery of surface brightness maps for two sets of eight clusters with the most extreme offsets from the mean M-$T_{\rm SL}$ relation. The eight unusually hot clusters are in the top panel, and the eight cooler clusters are in the bottom panel. In these plots the hotter clusters appear more symmetric, and are seemingly "more relaxed," and the cooler clusters appear less symmetric and seemingly "less relaxed." The gallery as a whole therefore suggests that relaxed clusters tend to be hot for their mass and unrelaxed clusters tend to be cool for their mass.

At first glance, the result that disrupted-looking clusters in cosmological simulations tend to be cooler than other clusters of the same mass may seem counter-intuitive, since one might expect that mergers ought to produce shocks that raise the mean temperature of the intracluster medium. This finding has also been noted by [Mathiesen & Evrard(2001)] and [Kravtsov et al.(2006)]. Cluster systems in the process of merging tend to be cool for their total halo mass because much of the kinetic energy of the merger has not yet been

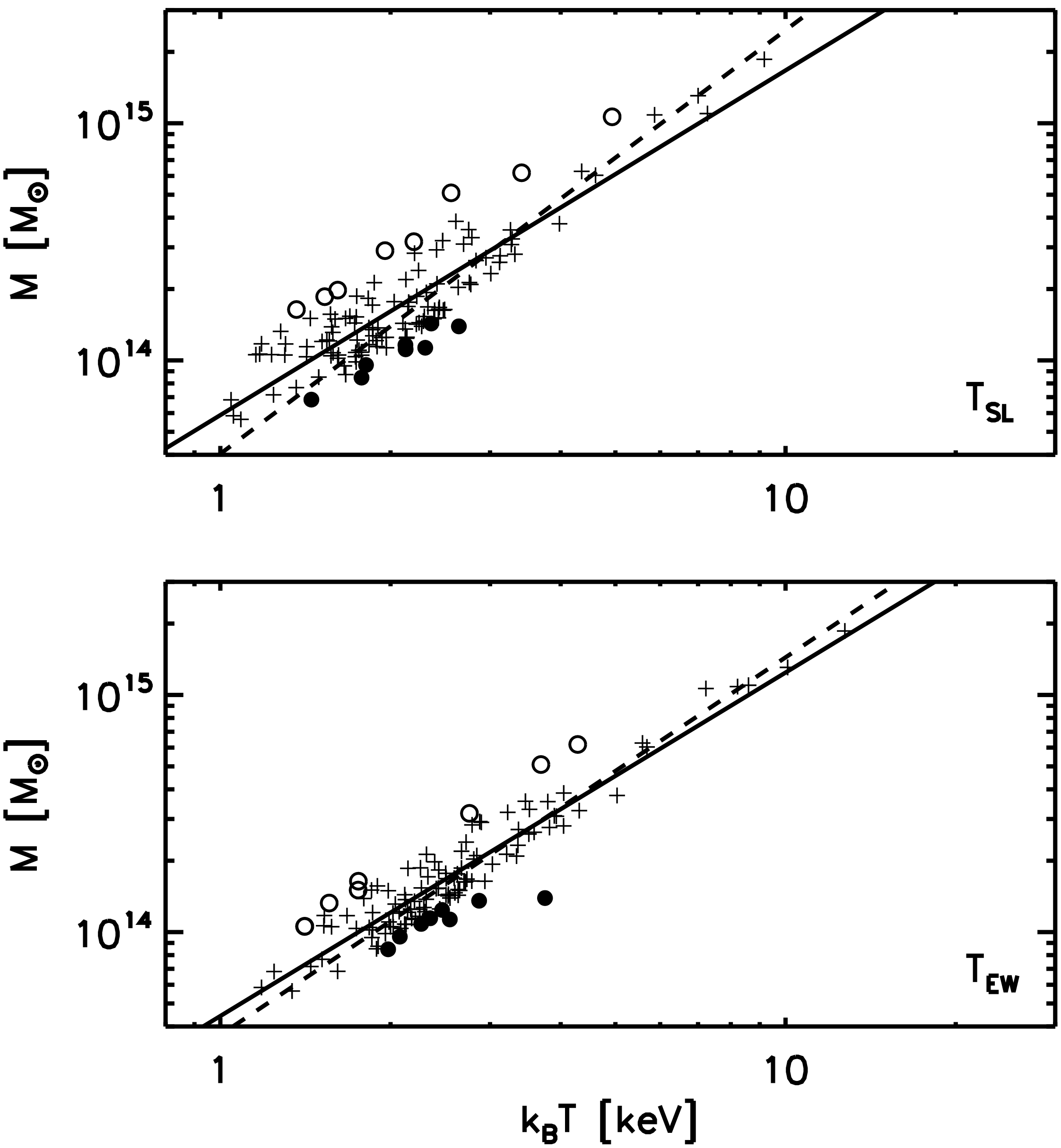

Figure 2.1: Mass-temperature (M-T_X) relationships for the 121 clusters in our sample. Spectroscopic-like temperature T_{SL} is plotted in the top panel, while emission-weighted temperature T_{EW} is plotted in the bottom panel. The solid lines show the best-fit power-law relation $M = M_0(T_X/3 \text{ keV})^\alpha$ over the whole sample, while the dashed lines show the best-fit relation for systems with $T_X > 2$ keV. Open circles represent the clusters that have the greatest positive temperature offset from the mean relationship, and filled circles represent the clusters with the greatest negative temperature offset.

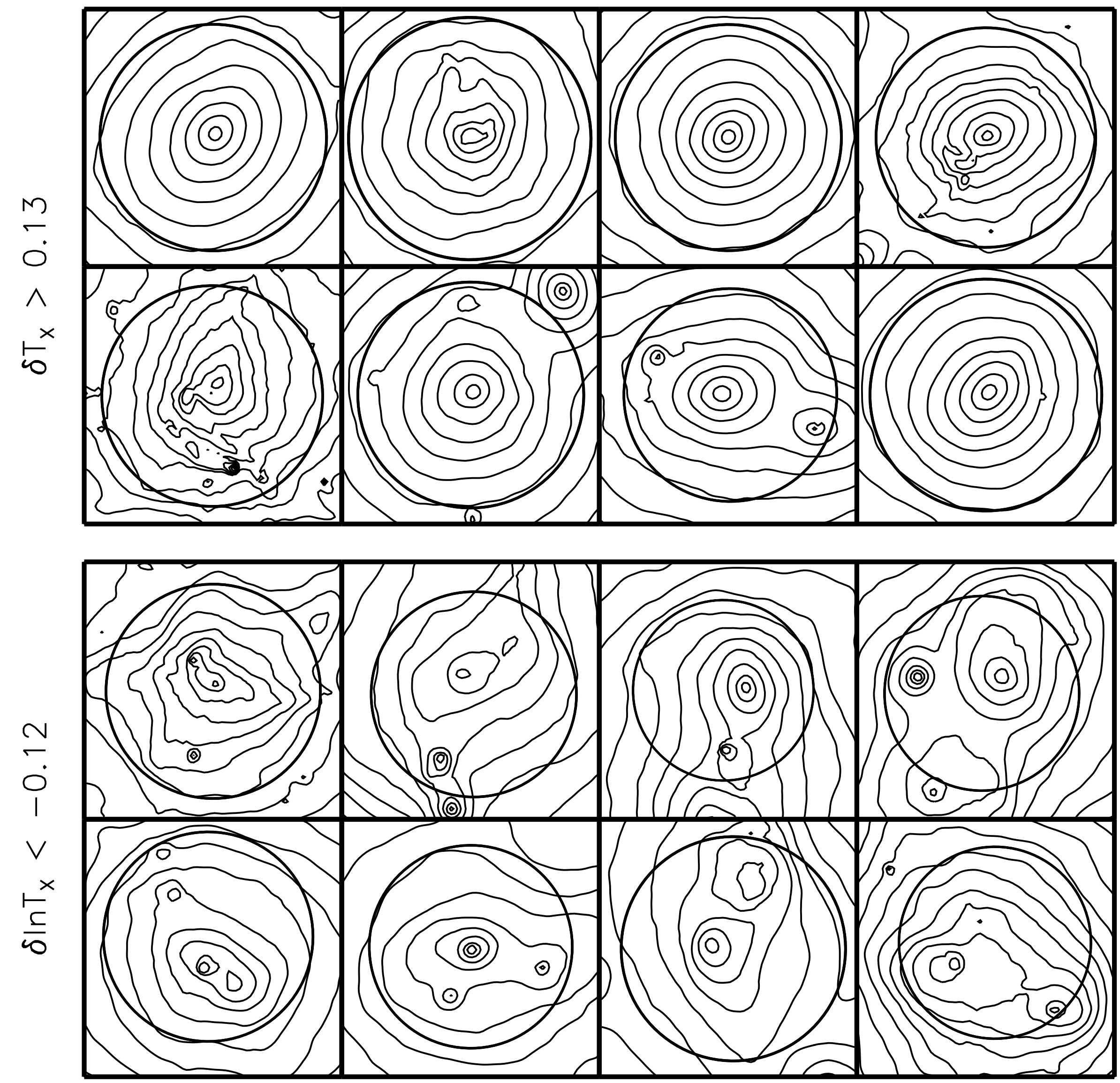

Figure 2.2: Surface-brightness contour maps for sixteen of the clusters in our sample, overlaid with a circular aperture of radius R_{500}. The top panel has eight maps representing the clusters that have the largest positive deviation $\delta \ln T_{\rm X}$ from the mean M-$T_{\rm X}$ relation, calculated using the spectroscopic-like temperature $T_{\rm SL}$.

thermalized.

The idealized simulations of [Poole et al.(2007)] illustrate what may happen to the ICM temperature during a single merger. Before the cores of the two merging systems collide, the mean temperature is cool for the overall halo mass because it is still approximately equal to the pre-merger temperature of the two individual merging halos. There is a brief upward spike in temperature when the cores of the merging halos collide, after which the system is again cool for its mass. Then, as the remaining kinetic energy of the merger thermalizes over a period of a few billion years, the temperature gradually rises to its equilibrium value. The merging system therefore spends a considerably longer time at relatively cool values of mean temperature for its halo mass than at relatively hot values. Hence, such simulations suggest a possible explanation for why more relaxed systems would tend to lie on the hot side of the M-$T_{\rm X}$ relation, while disrupted systems would tend to lie on the cool side. A caveat, however, is that the current generation of hydrodynamic cluster simulations tend to produce relaxed clusters whose temperature profiles continue to rise to smaller radii than is observed in real clusters [Tornatore et al.(2003), Nagai et al.(2007)], potentially enhancing average temperatures for such systems. As a separate test of this effect, we excise the core regions from our sample clusters, calculate new substructure measures and new emission-weighted temperatures for the core-excised clusters, and repeat our analysis.

2.3 Quantifying Substructure

The question we would like to address in this study is whether the surface-brightness substructure evident in Figure 2.2 is well enough correlated with deviations from the mean mass-temperature relation to yield useful corrections to that relation. In order to answer that question, we need to quantify the surface-brightness substructure in each cluster image, so that we can determine the degree of correlation across the entire sample. [O'Hara et al.(2006a)] explored the relationship between cluster structure and X-ray scaling relations in both observed and simulated clusters, and we adopt their suite of substructure measures in this study. These include centroid variation, axial ratio, and the power ratios of [Buote & Tsai(1995)]. In this section we define and discuss those statistics and apply them to surface-brightness maps made from three orthogonal projections of each cluster. Then we assess how well these statistics correlate with offsets from the mean mass-temperature relation.

2.3.1 Axial Ratio

The axial ratio η for a cluster surface-brightness map is a measure of its elongation, which is of interest because it has been found from simulations that the ICM is often highly elongated during merger events [Evrard et al.(1993), Pearce et al.(1994)]. It is computed from the second moments of the surface brightness,

$$M_{ij} = \sum I_{\mathrm{X}} x_i x_j. \tag{2.4}$$

The summation is conducted over the coordinates (x_1, x_2) of the pixels that lie within an aperture centered at the origin of the coordinate system to which (x_1, x_2) refer. Following the work of [O'Hara et al.(2006a)], we use an aperture of radius R_{500} centered on the brightness peak. We then compute η from the ratio of the non-zero elements that result from diagonalizing the matrix M. That is,

$$D = U^T M U, \tag{2.5}$$

where U is a diagonalizing matrix for M, and

$$\eta = \left\{ \begin{array}{ll} \frac{D_{12}}{D_{21}}, & D_{12} \leq D_{21} \\ \frac{D_{21}}{D_{12}}, & D_{12} > D_{21} \end{array} \right\} . \tag{2.6}$$

The axial ratio is therefore defined to be in the range $\eta \in [0, 1]$, with $\eta = 1$ for a circular cluster. Of course there are other choices for the origin of the coordinate system, besides using the brightness peak. For instance, in order to avoid misplaced apertures yielding artificially low axial ratios for nearly circular distributions, one could adjust the position of the aperture to seek a maximum in η. Doing this, we sometimes find that $\eta \approx 1$ even for non-circular clusters, as is evident in Figure 2.3. This figure depicts the surface-brightness map of what appears to be a disturbed cluster, chosen from among those in our sample that appear by eye to be the most unrelaxed. Yet, it happens to have an axial ratio very close to 1 for an aperture placed so as to maximize η. This example demonstrates that, while the axial ratio statistic may yield results consistent with a visual interpretation of cluster substructure, it is also capable of unexpected results for some clusters.

To further illustrate this point, we have computed an axial ratio value for this cluster for every possible choice of aperture placement. Apertures of radius R_{500} were centered on each and every pixel within the surface-brightness map, provided the aperture so placed does not reach the edge of the map. This procedure generated an axial-ratio “surface” mapping all of the aperture placements to a value of η. Figure 2.4 shows the axial-ratio surface for the cluster in Figure 2.3. For comparison purposes, Figure 2.5 presents an axial-ratio surface map for a very symmetric, uniform, and apparently relaxed cluster, in which the cluster’s brightness peak reassuringly corresponds to the aperture location that maximizes η. In contrast, the presence of two peaks in the axial-ratio surface for the asymmetric cluster

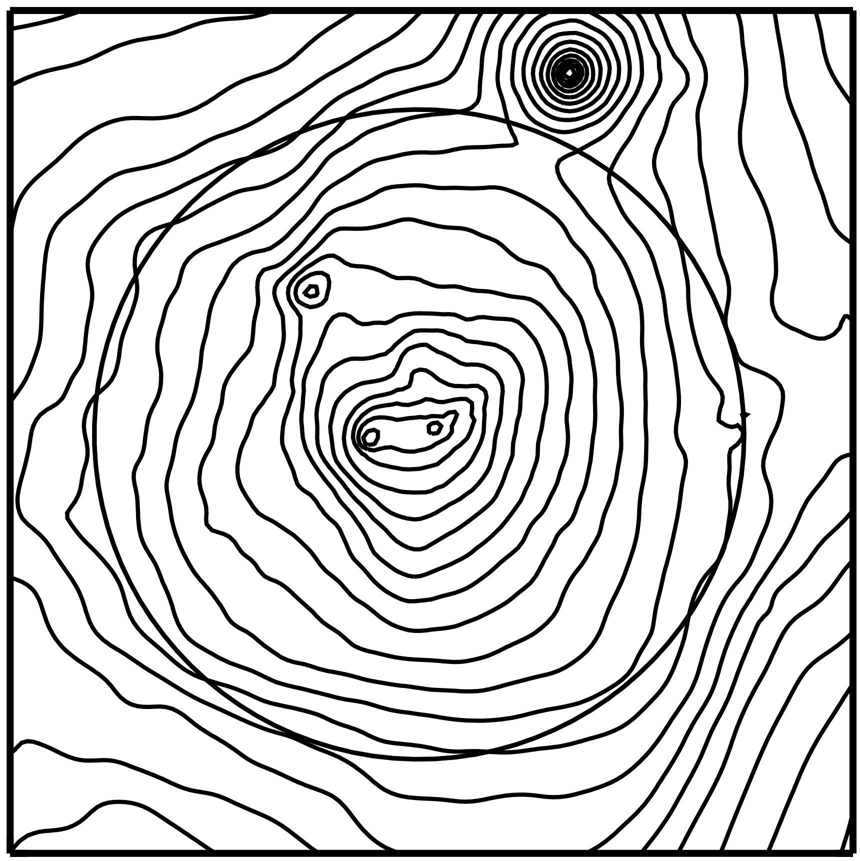

Figure 2.3: Surface-brightness contour plot of an asymmetric cluster which, for certain choices of aperture placement, yields an axial ratio close to 1. The circle represents an aperture of R_{500}

.

shows that η can sometimes depend strongly on aperture placement. Ideally, we would like to place the aperture on the "center" of this cluster, but the center of an unrelaxed cluster can be difficult to define, meaning that the axial ratio statistic may be likewise ill-defined for such clusters.

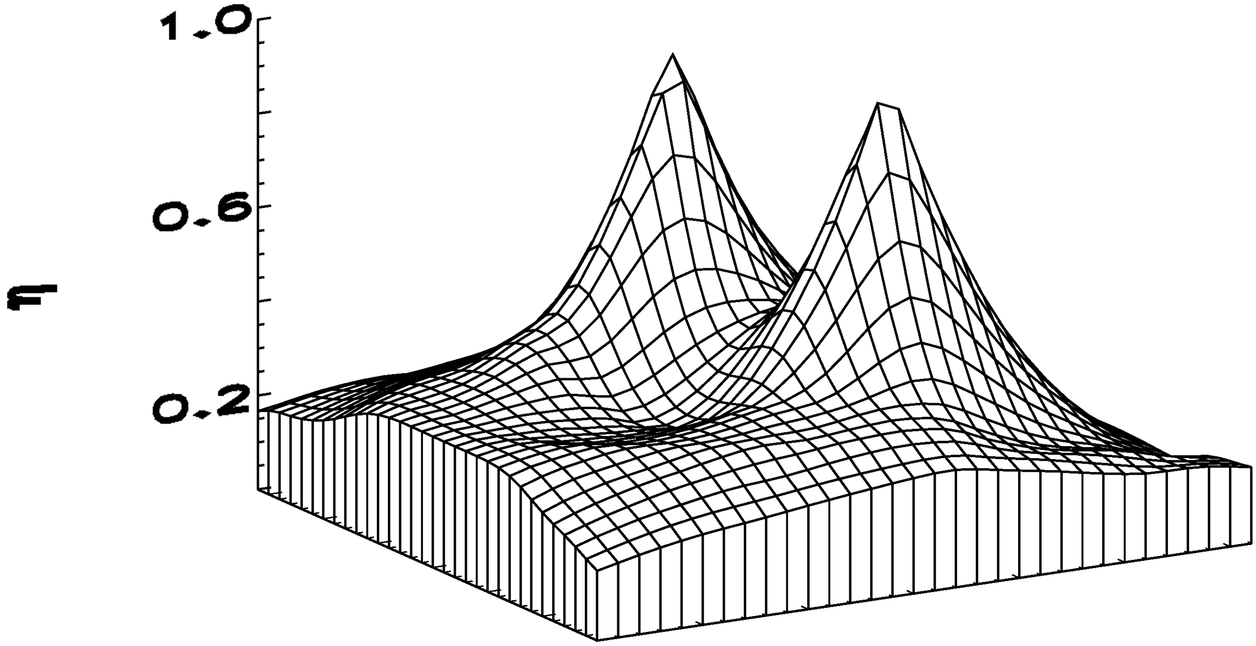

Figure 2.4: Surface of axial ratio η as a two-dimensional function of the coordinates of the aperture center. The axial ratio statistic appears to be ill-defined for this cluster.

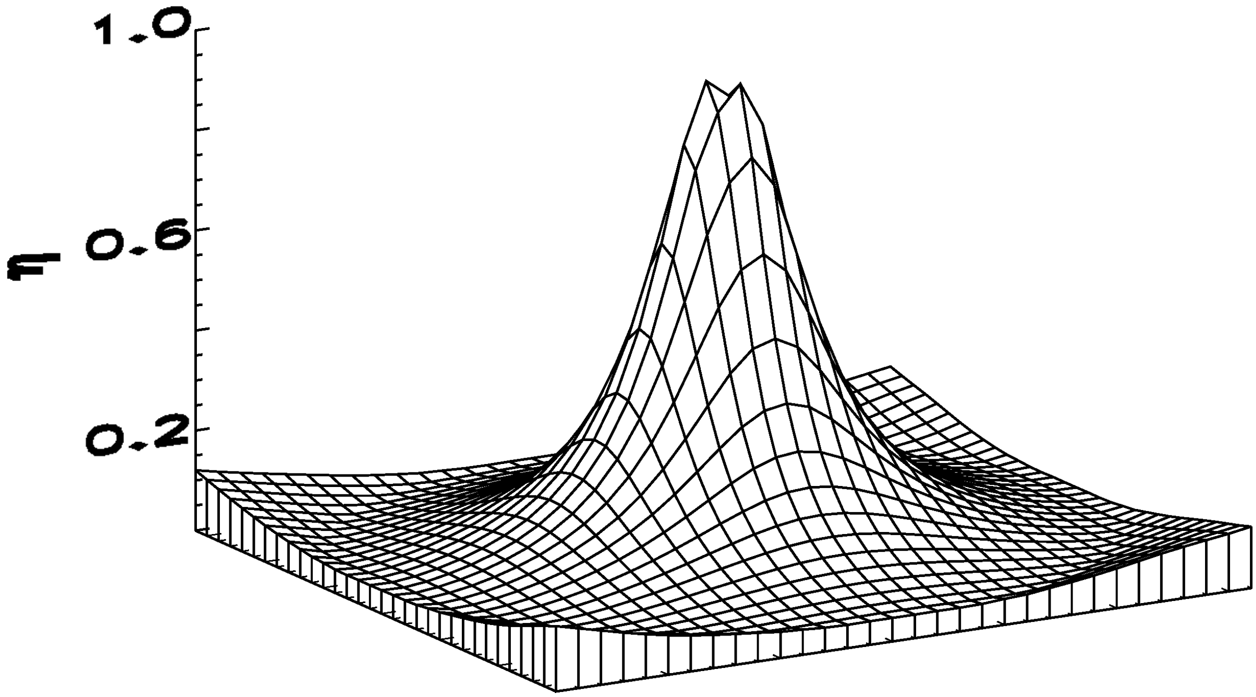

Figure 2.5: Abstract surface of axial ratio η as a two-dimensional function of the coordinates of the aperture center. This is a relaxed cluster, for which the axial ratio is better-defined.

2.3.2 Power Ratio

The power-ratio statistics [Buote & Tsai(1995), O'Hara et al.(2006a)] quantify substructure by decomposing the surface-brightness image into a two-dimensional multi-pole expansion, the terms of which are calculated from the moments of the image, computed within an aperture of radius $R_{\rm ap}$:

$$a_m(R_{\rm ap}) = \int_{R' \le R_{\rm ap}} \Sigma(\vec{x}')(R')^m \cos m\phi' \; d^2x' \tag{2.7}$$

$$b_m(R_{\rm ap}) = \int_{R' \le R_{\rm ap}} \Sigma(\vec{x}')(R')^m \sin m\phi' \; d^2x'. \tag{2.8}$$

The power in terms of order m is then

$$P_m = \frac{(a_m^2 + b_m^2)}{2m^2 R_{\rm ap}^{2m}}. \tag{2.9}$$

For $m = 0$, the power is given by

$$P_0 = [a_0 \ln(R_{\rm ap})]^2. \tag{2.10}$$

The power ratios $P_{m0} \equiv P_m/P_0$ are then dimensionless measures of substructure which have differing interpretations. For instance, P_{10} quantifies the degree of balance about some origin and can be used to find the image centroid, P_{20} is related to the ellipticity of the image, and P_{30} is related to the triangularity of the photon distribution. As in the case of the axial ratio computations, we set the aperture radius $R_{\rm ap}$ equal to R_{500}. The most appropriate place to center the aperture is at the set of pixel coordinates that minimizes P_{10}, which we achieve using a self-annealing algorithm.

2.3.3 Centroid Variation

The centroid variation statistic w is a measure of the center shift, or "skewness", of a two-dimensional photon distribution. It is measured for a cluster surface-brightness map in the following way. For a set of surface-brightness levels one finds the centroids of the corresponding isophotal contours and computes the variance in the coordinates of those centroids, scaled to R_{500}. Here we select 10 isophotes evenly spaced in $\log I_{\rm X}$ between the minimum and maximum of $I_{\rm X}$ within an aperture of radius R_{500} centered on the brightness peak, so as to adapt to the full dynamic range of surface brightness for different clusters. We employed this adaptive scheme because using one set of isophotes for all clusters tended to ignore important substructure in less massive clusters when they had surface brightness substructure inside R_{500} but outside of the lowest isophote.

2.3.4 Substructure and Scaling Relationships

Using the quantitative measures of substructure described in the previous section, we can test the significance of the relationship between substructure and temperature offset hinted at in Figure 2.2. We begin by treating four of our substructure statistics—centroid variation w, axial ratio η, and power ratios P_{20} and P_{30}—as different imperfect measurements of an intrinsic degree of substructure S. Figure 2.6 shows the relationship between substructure and a cluster's deviation $\delta \ln T_{\rm X}$ from the mean M-$T_{\rm X}$ relation for each substructure measure. In each case we present results for both the spectroscopic-like temperature $T_{\rm SL}$ and the emission-weighted temperature $T_{\rm EW}$. Note that centroid variation w and the power ratios P_{20} and P_{30} have large dynamic ranges, whereas the axial ratio η is always of order unity. We therefore attempt to fit the relationships between $\delta \ln T_{\rm X}$ and the different substructure measures with the following forms:

$$\delta \ln T_{\mathrm{X}} = \begin{cases} Aw^{\alpha} \\ B + \beta\eta \\ CP_{20}^{\gamma} \\ DP_{30}^{\lambda} \end{cases} \tag{2.11}$$

To visually indicate where the bulk of our substructure measures lie, Figure 2.6 has light gray bands covering the extremes, so that 80% of our sample clusters have substructure measures lying between the extremes. The power ratios in our study generally span two decades (in units of 10^{-7}), from ∼2—300 for P_{20} and from ∼0.01—10 for P_{30}. These ranges are consistent with those of [Buote & Tsai(1995)], [O'Hara et al.(2006a)], and [Jeltema et al.(2008)]. The measurements of axial ratio in our sample, with 80% of clusters having η∼0.4—0.95, cover a slightly wider range than do the simulated clusters of [O'Hara et al.(2006a)]. Finally, our measurements of centroid variation, with 80% of clusters having $w[R_{500}]$∼0.01—0.1, are again similar to those of [O'Hara et al.(2006a)].

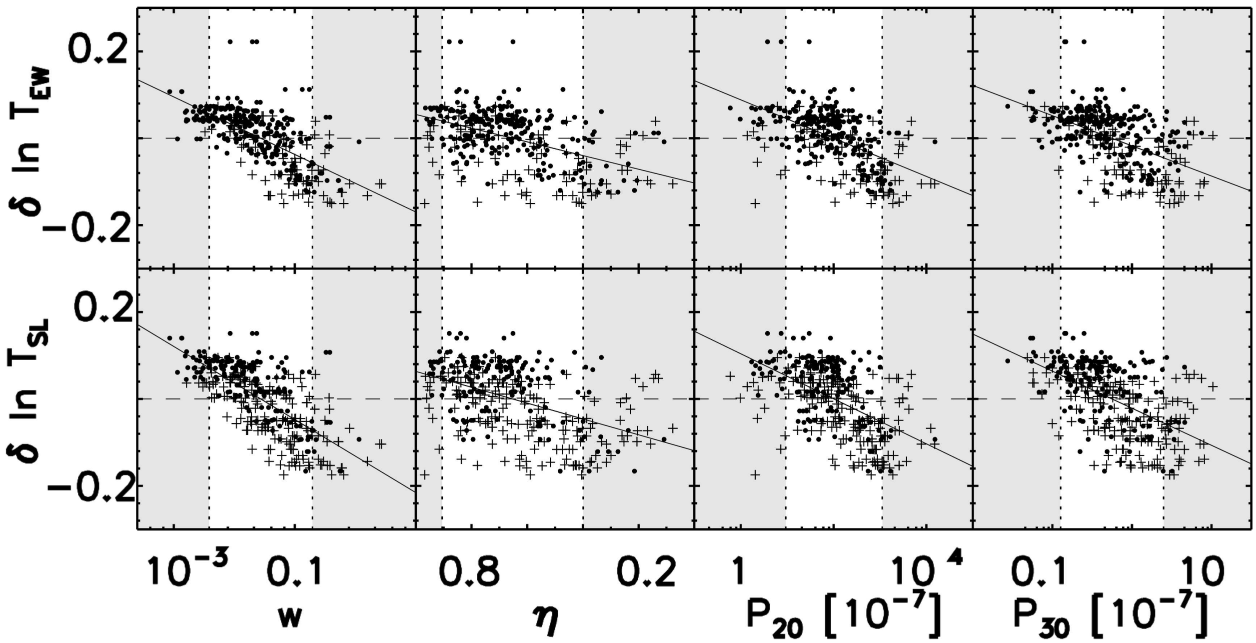

Figure 2.6: Relationship between a cluster's deviation $\delta \ln T_{\mathrm{X}}$ from the mean M-T_{X} relationship and four measures of substructure.

As denoted in Figure 2.6 by black filled circles, the systems with T_{X} above 2 keV occupy a slightly narrower range of substructure values than the systems below 2 keV, which are denoted by plus signs. For the axial ratio and the power ratios, the variance is 15 to 25 percent larger among the low-temperature systems when compared to the systems with $T_{\mathrm{X}} > 2$ keV. For centroid variation the variance among the low-temperature systems is approximately the same as it is among the high-temperature systems. However, it is not clear that there is a significant correlation between substructure and mass, since the mean substructure values are generally very similar between the low-temperature and high-temperature sub-samples. The mean value of the power ratio P_{30} is significantly larger for the low-temperature sub-sample, however this measure also has the weakest correlation with offsets from the mean M-T_{X} relation.

To test whether the low-mass clusters in our sample significantly boost the overall scatter in the M-T_{X} relation, we perform a cut at 2 keV and fit this relation both to the whole sample and to the sub-sample above 2 keV. Figure 2.7 shows the residuals in mass, actual minus predicted, where the predicted mass derives only from the M-T_{X} relation. The plus signs indicate clusters whose mass is predicted from an M-T_{X} relation derived from all 121 clusters. The black filled circles indicate clusters that are above 2 keV in X-ray temperature, with the mass estimated using the sub-sample M-T_{X} relation. There is a negligible reduction in scatter, from 0.127 to 0.124 for T_{SL} and from 0.102 to 0.094 for T_{EW}, suggesting that at best only a modest improvement is found in our sample if we remove the low-mass systems. In order to test the degree to which incorporating substructure measures adds to this modest improvement, when we compare mass estimates derived using substructure to those derived only from the M-T_{X} relation, we focus on clusters above 2 keV in the rest of our analysis.

Figure 2.6 shows that for our simulated clusters, a greater amount of measured substructure tends to be associated with "cooler" clusters while less substructure tends to be associated with "hotter" clusters. Also, the centroid variations w are more highly-correlated with $\delta \ln T_{\rm X}$ than are the other substructure parameters. We interpret this to mean that the centroid variation is a better predictor of the offset in the M-$T_{\rm X}$ relationship than are the power ratios and the axial ratio, though all four measures appear to be related to the temperature offset. Again, in this figure we denote systems above 2 keV by black filled circles, and systems below 2 keV by plus signs.

Correlations between substructure and $\delta \ln T_{\rm X}$ can potentially be exploited to improve on mass estimates of real clusters derived from the mass-temperature relation. Instead of computing the temperature offset at fixed mass, we can determine a substructure-dependent mass offset at fixed temperature and then apply it as a correction to the predicted mass $M_{\rm pred}(T_{\rm X})$ one would derive from the mean M-$T_{\rm X}$ relation alone. To assess the prospects for such a correction, based on this sample of simulated clusters, we first define the mass offset from the mean mass-temperature relation to be

$$\delta \ln M(T_{\rm X}) = \ln \left[\frac{M}{M_{\rm pred}(T_{\rm X})} \right] \quad , \tag{2.12}$$

where M is the cluster's actual mass, and examine the correlations between substructure measures and $\delta \ln M$. Figure 2.8 shows the results. These plots show mass predictions from both the M-$T_{\rm SL}$ relation and the M-$T_{\rm EW}$ relation. Consistent with our analysis of $\delta \ln T_{\rm X}$, the centroid variation w appears to be a more effective predictor of the mass offset $\delta \ln M(T_{\rm X})$. Nonetheless, all four measures of substructure appear to be correlated with mass offset.

In order to incorporate a substructure correction into the mass-temperature relation,

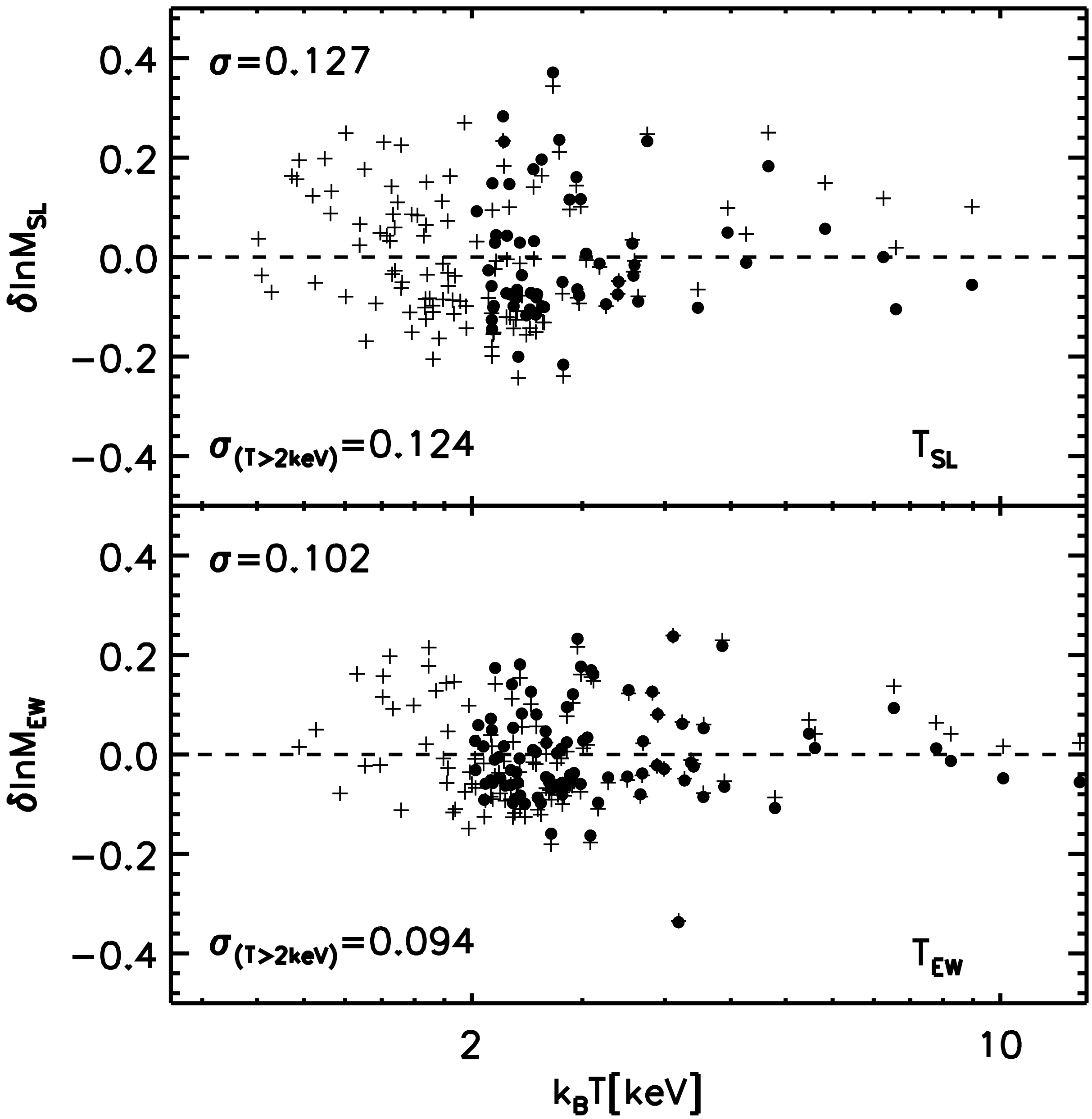

Figure 2.7: Comparison of mass offset $\delta \ln M$ between true mass and predicted mass, based on the $M(T_{\mathrm{X}})$ relation. Plus signs indicate residuals for masses estimated from the M-T_{X} relation derived from all 121 clusters, while black filled circles are for masses estimated from the M-T_{X} relation for clusters above 2 keV. Upper panels are for spectroscopic-like temperature and lower panels are for emission-weighted temperature. The standard deviations σ in the residuals are given in each plot.

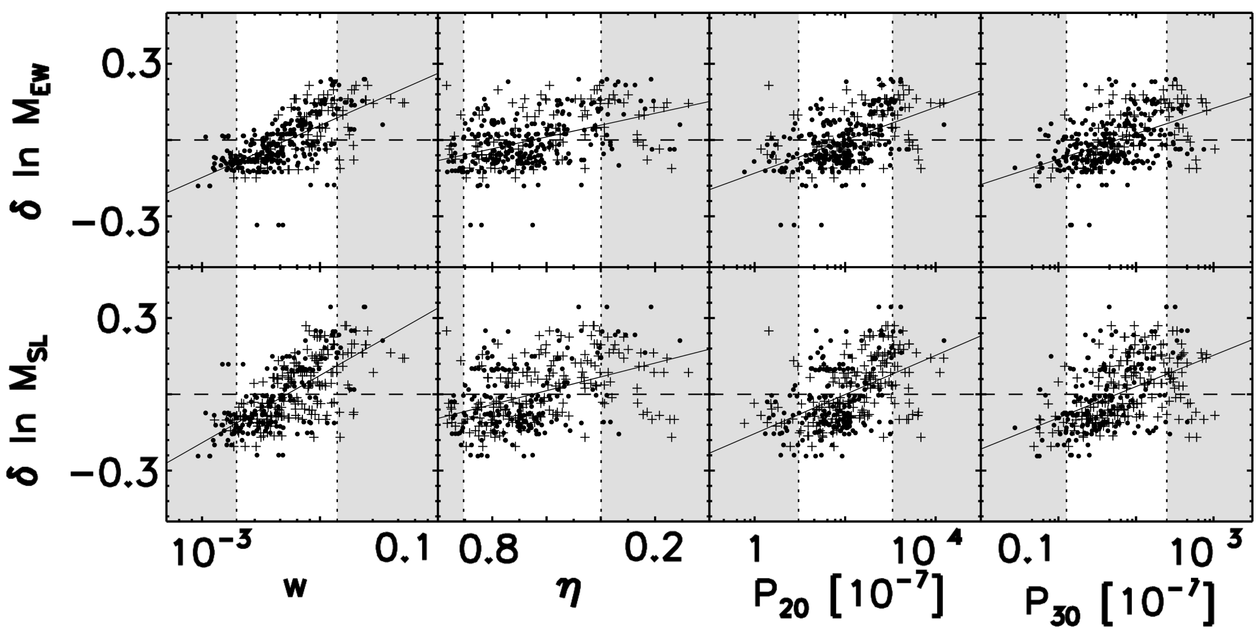

Figure 2.8: Relationship between substructure and mass offset $\delta \ln M(T_\mathrm{X})$ from the mean M-T_X relationship for the same substructure measures as in the previous figure. The lower panels are for $T_\mathrm{X} = T_\mathrm{SL}$, and the upper panels are for $T_\mathrm{X} = T_\mathrm{EW}$. The solid lines indicate the best-fitting linear relationships to the above 2 keV sub-sample denoted by black filled circles, and the gray bands and vertical dashed lines mark the extremes in substructure between which 80% of our clusters lie. The plus signs correspond to systems below 2 keV, while the black filled circles correspond to systems above 2 keV.

we perform a multiple regression, fitting our simulated clusters' mass, temperature, and substructure data to the form,

$$\log M_{\mathrm{pred}}(T_{\mathrm{X}}, S) = \log M_0 + \alpha \log T_{\mathrm{X}} + \beta S, \tag{2.13}$$

where S represents one of the following substructure measures: η, $\log w$, $\log P_{20}$, or $\log P_{30}$. This fit gives us a substructure-corrected mass prediction $M_{\mathrm{pred}}(T_{\mathrm{X}}, S)$ for each substructure measure, and we can assess the effectiveness of that correction by measuring the dispersion of the substructure-corrected mass offset

$$\delta \ln M(T_{\mathrm{X}}, S) = \ln \left[\frac{M}{M_{\mathrm{pred}}(T_{\mathrm{X}}, S)} \right] \ , \tag{2.14}$$

between the revised prediction and the true cluster mass.

Figure 2.9 shows the results of that test. Open circles in each panel indicate mass offsets $\delta \ln M(T_{\mathrm{X}})$ without substructure corrections, which have a standard deviation $\sigma_{M(T)}$. Filled circles indicate mass offsets $\delta \ln M(T_{\mathrm{X}}, S)$ with substructure corrections, which have a standard deviation $\sigma_{M(T,S)}$. The upper set of panels shows results for T_{SL}, and the lower set is for T_{EW}. In each case, incorporating a substructure correction to the mass-temperature relation reduces the scatter, yielding more accurate mass estimates. The centroid variation corrections are the most effective, reducing the scatter in mass from 0.124 to 0.085 in the M-T_{SL} relation and from 0.094 to 0.072 in the M-T_{EW} relation, though admittedly this is again a modest improvement. Although non-negligible structure correlates significantly with offsets in the M-T_{X} plane, apparently it does so with substantial scatter. This scatter may be partly due to projection effects, in which line-of-sight mergers are discounted by the measures of substructure and may dilute their corrective power [Jeltema et al.(2008)].

Lastly, Figure 2.10 shows the results for a similar analysis to that of Figure 2.9, except that in this case we have excised a region of radius $0.15R_{500}$ around the center of each cluster and recomputed $T_{\rm EW}$. We do this to test whether offset in temperature, whose correlation with substructure is the basis of our correction scheme, stems from a potentially unrealistic feature, which is that the cores of many real clusters have temperature profiles that decline at larger radii than occurs in simulated clusters. As in Figure 2.9, we restrict our analysis to clusters above 2 keV. After doing this test, for $T_{\rm EW}$ excising the core actually increases the scatter in M-$T_{\rm X}$ from 0.094 to 0.106. It may be that by removing the bright central region, the average temperature becomes more sensitive to structure outside the core. Also, this figure shows that the effect of incorporating substructure measurements into the mass-estimates is still present. The scatter is reduced to 0.075 for w, 0.093 for η, 0.090 for P_{20} and 0.094 for P_{30}. Figure 2.10 summarizes the results of this test, which support the conclusion that the reduction in scatter we realize using substructure is a real effect and not an artifact of known defects in the simulations.

2.3.5 Comparisons with Other Substructure Studies

[O'Hara et al.(2006a)] examined the relationship between galaxy cluster substructure and X-ray scaling relationships, including the M-$T_{\rm X}$ relation, using both a flux-limited sample of nearby clusters and a sample of simulated clusters, and found a greater amount of scatter among the more relaxed clusters in their observed sample. Contrasting that result they also found a greater amount of scatter among the more disrupted clusters in their simulation sample, though they characterize the evidence for this second result to be weak. Finally, they see no evidence in either sample for more disrupted clusters to be below the mean, and the more relaxed clusters to be above. One difference between our study and theirs is the presence of radiative cooling and supernova feedback in the simulation that produced our cluster sample. Also, the focus of our work is different from theirs in that we concentrate on the degree of correlation between the amount of substructure and the size and direction of the offset from the mean relation. We do find significant evidence of this correlation, such that relaxed clusters are hotter than expected given their mass. We also test, as best we can given our simulation sample, the hypothesis that substructure can be used to improve mass estimates derived from the ICM X-ray temperature. It is possible that our detection of a correlation between substructure and temperature offset arises from the additional physics in our simulated clusters, since when radiative cooling is included, cool lumps may be better preserved than in simulations that don't include cooling.

Our results are in agreement with [Valdarnini(2006)], who examined substructure in clusters simulated with cooling and feedback and found that unrelaxed clusters, identified with a larger power ratio P_{30}, have spectral-fit temperatures biased low relative to the mass-weighted temperatures. This trend aligns with our finding that the spectroscopic-like temperature $T_{\rm SL}$ is lower than the best-fit temperature at fixed mass for clusters with larger power ratios P_{20} and P_{30}. However, [Valdarnini(2006)] did not investigate the effectiveness of substructure measures in reducing scatter in the mass-temperature relation.

Our results are also in agreement with some of the results of [Jeltema et al.(2008)], who have recently investigated correlations between substructure and offsets in mass predictions in simulated clusters. They found that measuring cluster structure is an effective way to correct masses estimated using the assumption of hydrostatic equilibrium, which tend to be underestimates. Our findings support these results, given that we find substructure can be used to correct masses estimated directly from the M-$T_{\rm X}$ relationship. There also are differences between our findings and theirs. They report that the M-T_{X} relation for their simulation sample shows no dependence on structure, whereas the clusters in our sample exhibit offsets that correlate with the degree of substructure. One possibility is that these differences stem from differences in the simulations' feedback mechanisms. Another possibility is that some of the offset we observe derives from enhanced temperatures in simulations with radiative cooling. As we describe in section 3, we perform a test in which we estimate T_{EW} using projected surface-brightness and temperature maps, in order to remove the core regions from our analysis, but this may be less effective than properly excising the cores in the simulations, as [Jeltema et al.(2008)] have done.

[Kravtsov et al.(2006)] also looked at the relationship that cluster structure has to the M-T_{X} relation in simulated clusters, to show that the sensitivity of mass proxies Y_X and Y_{SZ} to substructure is not very strong. They divided their sample into unrelaxed and relaxed sub-samples, based on the presence or absence of multiple peaks in the surface-brightness maps of clusters, and found the normalization of the M-T_{X} relation to be biased to cooler temperatures for the unrelaxed systems. Other workers also have looked at the relationship between the M-T_{X} relation and substructure, as reflected in the X-ray spectral properties. [Mathiesen & Evrard(2001)] have examined the ratio of X-ray spectral-fit temperatures in hard and full bandpasses for an ensemble of simulated clusters, and found it to be a way of quantifying the dynamical state of a cluster. We consider our approach of using surface-brightness morphology information to be complementary to theirs. More recently, [Kay et al.(2007)] performed an interesting analysis on another large-volume simulation sample, using as substructure metrics the centroid variation and measures of concentration to report evolution in the luminosity-temperature relationship. Specifically, they report that the more irregular clusters in their sample lie above the mean M-T_{X} relation (i.e., they are cooler than average), for the spectroscopic-like temperature T_{SL}.

2.4 Summary

Using a sample of galaxy clusters simulated with cooling and feedback, we investigated three substructure statistics and their correlations with temperature and mass offsets from mean scaling relations in the M-T_{X} plane. First, we showed that the substructure statistics w, η, P_{20} and P_{30} all correlate significantly with $\delta \ln T_{\mathrm{X}}$, though with non-negligible scatter. In all cases this scatter is larger for $\delta \ln T_{\mathrm{SL}}$ than it is for $\delta \ln T_{\mathrm{EW}}$. Next, we considered the possibility that M-T_{X} scatter is driven by low-mass clusters. We tested the degree to which scatter can be reduced by filtering out these systems. This consisted of performing a cut at 2 keV, for which we saw that it yielded a modest improvement in mass estimates. To see whether incorporating substructure could refine these mass estimates, we first showed that w, η, P_{20}, and P_{30} correlate significantly with the difference $\delta \ln M$ between masses predicted from the mean $M(T_{\mathrm{X}})$ relation and the true cluster masses, with non-negligible scatter that again is less for $M(T_{\mathrm{EW}})$ than it is for $M(T_{\mathrm{SL}})$. Then we adopted a full three-parameter model, M-T_{X}-S, which includes substructure information S estimated using w, η, P_{20}, and P_{30}. Scatter about the basic two-parameter M-T_{EW} relation was 0.094. Including substructure as a third parameter reduced the scatter to 0.072 for centroid variation, 0.084 for axial ratio, 0.081 for P_{20}, and 0.084 for P_{30}. Scatter about the basic two-parameter M-T_{SL} relation was 0.124, and including substructure as a third parameter reduced the scatter to 0.085 for centroid variation, 0.112 for axial ratio, 0.110 for P_{20}, and 0.108 for P_{30}. As one last test, and to increase our confidence that our substructure measures are not relying on potentially non-physical core structure in the simulations, we also repeated the comparison of mass-estimates for $T_{\rm EW}$, with the core regions of the clusters excised. First, removing the core slightly increased the scatter in M-$T_{\rm X}$ possibly by making the average temperature more sensitive to structure outside the core. Second, even with the cores removed the improvement in mass-estimates obtained using substructure information remains. Based on these results, it appears that centroid variation is the best substructure statistic to use when including a substructure correction in the M-$T_{\rm EW}$ relation. However, the correlations we have found in this sample of simulated clusters might not hold in samples of real clusters, because relaxed clusters in the real universe tend to have cooler cores than our simulated clusters do.

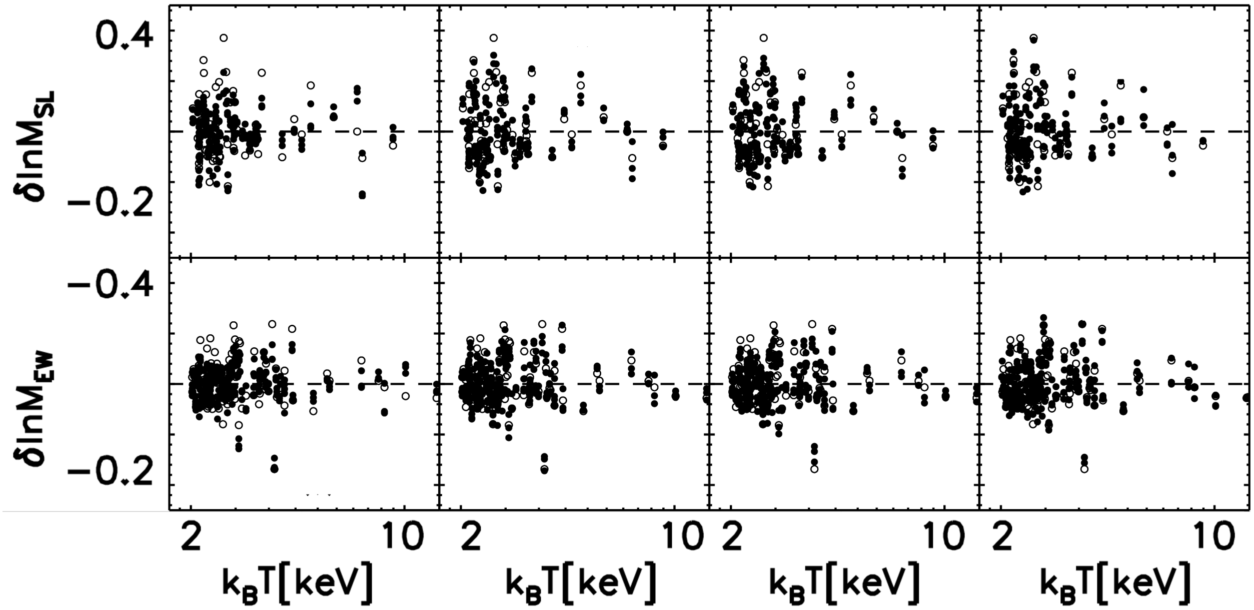

Figure 2.9: Comparison of mass offset $\delta \ln M$ between true mass and predicted mass, based on the $M(T_{\mathrm{X}})$ relation (open circles) and the $M(T_{\mathrm{X}}, S)$ relation (filled circles). Upper panels are for T_{SL} and lower panels are for T_{EW}. The standard deviations σ in the residuals are given in each plot.

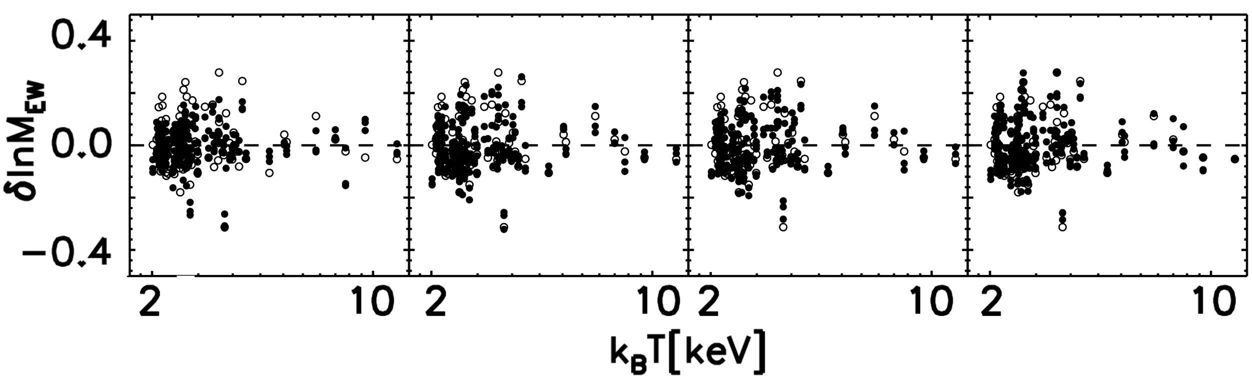

Figure 2.10: Comparison of mass offset $\delta \ln M$ between true mass and predicted mass, based on the $M(T_{\mathrm{X}})$ relation (open circles) and the $M(T_{\mathrm{X}}, S)$ relation (filled circles). These results are for are for T_{EW}, with the central 0.15 R_{500} region removed both from the average temperature and from the substructure measures. The standard deviations σ in the residuals are given in each plot.

Chapter 3

Temperature Structure and Mass-Temperature Scatter in Galaxy Clusters

3.1 Introduction

Galaxy clusters play an important role in precision cosmology that complements other techniques like Type Ia supernovae luminosity-distance relation measurements [Perlmutter et al.(1999), Riess et al.(1998)], baryonic acoustic oscillations (BAOs) angular-distance relation measurements [Eisenstein et al.(2005)], and observations of the cosmic microwave background radiation (see [Frieman et al.(2008)] for a review). For example, [Vikhlinin et al.(2009)] exploit dark energy's influence on the growth of structure by using 37 moderate-redshift and 49 low-redshift clusters to measure the shape of the galaxy-cluster mass function and its redshift evolution, which constrain the dark-energy density parameter Ω_Λ to 0.83 ± 0.15 in a non-flat ΛCDM cosmology and the dark energy equation of state parameter w_0 to -1.14 ± 0.21 in a flat cosmology. [Mantz et al.(2010)] have obtained similar results from measurements of the evolving number density of the largest clusters in order to constrain w_0 to -1.01 ± 0.20.

Strategies like these that compare model predictions to galaxy-cluster sample statistics inevitably confront sample error and sample bias. Future surveys expected to gather samples of 10–40 thousand galaxy clusters[1] will maximize survey reach while maintaining sufficient observation quality in order to minimize sample error, but they still must grapple with a major source of sample bias, which is scatter in the relationship used to infer cluster mass from an observable mass proxy. An important mass-observable relation for galaxy cluster studies connects dark matter halo mass to the temperature of the intracluster medium (ICM) inferred from its X-ray spectrum (its "X-ray temperature" T_X). In this chapter we investigate the possibility of correcting for scatter in this relation using temperature-inhomogeneity in the ICM, and discuss challenges that may exist in such a program.

A significant amount of uncertainty in the dark-energy constraints obtainable from large cluster surveys derives from uncertainty in scatter about the mean scaling relations obeyed by galaxy clusters' bulk properties [Lima & Hu(2005), Cunha & Evrard(2010)]. The key galaxy cluster property to measure when trying to constrain dark energy with clusters is the cluster's mass, which cannot be directly observed. Theoretical considerations predict correlations among halo mass and more readily observed cluster properties, like its galaxy richness, the velocity dispersion of its galaxies, T_X, the Sunyaev-Zel'dovich decrement, the gas mass, and $Y_{\rm X}$ parameter, which is the product of T_X and the gas mass inferred from X-ray observations [Kravtsov et al.(2006)]. Theory also predicts intrinsic scatter in these relations owing to variation in cluster dynamical state [Stanek et al.(2010), Fabjan et al.(2011), Rasia et al.(2012)].

One way to deal with intrinsic scatter is to join a cluster model to a cosmological model and simultaneously fit for the parameters of both, leveraging the statistical power of large surveys and "self-calibrating" the mass-observable relations. Another approach is to combine observables that tend to depart from the expected scaling relations in opposite ways, yielding

[1] http://www.mpe.mpg.de/heg/www/Projects/EROSITA/main.html

a new, low-scatter composite observable. An example low-scatter composite observable is $Y_{\rm X}$, since at a given halo mass, offsets in the measured gas mass at fixed total mass tend to anti-correlate with offsets in the measured temperature [Kravtsov et al.(2006)].

Another family of low-scatter composite observables attempt to measure structural variation directly. Mergers, relaxation, and non-adiabatic processes like radiative cooling, star formation, and feedback ought to leave a visible imprint that may allow us to measure and correct for scatter. For example, one might use imaging to quantify resolved morphological substructure. [Jeltema et al.(2008)] apply two observationally-motivated structure measures, the power ratios [Buote & Tsai(1995)] and the centroid shift [Mohr et al.(1993)], to a sample of galaxy clusters simulated with *Enzo* [Norman & Bryan(1999), O'Shea et al.(2004)]. They find that cluster structure correlates strongly with bias in mass estimates derived from T_X under the assumption of hydrostatic equilibrium and accounting for cluster structure can be used to correct some of the bias. Similarly, [Ventimiglia et al.(2008)] apply the power ratios, centroid shift, and axial ratio [O'Hara et al.(2006b)] substructure measures to the same sample of simulated clusters used in this chapter, and find that cluster substructure correlates with departures from the mean M-$T_{\rm X}$ relationship in the sense that clusters with more substructure tend to have a lower temperature at a given mass, and can be used to refine mass estimates derived from the ICM X-ray temperature. [Piffaretti & Valdarnini(2008)] likewise find that greater substructure, as quantified with power ratios, correlates with lower temperature at a given mass. [Yang et al.(2009)] find a strong correlation between mass-temperature scatter and halo concentration in their sample of simulated clusters, with cooler clusters appearing more concentrated than warmer clusters at similar mass.

[Jeltema et al.(2008)] observe, however, that line-of-sight projection effects lead to significant uncertainties in morphologically-derived substructure measures. Substructure also becomes more difficult to resolve at high redshift. Spectral signatures of dynamical state are therefore attractive because they are aspect-independent and redshift-independent. One such spectral signature of dynamical state is the "temperature ratio" T_{HBR} [Mathiesen & Evrard(2001), Cavagnolo et al.(2008)], which divides a "hardband" spectral-fit temperature by a "broadband" spectral-fit temperature. An energy cut applied to a broadband spectrum produces a hardband spectrum and serves to filter out cooler line-emitting components of the ICM. [Mathiesen & Evrard(2001)] studied the effects of relaxation on the observable properties of galaxy clusters, using a sample of numerically-simulated galaxy clusters generated by [Mohr & Evrard(1997)]. They found that hardband (2.0–9.0 keV) X-ray spectral fit temperatures average ∼20% higher than broadband (0.5–9.0 keV) temperatures and suggested that this effect may signal the presence of cool, luminous sub-clusters lowering the broadband temperature. [Valdarnini(2006)] corroborated these findings in simulations that included radiative cooling.

Figures 3.1 and 3.2 illustrate the effect. Both show a counts spectrum and single-temperature fit for a typical, unrelaxed cluster in our sample, with an aperture set at R_{2500} and a core region out to $0.15R_{2500}$ excised. Figure 3.1 is for a single-temperature model fit to the broad band, while figure 3.2 is for the hard band. Note the excess emission relative to the model above 4.0 keV and the deficit below 2.5 keV that arises because the model cannot simultaneously fit both a hot component and a cooler, line-emitting component [Mazzotta et al.(2004)]. Figure 3.2 shows the same spectrum, but with the residuals for a model fit just to the hard band. In this case the fit is much better over the range from 2.0 to 7.0 keV but under-predicts the emission below 2.0 keV.

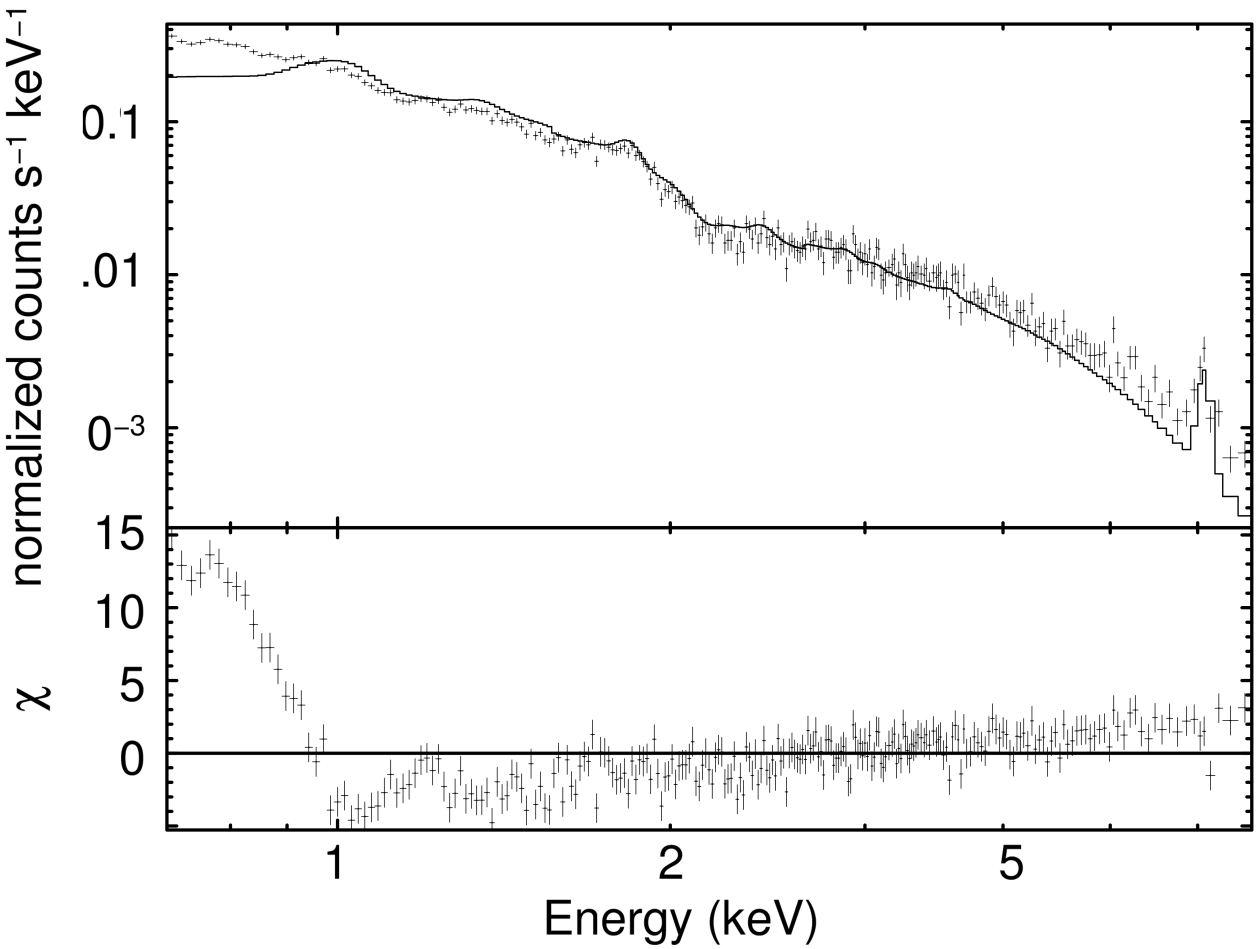

Figure 3.1: X-MAS simulated counts spectrum for a simulated cluster that appears to have significant temperature structure. A single-temperature MEKAL model fit to the [0.7–7.0] keV broad band is over-plotted as the solid line, with $k_B T = 2.42 \pm 0.03$ keV. Fit residuals appear in the bottom panel. This figure illustrates qualitatively the effect that additional cool components have on a single-temperature fit.

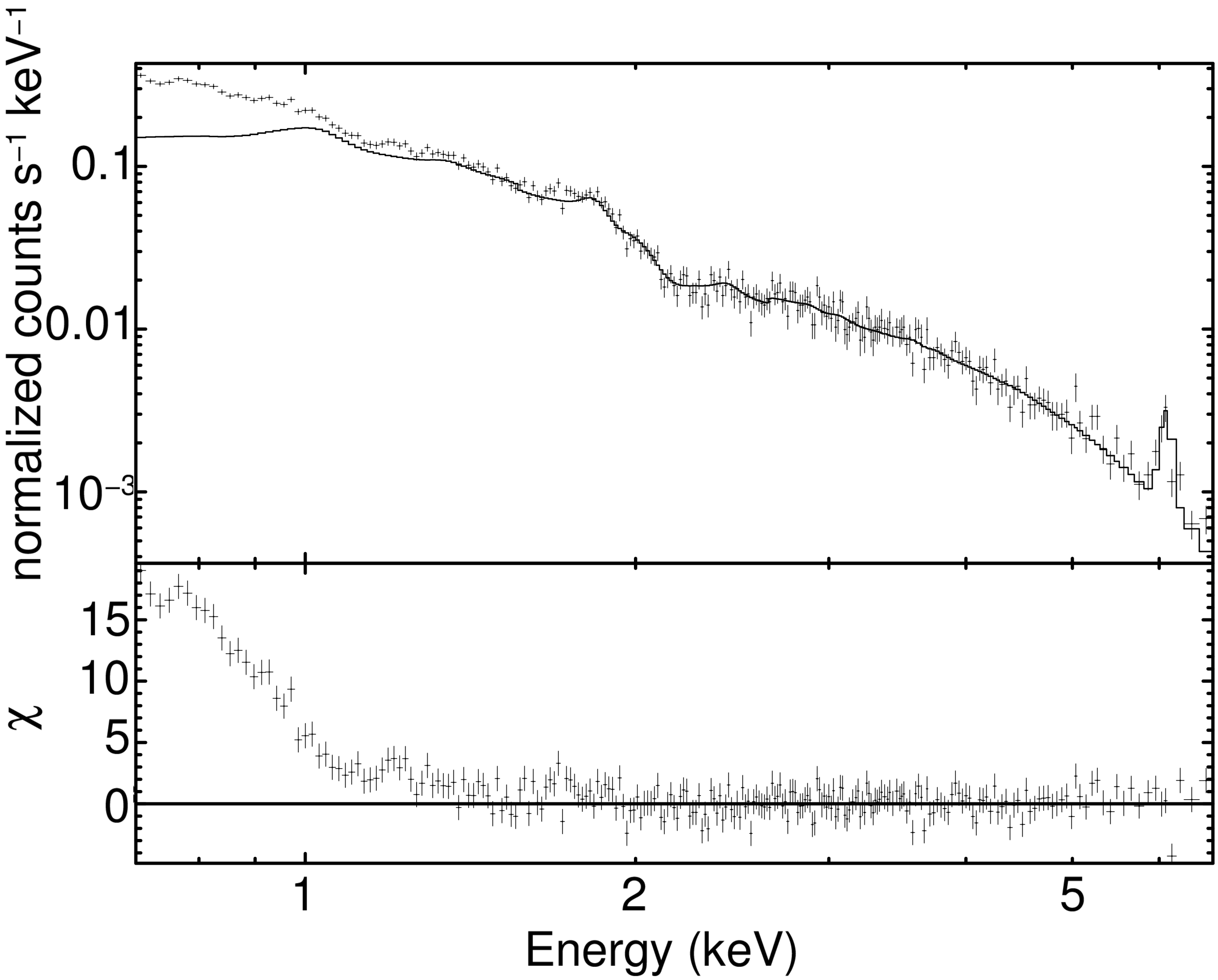

Figure 3.2: X-MAS simulated counts spectrum for the same simulated cluster as in the previous figure. A single-temperature MEKAL model fit to the [2.0–7.0] keV hard band is over-plotted as the solid line, with $k_B T = 3.52 \pm 0.2$ keV. Fit residuals appear in the bottom panel.

[Mathiesen & Evrard(2001)] suggested that the temperature skewing they observed might indicate a real temperature skewing detectable in real clusters using *Chandra*. Other researchers, including [Cavagnolo et al.(2008)] fit single-temperature emission models to the hard band (2.0–7.0 keV) and broad band (0.7–7.0 keV) for a large (N = 192) sample of clusters with observations selected from the *Chandra* Data Archive. These authors show that for a large, heterogeneous sample of clusters across a broad temperature range, the distribution of $T_{\rm HBR}$ has a mean of 1.16 and an rms deviation $\sigma = \pm 0.10$, with $T_{\rm HBR}$ tending to be larger in merging systems. They also report that while this signal is significant in the aggregate, the errors for any single $T_{\rm HBR}$ measurement and the scatter across all of the measurements together pose challenges for any effort to use $T_{\rm HBR}$ either to select for merging systems or to obtain more accurate mass estimates. In order to meet these challenges it is important also to examine $T_{\rm HBR}$ and similar spectral signatures of dynamical state in a simulation context. Like the original study of [Mathiesen & Evrard(2001)], this chapter examines the temperature ratio for a sample of simulated clusters and simulated *Chandra* observations, and as in the subsequent study by [Valdarnini(2006)], the simulated clusters analyzed here were generated using a hydrodynamical code with radiative cooling included.

This chapter is organized as follows. In section 3.2, we describe the simulated clusters in our sample along with the X-MAS code for generating their mock X-ray observations. In section 3.3, we present our analysis methods and define the spectral signatures of dynamical state we examine. In section 3.4, we report and discuss our results, and section 3.5 summarizes our work.

3.2 Methods

3.2.1 Numerical Simulations

This study is based on an analysis of 118 clusters simulated using the cosmological hydrodynamics TREE+SPH code GADGET-2 [Springel(2005)], which were simulated in a standard Λ cold dark matter (ΛCDM) universe with matter density $\Omega_M = 0.3$, $h = 0.7$, $\Omega_b = 0.04$, and $\sigma_8 = 0.8$. The simulation includes radiative cooling assuming an optically-thin gas of primordial composition, with a time-dependent UV background from a population of quasars, and handles star formation and supernova feedback using a two-phase fluid model with cold star-forming clouds embedded in a hot medium. All but four of the clusters are from the simulation described in [Borgani(2004)], who simulated a box $192\,h^{-1}$ Mpc on a side, with 480^3 dark matter particles and an equal number of gas particles. The present analysis considers the 114 most massive clusters within this box at $z = 0$, which all have M_{200} greater than $5 \times 10^{13}\,h^{-1} M_\odot$. These are referred to as the B04 Sample in the remainder of this chapter. By convention, M_Δ refers to the mass contained in a sphere which has a mean density of Δ times the critical density ρ_c, and whose radius is denoted by R_Δ

That cluster set covers the $\sim$1.5-5 keV temperature range, but the $192\,h^{-1}$ Mpc box is too small to contain significantly hotter clusters. We therefore supplemented it with four clusters with masses $> 10^{15}\,h^{-1}\,M_\odot$ and temperatures $>$ 5 keV drawn from a dark-matter-only simulation in a larger $479\,h^{-1}$ Mpc box [Dolag & Stasyszyn(2009)], referred to in this chapter as the D09 sample. The cosmology for this simulation also was ΛCDM, but with $\sigma_8 = 0.9$. These were then re-simulated including hydrodynamics, radiative cooling, and star formation, again with GADGET-2 and using the zoomed-initial-conditions technique of [Tormen(1997)], with a fourfold increase in resolution. This is comparable to the resolution of the clusters in the smaller box. Adding these four massive clusters to our sample gives a total of 118 clusters with M_{200} in the range $5 \times 10^{13}\, h^{-1} M_{\odot}$ to $2 \times 10^{15}\, h^{-1} M_{\odot}$. The mean structural properties of massive clusters drawn from a sample with $\sigma_8 = 0.9$ may differ somewhat from those of similar-mass clusters in a $\sigma_8 = 0.8$ universe because they reflect a more advanced state of cosmic evolution. However, these four additional clusters carry minimal statistical weight in the context of the overall sample. They are included primarily to evaluate whether the mean and dispersion of their $T_{\rm HBR}$ values are consistent with those of the lower-mass systems.

3.2.2 X-Ray Simulations

The simulated galaxy clusters in our sample are processed with the *X-ray Map Simulator* version 2 (X-MAS) [Gardini et al.(2004), Rasia et al.(2008)] to generate X-ray images suitable for standard *Chandra* reduction techniques. In its first step X-MAS uses the outputs of the hydrodynamic code to calculate the emissivity of each simulation element within the chosen field of view and to project this onto the image plane. In its second step it convolves the resulting flux with the appropriate response of a given detector. In the case of our simulated *Chandra* observations, the second step applies the response matrix file and ancillary response file for the ACIS S3 CCD, with a 200 kilosecond exposure time. In order to separate out potential calibration issues from the focus of this particular study, these response matrices implement a constant response over the detector, and in generating the simulated X-ray images, the evolved zero-redshift clusters are shifted to a redshift sufficient to fit R_{500} within the 16 arcminute field of view. Because of this step, though the clusters in the sample are distributed over a range of physical sizes, they all have approximately the same apparent size projected onto the image plane and into the simulated observations.

3.2.3 M-T_{X} Relation

In this chapter, cluster mass refers to M_{200}, while T_X refers to our estimated "spectral-fit temperatures" obtained using XSPEC [Arnaud(1996)] to fit single-temperature MEKAL plasma models to various energy bands in simulated X-MAS X-ray observations taken from the numerically-simulated clusters. The steps involved in the process are described in detail in § 3.3.

Figure 3.3 shows the mass-temperature relation based on our sample of simulated clusters and estimated spectral fit temperatures, measured in a broad 0.7–7 keV band within an annular aperture from $0.15R_{500}$ to R_{2500} as in [Cavagnolo et al.(2008)]. The best fits to the power-law form

$$M = M_0 \left(\frac{T_{\mathrm{X}}}{2\,\mathrm{keV}} \right)^{\alpha} \tag{3.1}$$

have the coefficients $M_0 = 1.09 \pm 0.01 \times 10^{14}\ h^{-1} M_{\odot}$, $\alpha = 1.57 \pm 0.06$ for the full sample of clusters. For the subset of clusters with $T_{2.0-7}>$ 2.0kev, the best-fit parameters are $M_0 = 1.06 \pm 0.02 \times 10^{14}\ h^{-1} M_{\odot}$, $\alpha = 1.71 \pm 0.07$. As is generally the case for simulated clusters, the power-law indices of the mass-temperature relations found here are consistent with cluster self-similarity and the virial theorem [Kaiser(1986), Navarro et al.(1995)]. These relationships have scatter, which we characterize by the standard deviation in log space $\sigma_{\ln M}$ about the best-fit mass at fixed temperature T_{X}. We find $\sigma_{\ln M} = 0.10$.

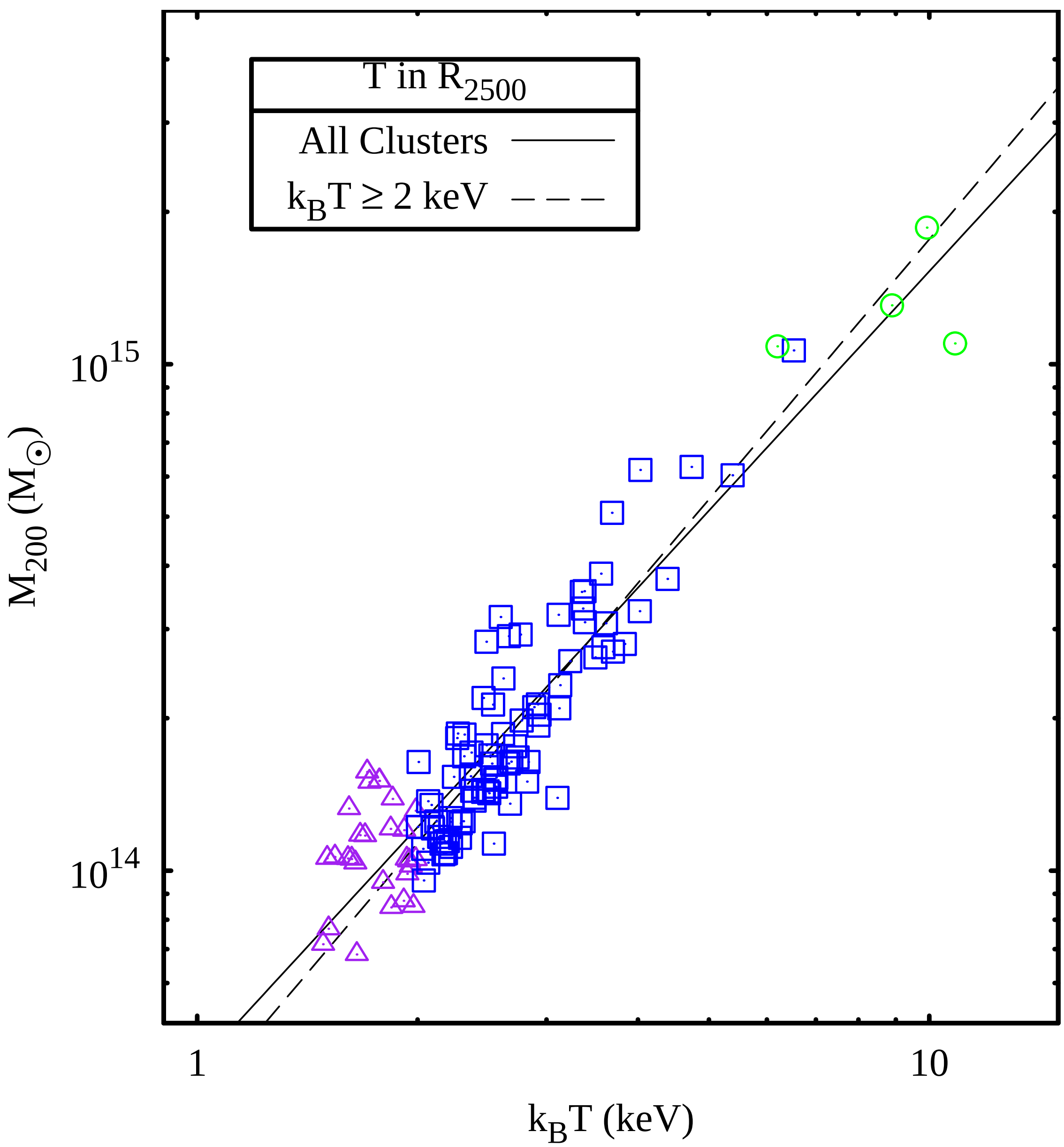

Figure 3.3: Mass-temperature (M-T_{X}) relation for the clusters in our sample. Clusters with $k_BT < 2$ keV are plotted in purple open triangles, while clusters with $k_BT \geq 2$ keV are plotted in blue open squares, and the four massive D09 clusters in green open circles. Mean relations are plotted with solid lines for the whole sample, and dashed lines for clusters with $k_BT \geq 2$keV. Finally, note that average temperatures are taken within a core-excised annulus whose outer radius is placed at R_{2500}. *For interpretation of the references to color in this and all other figures, the reader is referred to the electronic version of this dissertation.*

3.3 Analysis

3.3.1 Filtering

We use X-MAS to simulate X-ray observations—provided as standard *Chandra* event files—then subject them to a series of reduction steps using the *Chandra* Interactive Analysis of Observations package (CIAO) v4.1 [Fruscione et al.(2006)]. All of the event files have at least 100K counts, while those for the most luminous clusters have over half a million counts. Simulated observations of this quality provide us with an opportunity to address the question of how much of the scatter in our temperature-structure statistics is intrinsic. Consequently, our first reduction step filters each raw event file into a new set of event files by randomly sampling the events it records. The number of counts in each file is its "count level," and in order to cover the space of typical *Chandra* archival observations, we apply the filtering step to each of the raw event files four times, at count levels 15K, 30K, 60K, and 120K. These count levels roughly map to the range between observations of short duration or of relatively low surface-brightness objects to observations of long duration or of relatively high surface-brightness objects.

3.3.2 Cool Lump Excision

An example of a filtered event file appears in Figure 3.4 as a surface-brightness image. It displays a common feature of numerical simulations of galaxy clusters, which is the presence of relatively dense, cool, and metal-rich substructures that continuously undergo mass accretion and have not yet come into thermal equilibrium with the hot ICM surrounding them [Borgani & Kravtsov(2009)]. These bright point-like spots, or "cool lumps", typically are associated with the dense cool cores of smaller halos that have merged with the primary halo. Generally regarded as an unphysical artifact of numerical simulations, at least insofar as their temperatures, densities, and concentrations are concerned, commonly they are excised before further analysis is conducted [Rasia et al.(2006), Piffaretti & Valdarnini(2008), Nagai et al.(2007)].

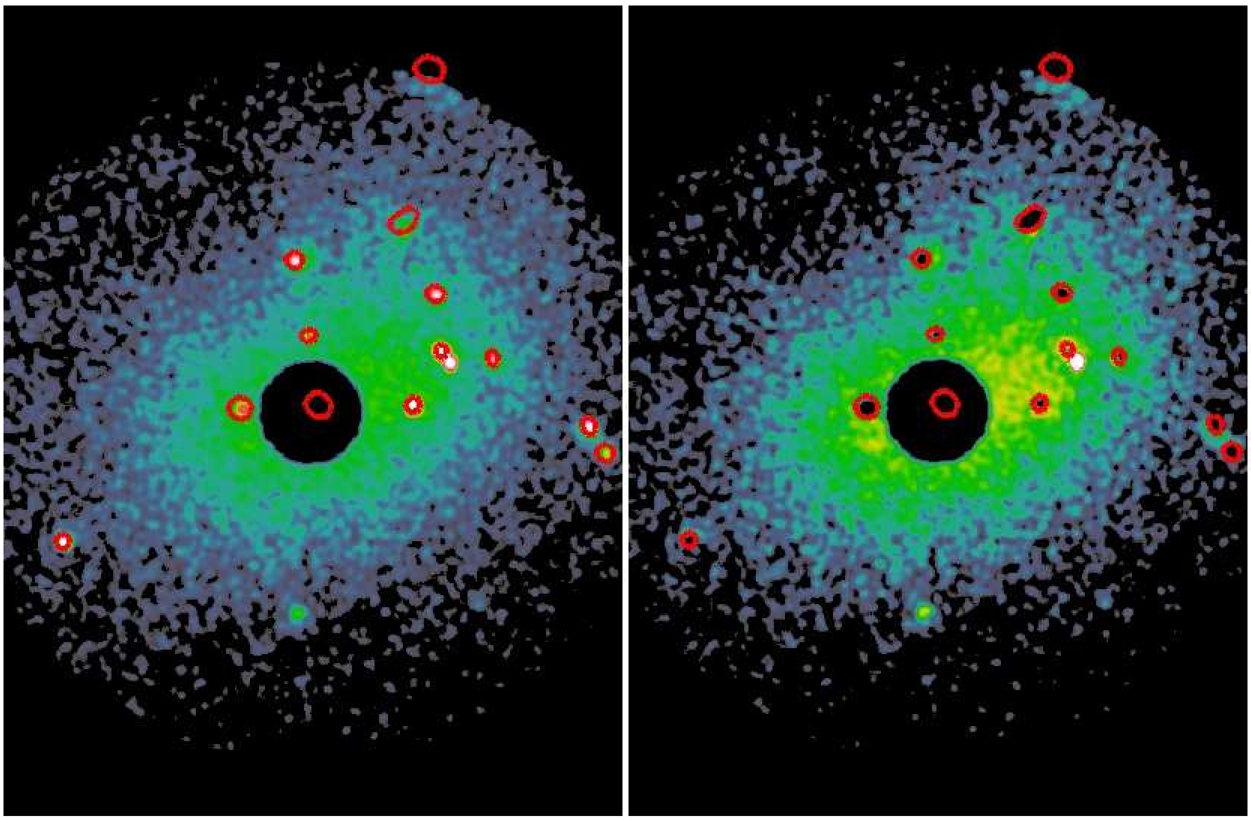

Figure 3.4: X-MAS simulated X-ray surface-brightness images for the same cluster whose spectrum is presented in the previous figure. The aperture is set at R_{2500} and a core region of size $0.15R_{2500}$ is excised. Note the surface-brightness peaks in the image. In this study these are detected automatically by the CIAO tool wavdetect, which generates source regions identified in this figure by red ellipses. Labeled "cool lumps" in this analysis, they are subjected to varying degrees of excision, from no masking (*left*) to full masking (*right*), as described in the text.

In order to study the effect that excising cool lumps has on measures of temperature substructure, we produce from the originals several new event files whose cool lumps have been excised to an increasing degree. The CIAO `wavdetect` tool identifies peaks in the photon distribution by correlating an event file's image with a sequence of "Mexican-Hat" wavelet functions of differing scale sizes, measured in pixels, then generates a source list with associated region files. We use its default sequence of wavelet scale sizes in this analysis (2 and 4 pixels), though we apply the tool four times to each filtered event file, each time incrementing the multiplicative factor by which the source regions are scaled. In CIAO `wavdetect`, the parameter governing this multiplicative factor is `ellsigma` and in our study ranges between 0 to 3. A value of 0 for `ellsigma` is equivalent to "no masking" while a value of 3 corresponds to what we call "full masking". The effect is to produce versions of each cluster observation with a range of masking. Note that the wavelet scale size is a constant fraction of the cluster size because all the clusters have been redshifted so that R_{500} fits in the field of view.

We finish the extraction phase of our analysis with the following steps. First, for every excised file we apply an aperture of R_{2500} and excise the central 0.15 R_{2500} region, generating new copies of the event files. This step, including the centering algorithm, matches the procedure in [Cavagnolo et al.(2008)] so that regions measured in the simulated clusters correspond to those in the *Chandra* archival observations. Next, each fully-processed event file is extracted into a standard pulse-invariant (PI) spectral file binned so as to have at least 25 counts in each energy channel. The extraction phase is complete when each original raw event file generates PI spectral files suitable for spectral fitting in XSPEC.

3.3.3 Spectral Fitting

The PI spectral files are then fed into XSPEC v12.5.0 for spectral fitting. In order to form the temperature ratio T_{HBR} two fits are performed for each spectrum. The first fit is over the hard band from $2.0(1+z)^{-1}$–7 keV, for which the $(1+z)^{-1}$ factor exists in order to shift the 2 keV cutoff from the observer's frame to the cluster's rest-frame. The simulated clusters occupy a range of redshifts because larger clusters are translated to higher redshifts in order to fit R_{500} within 16 arc-minutes, when creating artificial observations. The second fit is over the broad band, including all energy channels in the spectrum from 0.7–7 keV. Every fit is made by minimizing the χ^2 statistic for a single-temperature MEKAL model multiplied by a warm-absorber (WABS, to account for Galactic absorption). The Galactic column is fixed to $N_H = 5 \times 10^{20}$ cm^{-2} and the metallicity to 0.3 Solar, leaving the temperature of the emission component, its H density (although this makes no difference), and its normalization as the only free parameters.

3.3.4 Quantifying Temperature Structure

We adopt two spectral measurements of temperature structure. The first is the temperature ratio T_{HBR} of [Cavagnolo et al.(2008)] and is found in the following way. For each simulated cluster in our sample, for each count level (15K, 30K, 60K, 120K), and for each cool lump masking level (0, 1, 2, 3), we find a spectral-fit temperature in the hard band and the broad band and form the temperature ratio T_{HBR}. Emission from cooler, line-emitting metal-rich parts of the ICM ought to be excluded from the hard band, so we expect that a T_{HBR} value greater than unity signals the presence of merging sub-clumps.

Our second measure of temperature, which we call the "cool residual," (RES_{cool}) compares an observation's actual broadband count rate to a model-predicted count rate for a spectral model fit only over the hard band. Again, we determined a spectral-fit temperature for each combination of cluster, count level, and masking level, except that in this case we performed only a hardband fit. Since emission from cooler components should be excluded from this band, in general we achieve good fits even when the count level is sufficiently high that broadband fits may formally have large reduced χ^2 values. From this hardband model fit we estimate the corresponding broadband count rate and calculate its percentage deviation from the actual broadband count rate. While single-temperature systems will have actual count rates that are essentially the same as their model count rates, the introduction of cooler, luminous substructure components should generate an excess broadband count rate relative to the model. This measure of temperature substructure avoids the uncertainties associated with a single-temperature fit to the broad band.

3.4 Results and Discussion

Having calculated spectral-fit temperatures, T_{HBR}, and the cool residual for all of the clusters in our sample, we have the means to study how well temperature structure correlates with departures from the mean M-T_{X} relation, and how well these measures can be used to obtain better mass estimates. We will also examine how our results depend on the removal of the cool lumps.

3.4.1 T_{HBR} from Simulations.

We present in Figure 3.5 the temperature ratios T_{HBR} for our simulation sample, plotted as a function of the broadband temperature fit $T_{0.7-7}$. This figure is similar to Figure 8 in

[Cavagnolo et al.(2008)], which shows that the mean value of T_{HBR} observed among clusters in the *Chandra* archive is $\langle T_{\mathrm{HBR}} \rangle = 1.16$, with a standard deviation of $\sigma_{\mathrm{THBR}} = 0.10$. We remind the reader of important differences between the two samples being considered. The *Chandra* archive sample of [Cavagnolo et al.(2008)] contains clusters most of which have $k_B T > 3$ keV, whereas most of the clusters in our sample have $k_B T < 3$ keV. Nevertheless, even with that caveat the temperature ratios of the simulated clusters are distributed in approximately the same way as are those in the real sample of [Cavagnolo et al.(2008)], with $\langle T_{\mathrm{HBR}} \rangle = 1.12$ and $\sigma_{\mathrm{THBR}} = 0.11$, provided the cool lumps are not excised (circles in Figure 3.5). When the cool lumps are excised (squares in Figure 3.5), the mean and variance of T_{HBR} diminish, with $\langle T_{\mathrm{HBR}} \rangle = 1.07$ and $\sigma_{\mathrm{THBR}} = 0.07$. These values are for the full 120K count data, though the full set of $\langle T_{\mathrm{HBR}} \rangle$ for the four `ellsigma` values and four count values are tabulated in Table 3.1. This table provides mean values for T_{HBR} and its variance for all of the clusters in the sample, and for a subset whose $T_{2.0-7}$ value is greater than 2 keV. Much of the variance derives from the lower-temperature clusters, and as they are removed the variance in T_{HBR} drops significantly, especially when full masking is applied.

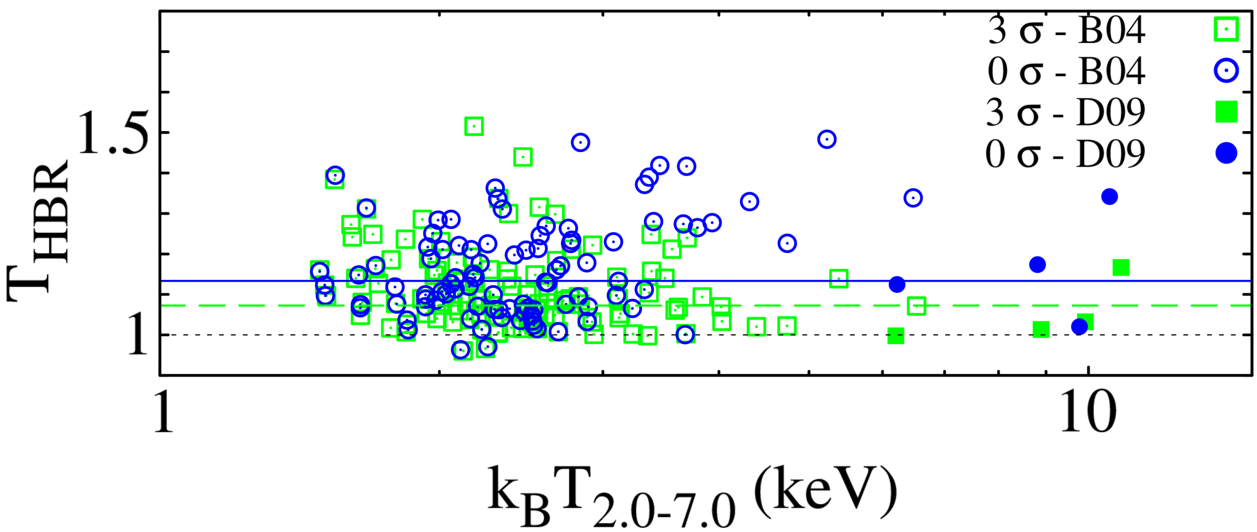

Figure 3.5: T_{HBR} plotted against $T_{0.7-7}$ for simulated X-MAS observations that have approximately 120K counts. Hydrodynamic simulations may produce spurious over-condensations of cool gas. These cool lumps can be excised using the CIAO tool wavdetect, whose aggressiveness can be controlled via its ellsigma parameter. Squares correspond to single-temperature MEKAL fits whose underlying observations are processed by wavdetect with ellsigma set to 3, and circles correspond to those with ellsigma set to 0. Finally, note that the 4 massive D09 clusters are denoted by filled symbols rather than by open symbols. The solid line represents the mean when cool lumps are not removed, while the dashed line represents the mean when they are removed. The dotted line indicates $T_{\text{HBR}} = 1$.

Figure 3.6 presents a similar effect for RES_{cool}. Here, we see that the excision of cool lumps again reduces the mean and variance of the temperature substructure measure, although in this case the effect is more dramatic. Evidently, the presumably unphysical cool lumps in simulated clusters may be necessary to reproduce the distribution of quantitative temperature substructure measures found in real clusters. This is a subject which we return to in Section 3.4.3.

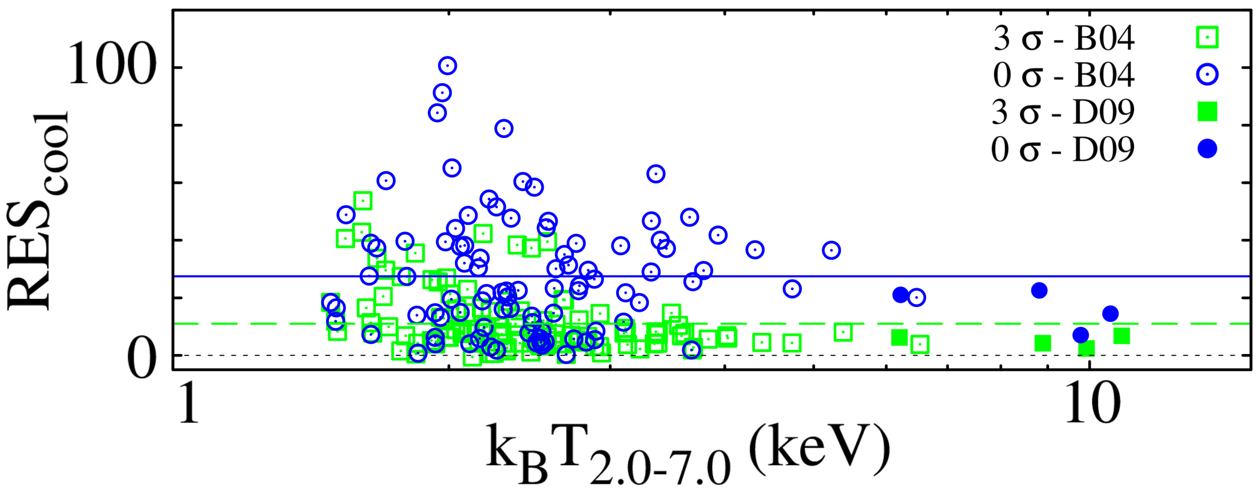

Figure 3.6: RES_{cool} plotted against $T_{0.7-7}$ for simulated X-MAS observations that have approximately 120K counts. This statistic tracks the percent excess count rate of the actual observation with respect to count rate for a MEKAL model fit to just the hard band. Squares correspond to single-temperature MEKAL fits whose underlying observations are processed by wavdetect with ellsigma set to 3, and circles correspond to those with ellsigma set to 0. As in the previous plot, the 4 massive D09 clusters are denoted by filled symbols rather than by open symbols. The solid line represents the mean when cool lumps are not removed, the dashed line represents the mean when they are removed, and the dotted line indicates zero residual.

3.4.2 Temperature Structure and Scaling Relations

Our original motivation for conducting this study was to determine if temperature structure, as quantified by the temperature ratio T_{HBR}, correlates with and can be used to correct for departures from the mean mass-temperature relation M-T_{X}. In order to test this idea, we define the "mass offset" at fixed temperature by the relation

$$\delta \ln M(T_{\mathrm{X}}) = \ln \left[\frac{M}{M_{\mathrm{pred}}(T_{\mathrm{X}})} \right] \tag{3.2}$$

where M is the cluster's actual mass, and M_{pred} is the mass predicted from the mean M-T_{X} relation. Figure 3.7 plots the mass offsets for our simulated clusters as a function of T_{HBR}, for the case in which predicted masses are derived from the M-T_{X} relation for the broadband spectral fit temperature. Values of T_{HBR} calculated both with cool lumps excised (squares) and without excision (circles) appear in this figure. Error bars on T_{HBR} are omitted for clarity. While there is some correlation, such that clusters with more temperature structure (larger T_{HBR}) tend to be more massive than predicted by the mean M-T_{X} relation, the trend is weak and has substantial scatter. Excising the cool lumps weakens the trend further. Figure 3.8 shows the same comparison for the RES_{cool} measure instead of T_{HBR}, and in this case we again find that excising the cool lumps has an even larger effect for T_{HBR} although in both cases accounting for temperature substructure does not greatly reduce scatter in mass offset.

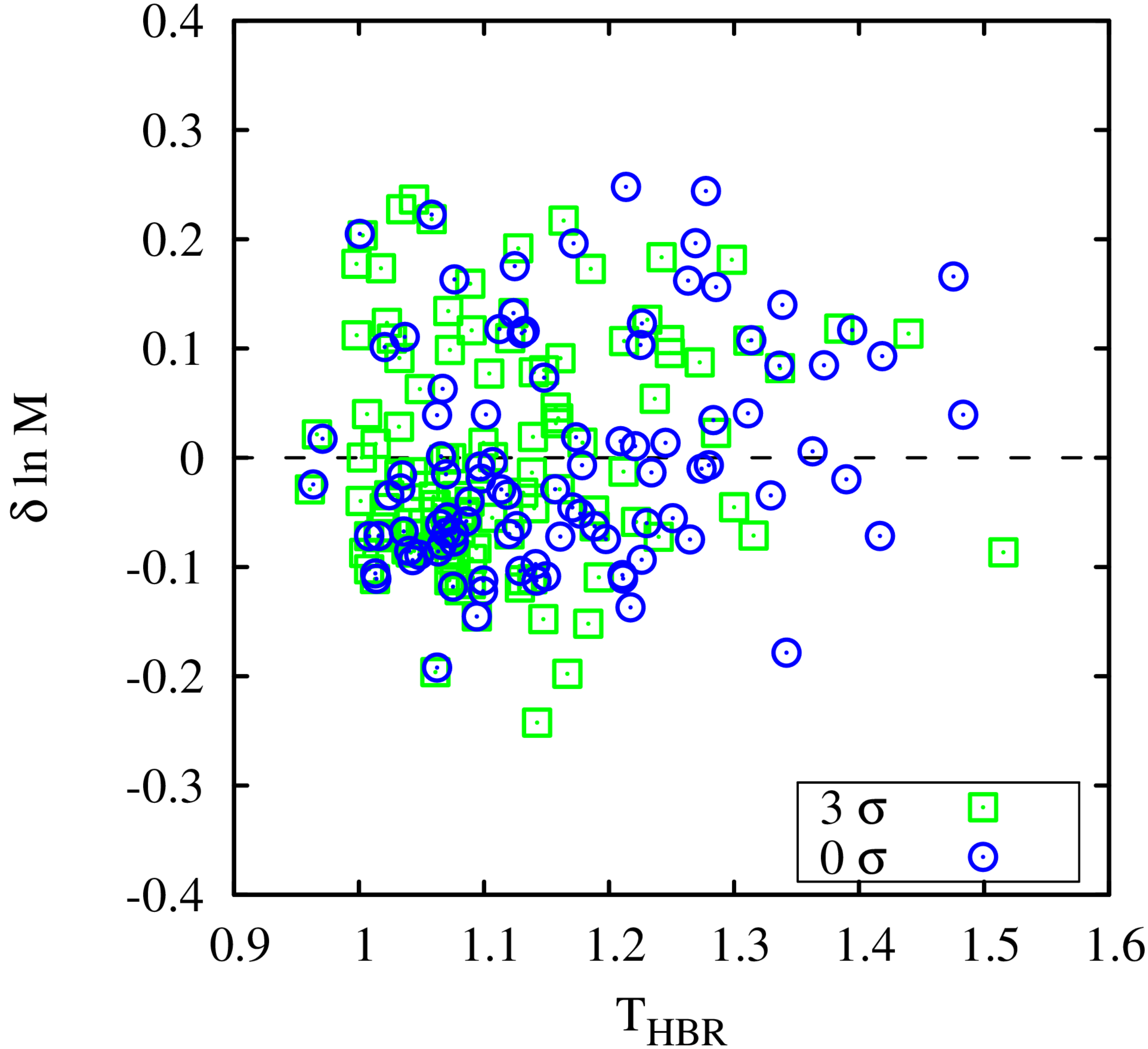

Figure 3.7: Relationship between $T_{\rm HBR}$ and mass offset $\delta \ln M(T_{\rm X})$ from the mean M-$T_{\rm X}$ relationship for the clusters in combined B04+D09 simulation sample. The temperatures in this relation are our broadband spectral-fit temperatures. Squares correspond to simulated X-MAS observations that are processed by wavdetect with ellsigma set to 3 (full masking), while circles correspond to observations that have ellsigma set to 0.

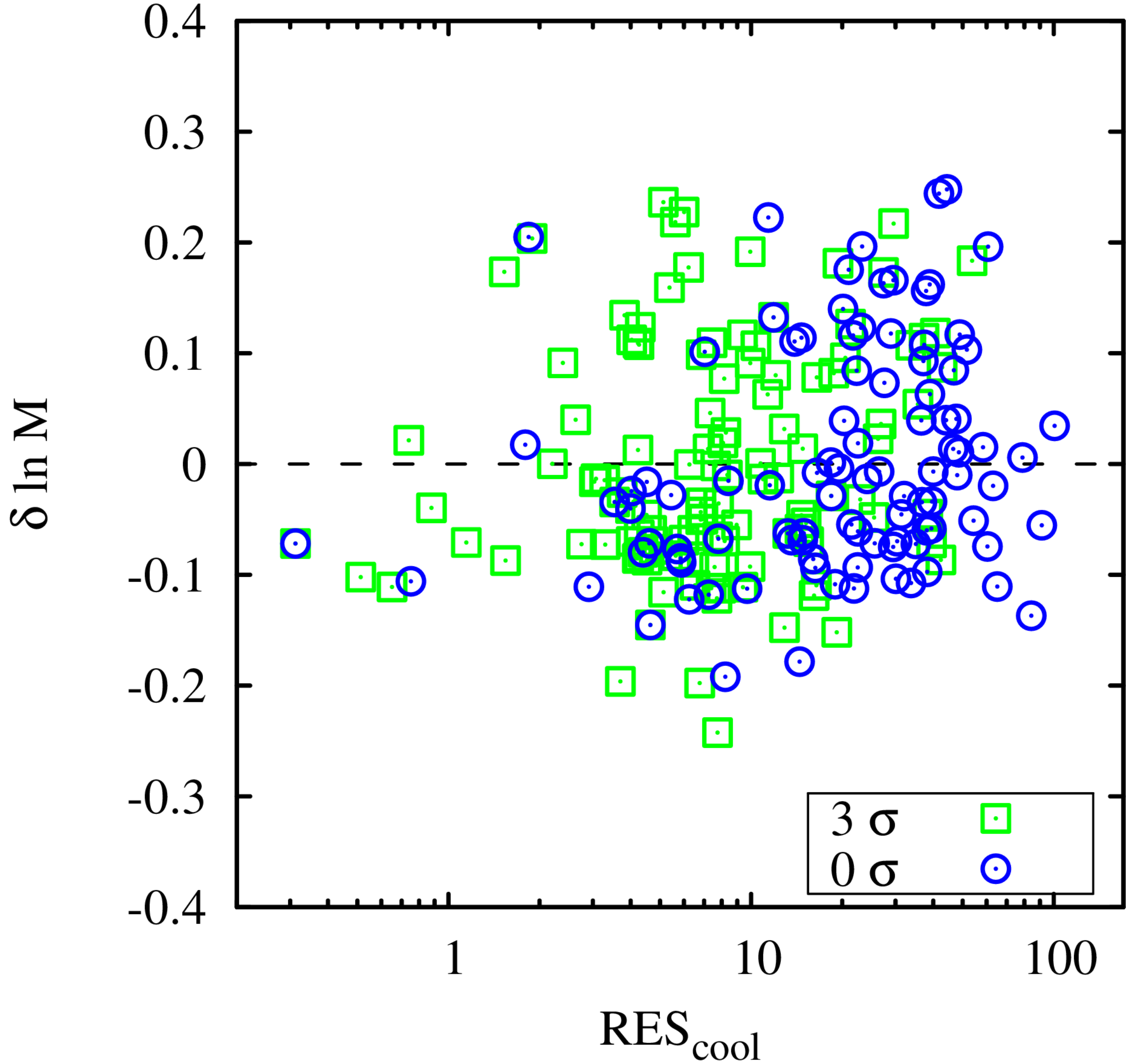

Figure 3.8: Relationship between RES_{cool} and mass offset $\delta \ln M(T_{\rm X})$ from the mean M-$T_{\rm X}$ relationship for the clusters in combined B04+D09 simulation sample. The temperatures in this relation are our broadband spectral-fit temperatures. Squares correspond to simulated X-MAS observations that are processed by wavdetect with ellsigma set to 3, while circles correspond to observations that have ellsigma set to 0.

3.4.3 Effects of Masking Strategy

We now examine the decline in T_{HBR} and its variance as cool lumps are excised, beginning with Figure 3.9, which focuses on T_{HBR}. Here, we plot the statistic's standard deviation σ_{THBR} as a function of the two dimensions along which we adjust our analysis pipeline, with the top panel devoted to the masking strategy, and the bottom panel devoted to the count level. Focusing on the top panel, we see that increasing the `ellsigma` parameter of the CIAO `wavdetect` tool from 0 to 3 reduces σ_{THBR} from 0.15 down to 0.13, when the observations are relatively "poor" (with ∼15K counts). With higher-quality observations of 60K or 120K counts, the decline is in σ_{THBR} greater, going from 0.12 down to 0.07 as the `ellsigma` parameter rises from 0 to 3, and σ_{THBR} for full masking ends up being significantly less than the value of 0.10 observed in the [Cavagnolo et al.(2008)] sample.

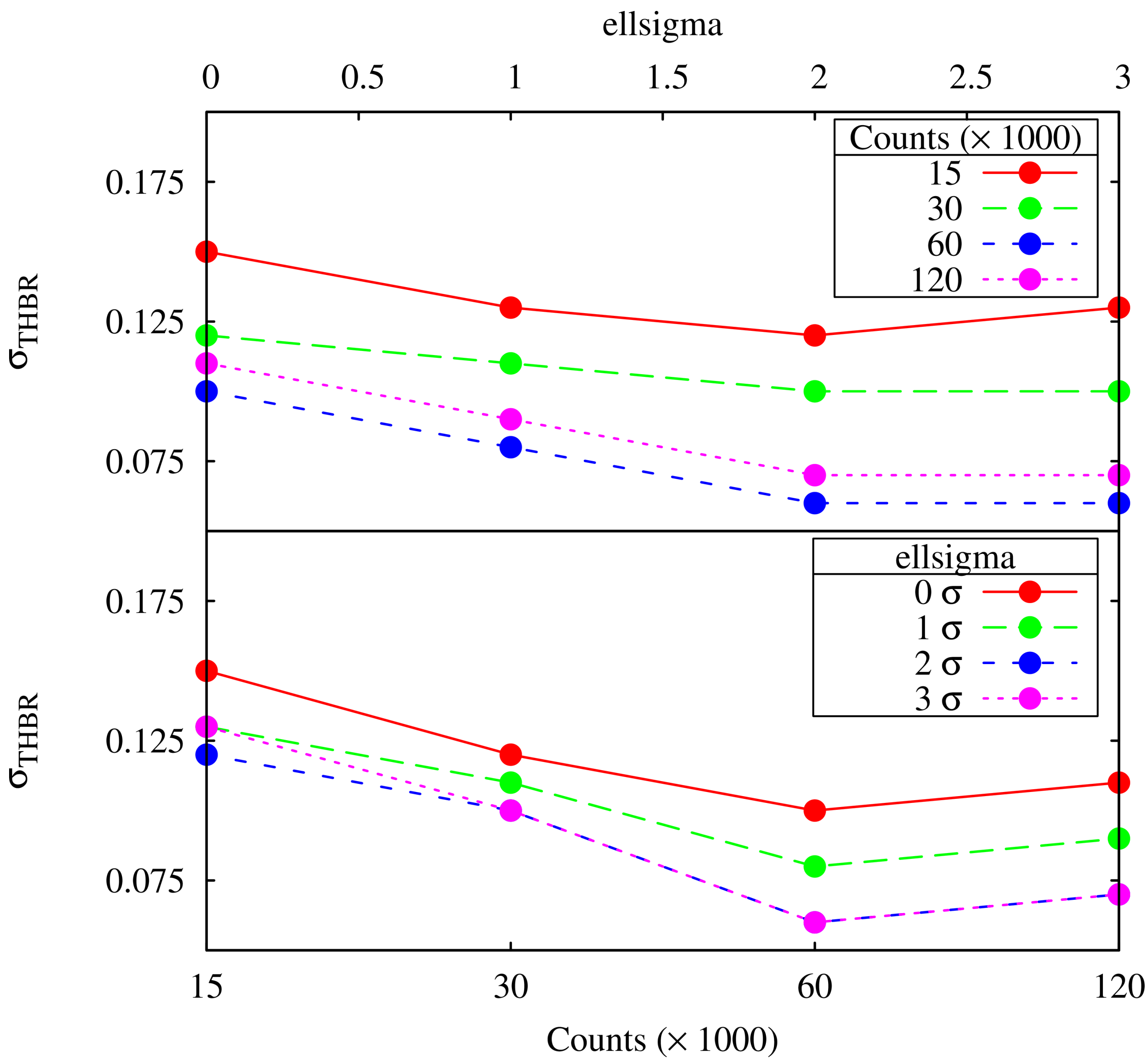

Figure 3.9: (*top*) Decline in the T_{HBR} standard deviation σ_{THBR} as wavdetect's ellsigma parameter ranges from 0 to 3. These are plotted for a family of simulated observations of increasingly higher quality, from approximately 15k counts to approximately 120k counts. (*bottom*) Decline in σ_{THBR} as simulated X-MAS observations go from lowest-quality (approximately 15k counts) to highest-quality (approximately 120k counts). These are plotted for a family of simulated observations with wavdetect's ellsigma parameter ranges from 0 to 3.

Figure 3.10 helps show why the temperature ratio T_{HBR} and its variance decline as the cool lumps are removed. It plots the sample average of the relative change in temperature as the CIAO `wavdetect ellsigma` parameter is increased. As more of each cool lump is excised, both the broadband spectral fit temperature, and the hardband fit temperature increase. However, the increase is significantly larger for the broadband temperature, as the cool lumps' contribution to the flux is already largely excluded from the hardband fits. The top panel in this figure shows this effect for spectra with approximately 120K counts, while the bottom panel is for spectra with approximately 15K counts.

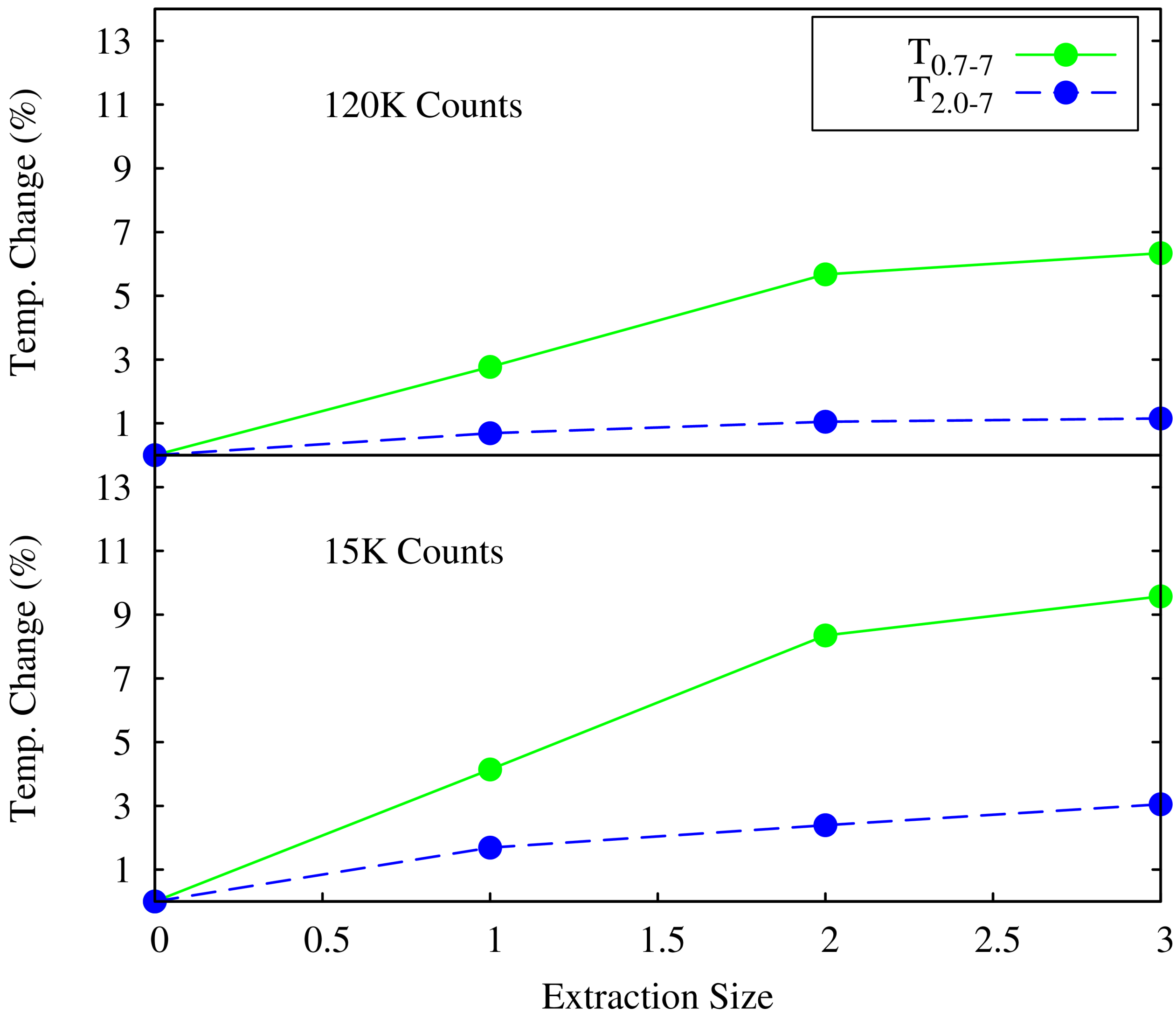

Figure 3.10: Relative change in spectral fit temperatures as the cool lumps are removed from the simulated clusters for high-quality simulated observations. (*top*) Observations with approximately 120K counts. (*bottom*) Observations with approximately 15K counts. Note that these are for observations in an aperture corresponding to R_{2500}.

Another way of visualizing the effect of more aggressive masking is depicted in Figure 3.11. The top panel in this figure is similar to Figure 3.6 in that it occupies the $T_{0.7-7}$–$T_{\rm HBR}$ plane, with $T_{\rm HBR}$ plotted as a function of $T_{0.7-7}$ for our simulated clusters. Arrows illustrate the shift in $T_{\rm HBR}$ and in $T_{0.7-7}$, as the cool lumps are excised. Some of the clusters experience very large shifts in both quantities, while others experience no shifts at all. The former are associated with clusters that have many well-defined and bright cool lumps, while the latter correspond to those clusters that are completely free of cool lumps. The bottom panel in this figure shows just the size of this shift for the $T_{\rm HBR}$ statistic, from which we can see that some clusters indeed have a shift of precisely 0. Again, these are clusters whose simulated X-ray observations are unchanged after applying the CIAO `wavdetect` tool because it finds no sources to mask out. Comparing Figure 3.11 and 3.12, we also see that the dependence of the broadband spectral-fit temperature on the aggressiveness of masking does not depend strongly on aperture size.

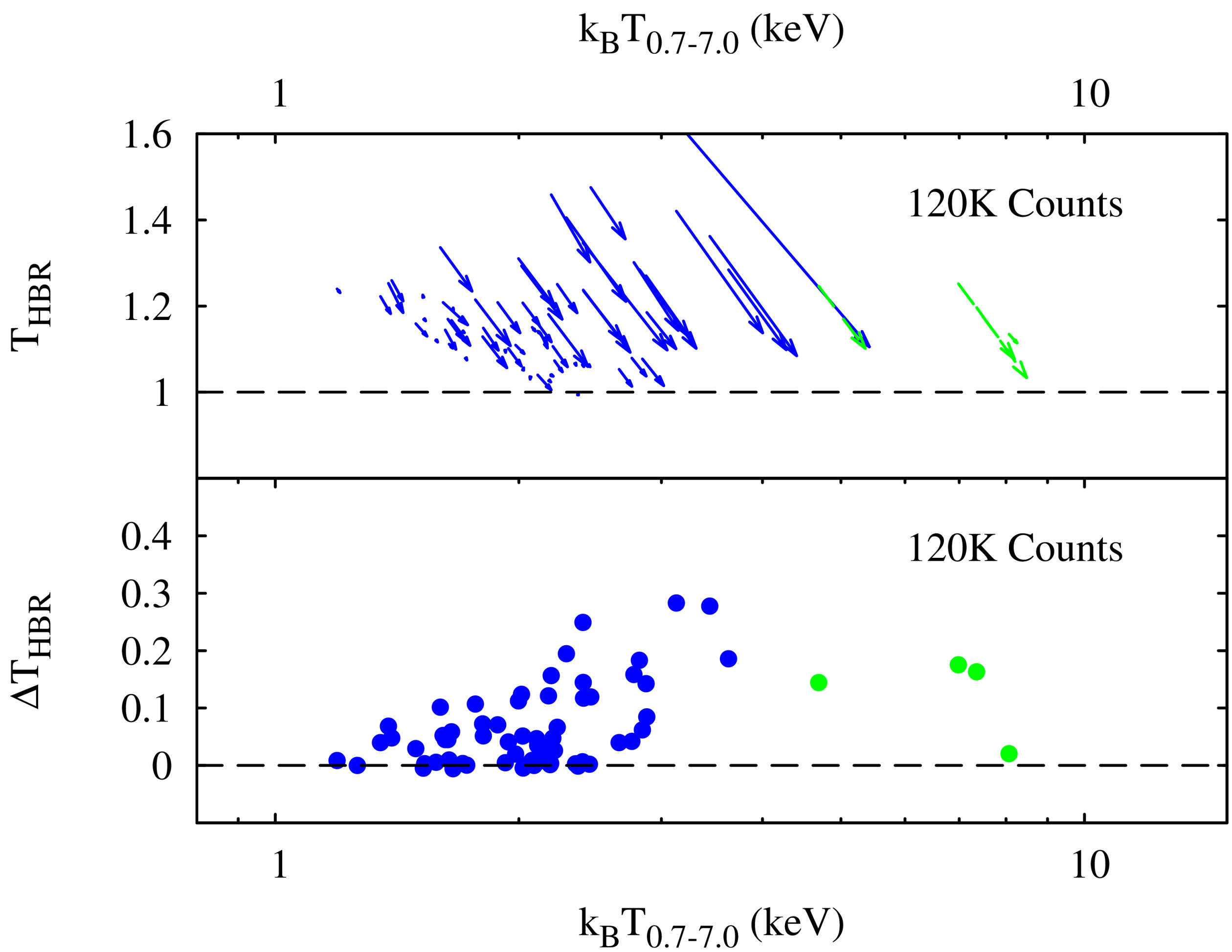

Figure 3.11: (*Top*) Shift in the $T_{0.7-7}$-$T_{\rm HBR}$ plane as wavdetect's ellsigma parameter ranges from 0 to 3. Clusters from the B04 sample are depicted with solid arrows, while clusters from the D09 sample are depicted with long-dashed arrows. broadband spectral-fit temperatures are estimated within an aperture set at R_{2500}. Notice that the distribution of most of the points shifts significantly to higher spectral fit temperatures and smaller temperature ratios as cool lumps are excised. Notice also that some simulated clusters are unafflicted by cool lumps, so that their net shift is 0. (*Bottom*) The $T_{\rm HBR}$ component (y-axis) of the shift presented in the top panel. Note that these are for simulated X-MAS observations of maximum quality, having approximately 120K counts.

3.4.4 Substructure Measures and $T_{\rm HBR}$

Various researchers have established a clear correlation between morphological measures of cluster dynamical state and $\delta \ln M$ [Jeltema et al.(2008)], a correlation which is less apparent in our study of spectral measures of substructure. Similarly, [Cavagnolo et al.(2008)] found a correlation between the temperature ratio and structure for their *Chandra* sample, in that merging events are associated with elevated $T_{\rm HBR}$. To probe this issue further we focus on $T_{\rm HBR}$ and compare it to several metrics for cluster substructure. These are the centroid variation w, the axial ratio η, and the power ratios P_{20} and P_{30} [Ventimiglia et al.(2008)]. The centroid variation w measures the skewness of a cluster's two-dimensional photon distribution by calculating the variance in a series of isophotes for the cluster surface-brightness map. The axial ratio η measures a cluster's elongation, which tends to increase during merger events. The power ratios P_{20} and P_{30} decompose a cluster's surface-brightness image into two-dimensional multi-pole expansions, capturing different aspects of a cluster's geometry. P_{20} relates to the ellipticity in an image and is similar to the axial ratio η, while P_{30} measures the "triangularity" in an image.

In [Ventimiglia et al.(2008)] we calculated these morphological substructure metrics for a superset of the B04 sample of simulated galaxy clusters and compared them to departures from the M-$T_{\rm X}$ relation (see Fig. 2.6 in chapter 2). Here we use the same substructure measures for the 114 B04 clusters for which we are able to calculate $T_{\rm HBR}$ and compare the results. These are presented in Figure 3.12. Whereas in [Ventimiglia et al.(2008)] there is a clear correlation between morphological substructure and $\delta \ln M$, we find in this study that there is little or no correlation between substructure and $T_{\rm HBR}$ for our B04 sample.

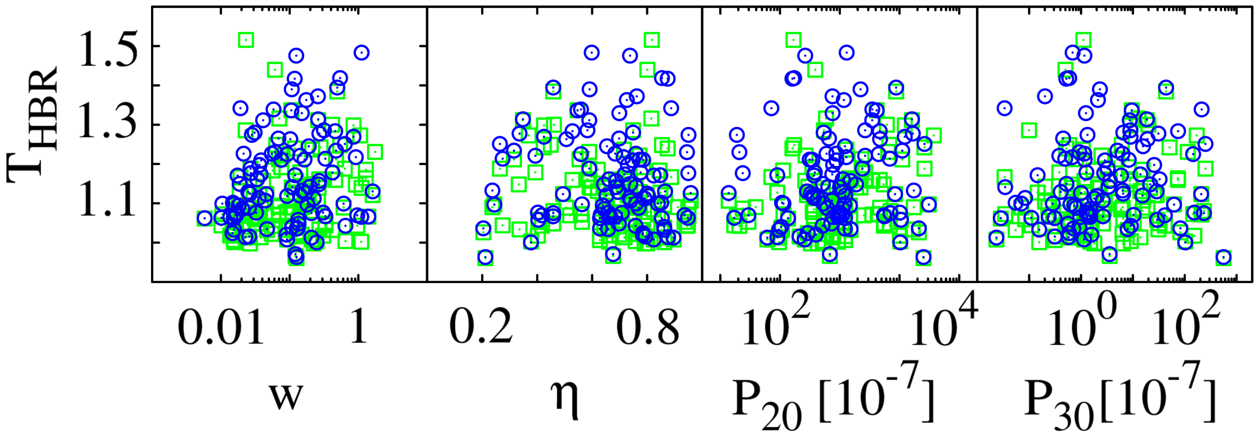

Figure 3.12: Relationship between T_{HBR} and four measures of substructure: the axial ratio η, the centroid variation w, and the power ratios P_{20} and P_{20}. Squares correspond to simulated X-MAS observations that are processed by wavdetect with ellsigma set to 3 (full masking), while circles correspond to observations that have ellsigma set to 0.

In order to understand how temperature structure and morphological structure can be uncorrelated, we looked at four simulated clusters having approximately the same temperature ($k_BT \simeq 3.2keV$) and occupying the relative extremes in $T_{\rm HBR}$ and in the centroid variation w. Two were selected for relatively low $T_{\rm HBR}$ ($\simeq 1.1$) but large variation in w ($\simeq$ 0.02–1.0). Two were selected for large $T_{\rm HBR}$ ($\simeq 1.4$) but again large variation in the morphological structure parameter ω ($\simeq$ 0.1–1.0). These clusters are presented in Figure 3.13 with surface-brightness contours overplotted and with the associated values for $T_{\rm HBR}$ and w. The two clusters in the left column appear more symmetric in their contours, while the two in the right column exhibit noticeable centroid shift. However, the morphologically apparent structure in the lower right cluster is not observed spectrally in the temperature ratio $T_{\rm HBR}$. Evidently, neither morphology nor $T_{\rm HBR}$ is a perfect measure of relaxation in our simulation sample, as it contains clusters with small centroid shift ω and obvious substructure, as in the upper left of this figure. And, it contains clusters with large w that are nearly isothermal, as in the lower right of this figure.

3.5 Summary

We used a sample of galaxy clusters simulated with radiative cooling and supernova feedback, along with simulated *Chandra* X-ray observations of these clusters, to study temperature inhomogeneity as a signature of cluster dynamical state. Specifically, we adopted two methods of quantifying temperature inhomogeneity spectroscopically, the temperature ratio $T_{\rm HBR}$ [Mathiesen & Evrard(2001), Cavagnolo et al.(2008)] and the cool residual RES_{cool}. The former is the ratio of a hardband X-ray spectral-fit temperature to a broadband temperature, and becomes greater than 1 for clusters whose ICM contains cool, over-luminous

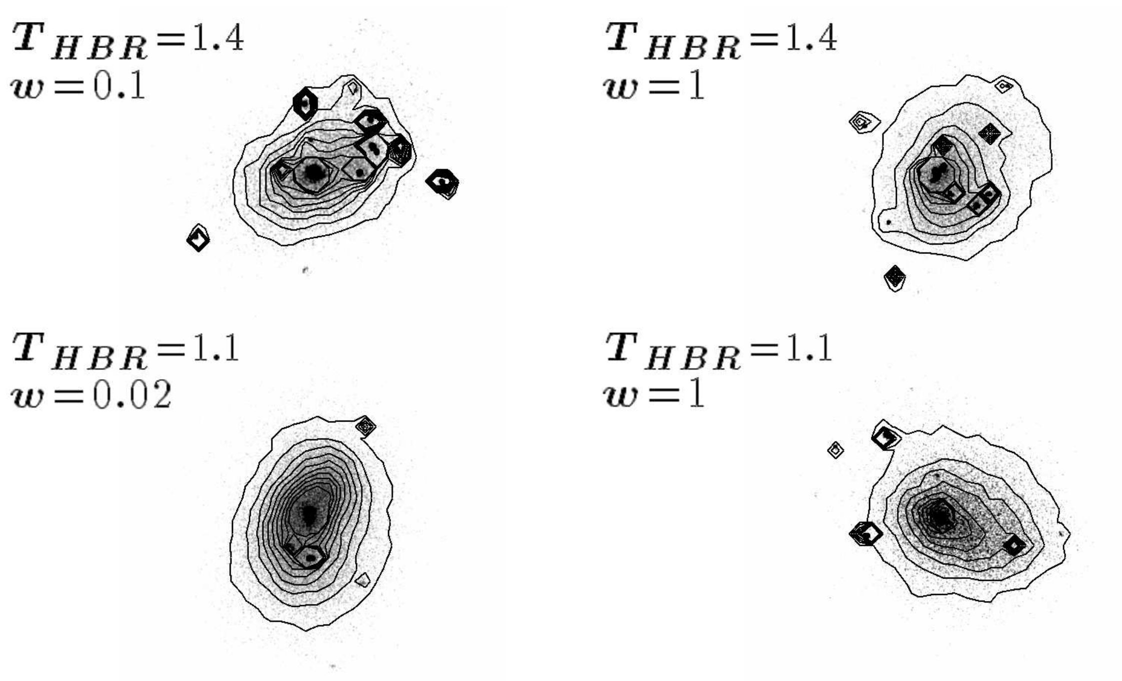

Figure 3.13: Surface-brightness contours for four clusters drawn from our simulation sample, illustrating that temperature ratio and centroid shift are both imperfect measures of relaxation. All four clusters are at nearly the same temperature, with kBT 3.2. The two in the left column exhibit little centroid shift w, while the two in the right column have centroid shift near the maximum for the sample. The two clusters in the bottom row have low THBR while the two in the top row have higher THBR suggesting the presence of multiple temperature components.

sub-components. The latter is the excess broadband count rate relative to the count rate predicted by a model fit to the hard X-ray band. Though our simulated clusters are typically less massive and have lower temperatures than the *Chandra* archive clusters in [Cavagnolo et al.(2008)], we find that their temperature ratios $T_{\rm HBR}$ occupy generally the same distribution as the observed clusters.

We also looked for an opportunity to combine $T_{\rm HBR}$ and the cool residual with the mean mass-temperature relation to obtain better mass estimates than are achieved just with the scaling relation alone. We find, however, that while both $T_{\rm HBR}$ and the RES_{cool} are correlated with offset from the M-$T_{\rm X}$ relation, these correlations are weak, at least for this sample. We conclude that these measures of temperature inhomogeneity are not very effective at reducing scatter in the mass-temperature relation.

Finally, we note a particular difficulty that arises when trying to use clusters from hydrodynamic simulations to calibrate scatter-correction observables based on temperature inhomogeneity, such as $T_{\rm HBR}$. Historically, simulated clusters have tended to exhibit their own kind of "over-cooling problem", in which dense lumps of luminous, cool gas associated with merged sub-halos appear. These cool lumps are often excised from simulated clusters before their global properties are measured, but masking them appears to make the remaining temperature structure of the simulated clusters overly homogeneous. This finding suggests that real clusters may have cooler sub-components, that are more diffuse and less concentrated than in their simulated counterparts. Some physical process, perhaps thermal conduction, turbulent heat transport [Dennis & Chandran(2005), Parrish et al.(2010), Ruszkowski & Oh(2011)], or a more aggressive form of feedback, prevents cool lumps from forming in real clusters and might not completely eliminate those temperature inhomogeneities. Newer simulations incorporate treatments of conduction and AGN feedback, as well as more accurate treatments of mixing, and it will be interesting to revisit these temperature inhomogeneity measures in simulated clusters when large samples of such simulated clusters become available.

counts	ellsigma	$\overline{T^a_{\mathrm{HBR}}}$	$\overline{\sigma}^a$	$\overline{T^b_{\mathrm{HBR}}}$	$\overline{\sigma}^b$
15000	0	1.19	0.15	1.20	0.15
15000	1	1.17	0.13	1.18	0.13
15000	2	1.13	0.12	1.13	0.11
15000	3	1.13	0.13	1.13	0.12
30000	0	1.16	0.12	1.16	0.12
30000	1	1.13	0.11	1.13	0.11
30000	2	1.10	0.10	1.10	0.10
30000	3	1.10	0.10	1.09	0.10
60000	0	1.13	0.10	1.14	0.10
60000	1	1.11	0.08	1.11	0.08
60000	2	1.08	0.06	1.08	0.06
60000	3	1.07	0.06	1.07	0.06
120000	0	1.12	0.11	1.12	0.12
120000	1	1.10	0.09	1.10	0.09
120000	2	1.07	0.07	1.07	0.07
120000	3	1.07	0.07	1.07	0.06

Table 3.1: T_{HBR} & $\sigma_{T_{HBR}}$ with ^{a}All Clusters and ^{b}Clusters with $k_B T_{2.0-7} > 2$ keV

Chapter 4

Modeling Galaxy Cluster Surveys

4.1 Introduction

Given the importance of galaxy clusters in precision cosmology in general and in helping unravel the mystery of Dark Energy in particular, ambitious cluster surveys are planned for the coming decades, such as at the South Pole Telescope [Song et al.(2012)], the Dark Energy Survey [DES(2012)], eROSITA [Merloni et al.(2012)], Pan-STARRS [PanSTARRS(2012)], and the LSST [LSST(2012)]. These surveys will take a census of a substantial fraction of their number in large solid-angle surveys, and will make detailed studies of important characteristics in more narrow, targeted surveys. Naturally, numerical and semi-analytical models will be essential to such programs. While numerical simulations are powerful, general, and sometimes resolve details with amazing precision, it is worthwhile to complement them with semi-analytical models, which have their own virtues. Computationally efficient, they sometimes can be crafted to yield deep insights. Semi-analytical galaxy cluster survey models also are often built around just a few simple, key principles. One common approach is to join a cosmological model to a structure formation model, subject to observational constraints. In this work we take advantage of these common characteristics by abstracting them into a simple program and library, called CosmoSurvey, which is efficient to evaluate on commodity computing hardware and is adaptable to a variety of applications. It is a simple, convenient, extensible, flexible, efficient model of flux-limited galaxy cluster surveys.

4.2 CosmoSurvey

CosmoSurvey is a semi-analytical modeling framework for galaxy cluster surveys, which relies on the Press-Schechter formalism [Press & Schechter(1974)] augmented with halo mass functions derived from numerical simulations. It is both a program in that it can be used out-of-the-box to model flux-limited galaxy cluster redshift surveys simply from the command-line, and also a framework in that it provides library functions for modeling other kinds of cluster surveys. Its overall design is described in the next section, while a user guide and reference manual appears in an appendix.

4.2.1 Design

CosmoSurvey ultimately is a very simple program and set of tools. Its utility derives from a coherent, deliberate set of goals, principles, and architectural choices.

4.2.1.1 Goals

Broadly speaking the goal of this project is to create a general-purpose framework for modeling galaxy cluster surveys according to a small set of guiding principles.

4.2.1.2 Principles

These guiding principles for CosmoSurvey are the following.

- It should be easy to understand.
- It should be easy to use.
- It should be easy to adapt.

- It should be easy on the hardware.

4.2.1.3 Architecture

Probably the first thing the user notices about CosmoSurvey as soon as they inevitably wish to extend or adapt it, is that it is written in Fortran. This may seem an unusual choice at first. While Fortran has a strong pedigree in science and engineering, it is undeniable that this oldest general-purpose programming language still in use grows more out-of-fashion as it enters its seventh decade.

Nevertheless, Fortran still has considerable life within it. It is still widely-used and widely-understood in the scientific and engineering communities. There are abundant high-quality libraries available in Fortran. Fortran excels in numerical computation. Fortran is exceptionally fast and efficient. Newer versions of Fortran, like Fortran 95 and Fortran 2003 add modern programming features. There are excellent free and commercial compilers for Fortran. And, newer versions of Fortran perform powerful optimizations, like auto-vectorizing array operations on multi-core hardware. CosmoSurvey is written in Fortran 95 in order to take advantage of these features, including the new module system, dynamic memory allocation, and array auto-vectorization.

Modeling a galaxy cluster census as it does, CosmoSurvey naturally makes abundant use of one-dimensional and multi-dimensional numerical integration. These services are provided by robust, well-optimized, and sometimes ancient third-party libraries written in either Fortran or C. One-dimensional integration is performed using the excellent Netlib libraries, which are written in Fortran 77 and in some cases Fortran 66. Multi-dimensional integration is performed using the CUBA library, which is written in modern C but is equipped with a Fortran interface.

In addition to its core function of providing quantitative estimates of galaxy cluster survey results, CosmoSurvey also provides additional plotting tools. These functions are supplied by the PLplot library. Like CUBA, it also is written in C but possesses a convenient Fortran interface.

Tailored to the writing of small command-line programs as it is, CosmoSurvey has a flexible, easy-to-use system for creating command-line interfaces. This is no small task, given that user interactivity, I/O, and text processing are among Fortran's weakest areas. Command-line interface functions are performed using the Kracken library.

CosmoSurvey has just a few core modules that can be combined and adapted to create different kinds of cluster survey models. Out of the box, they supply the `cosmosurvey`, `cosmoplot`, and `cosmotest` programs. Of these, the `cosmosurvey` program is the main program of interest. Its basic operation is to evaluate its internal model according to command-line arguments and emit observables to standard output. One nice aspect of this design is that the use of command-line arguments and standard output make it easily scriptable.

The other programs provided out of the box are `cosmoplot` and `cosmotest`. The `cosmoplot` program is an auxiliary tool that helps the user visualize the internal survey model. The `cosmotest` program is another tool that helps the user visualize specific components of the internal model.

4.2.1.4 Modules

As introduced above, CosmoSurvey has just a few modules. The core modules are `constants` (which, in general, defines physical units), `cosmology`, and `structure`. Additional important modules are the `survey` modules, which are easy to write. These modules, their details, and the ways they relate are described in greater detail in the following paragraphs, and in the appendix.

The `cosmology` module defines a user-defined type named `cosmoparams`, that collects in one place all of the physical parameters of the joint cosmology-cluster-survey model. The `cosmology` module defines a global variable of type `cosmoparams` and named `theta_G`. This makes the model parameters in `theta_G` available to all functions that use the `cosmology` module, which in general are all other modules and programs in the CosmoSurvey suite. This choice was made for several reasons. First, it is convenient to have these model parameters available globally, to avoid the cumbersome ritual of passing so many values into all of the other functions that use them, of which there are many. Second, it turns out it is necessary to have these model parameters available globally, since the Netlib and CUBA numerical integration libraries prohibit the ability to communicate parameters into their integrands directly. Third, Fortran 95 custom or user-defined types are a convenient way to aggregate related data. The `cosmology` module also provides convenience functions for returning instances of `cosmoparams`, the model parameter priors, and String names for these model parameters. Finally and most important, the `cosmology` module provides functions for computing global geometry, expansion history, comoving distances, comoving volumes, matter and Dark Energy density parameters, and various commonly-used distance measures.

The `structure` module provides functions for computing the growth of linear perturbations, halo concentration, the M-T and L-M mass-observable relations for galaxy clusters, for describing intrinsic scatter in these relations, and for calculating the luminosity and flux of distant sources.

The `survey` module ties together the `constants`, `cosmology`, and `structure` modules. It mainly provides functions for convolving the halo concentration, the comoving volume, the mass-observable scatter, and the survey flux limit, to calculate integrated galaxy cluster number counts in redshift-luminosity observable bins.

Finally, the `cosmosurvey` program brings these modules together, provides a run-time context for the `survey` and its dependent modules, arranges for the specification and collection of command-line arguments, and generates the program output.

4.2.1.5 Trade-offs

It is important to acknowledge several trade-offs that were accepted in the design and writing of CosmoSurvey. First, as a compiled language, Fortran is not as convenient or as flexible as dynamic programming environments, like IDL or Python. This was accepted for the sake of computational efficiency and for the convenience of running outside of a run-time, which introduces other forms of complexity. Second, as noted above Fortran is out of fashion. Fortran 95 and Fortran 2003 often are ignored, and Fortran in general is not as modern a language, like even C is by comparison. This was accepted because of the many modern programming features Fortran 95 provides, because of the reported numerical efficiency edge over C, and because though older, Fortran actually is easier to read and easier to program in than C/C++ is, so long as one avoids low-level system access, string and character manipulation, and object-oriented programming. Third, CosmoSurvey uses PLplot. As a library compiled into one's executables, PLplot is not as flexible as data-oriented plotting tools, like GNUplot or Excel, and is not as convenient as exploratory dynamic programming environments, like IDL or R. This was accepted because those tools still can be used with `cosmosurvey` output, and it is often convenient to build plotting and visualization functions directly into your executables. In addition, PLplot is powerful, produces high-quality output in a dizzying array of formats, is well-documented, and is free. Fifth, while it may be possible to build CosmoSurvey in a Windows environment, the package and especially its build system is not designed for and has never been tested in this setting. This was accepted because high-quality Unix-like programming, development, and analysis environments are now widely available, and are nearly ubiquitous in astrophysics. Finally and probably most important the cosmological, galaxy cluster, and survey models are without a doubt quite simple. This was a deliberate choice, and was accepted because it is relatively simple to adapt and augment them with additional model components, though it does require programming to do so. These simple component models are described in detail in the next section.

4.2.1.6 Cosmological Model

We begin by describing in broad outline the cosmological model of the Universe in CosmoSurvey. For this we choose the concordance model for its simplicity, for its accessibility to semi-analytical computational methods on commodity hardware, and for its success in explaining the observed properties of the Universe. Also called the ΛCDM model—emphasizing the importance of Dark Energy and Cold Dark Matter—it rests on a small set of assumptions [Longair(2008), Voit(2005)]

- The Universe is homogeneous and isotropic on large scales.
- It comprises an expanding, pressureless, curl-free fluid that obeys *Weyl's Postulate*, so that the fluid particles move along world lines that only meet at a common point in the past.
- Its geometry and dynamics are governed by its contents and obey the principles of General Relativity.
- It contains radiation, baryonic matter, Cold Dark Matter, and Dark Energy.

- At an early epoch its matter component received an imprint of Gaussian-random "primordial" density fluctuations that had a scale-free Fourier-space power spectrum.

A Lagrangian spherical coordinate system in which the radial component r moves along with a fluid free of gradients and vorticity is the natural choice for an expanding, homogeneous Universe. This so-called comoving coordinate system has the virtue of separating out of proper distances ρ a non-local, time-dependent scale factor $a(t)$

$$a(t) = \frac{\rho(t)}{r} \tag{4.1}$$

that is taken to be unity at the current epoch. The scale factor can be put on an empirical basis using Hubble's Law

$$\dot{\rho} = H\rho \tag{4.2}$$

which describes the proportionality of proper distances to expansion velocity $\dot{\rho} = \dot{a}\,r$ and defines the Hubble parameter H.

$$H = \frac{\dot{a}}{a} \tag{4.3}$$

The value H_0 of the Hubble parameter at the current epoch is an important cosmological parameter, sought by nearly a century of astronomers. It is currently estimated to be 72 km/s/Mpc.

Because the Universe is homogeneous it also possesses a non-local curvature κ and a corresponding global radius of curvature $\mathcal{R} \propto \kappa^2$. A compact way to summarize these geometric and kinematic properties is by way of the Robertson-Walker metric ds

$$ds^2 = c^2\,dt^2 - a^2(t)\left[\frac{dx^2}{1 - \kappa\,x^2/\mathcal{R}^2} + x^2\,d\phi^2\right] \tag{4.4}$$

where $d\phi$ is a transverse angle and where we make the transformation

$$x = \{\ R\sin(r/\mathcal{R}), \kappa > 0, \mathcal{R}\sinh(r/\mathcal{R}), \kappa < 0. \tag{4.5}$$

The Robertson-Walker metric is the starting point for developing useful relations between time intervals, proper distances, and coordinate distances in this coordinate system. For instance, as a light signal propagates it accumulates coordinate distance dr

$$dr(t) = \frac{c\,dt}{a(t)} \tag{4.6}$$

whose integral from an observer at the origin O to an event at an earlier epoch t defines the distance measure D

$$D = \int_{t_O}^{t} dr(t') \tag{4.7}$$

In addition to these effects, light rays also are deflected by spatial curvature, and this deflection distorts observed angles. The angle subtended by a coordinate distance dr at coordinate distance r becomes

$$d\phi = \frac{dr}{x} \tag{4.8}$$

where x is defined in equation 4.5. Equation 4.8 defines the angular-diameter distance measure

$$D_A = a\,x \tag{4.9}$$

Equation 4.8 allows us to specify a comoving volume element $dV(t)$ at distance $\rho(t)$ in solid angle $d\Omega$ and comoving coordinate interval dr.

$$\begin{aligned} dV(t) &= x\, d\theta\, x\, d\phi\, dr \\ &= x^2\, d\Omega\, \frac{c\, dt}{a(t)} \end{aligned} \tag{4.10}$$

The time coordinate t in equations 4.6 and 4.10 can be replaced with the observable redshift z, which measures the stretch a photon wavetrain experiences in an expanding Universe. Expressed as a ratio of observed to emitted wavelengths, this stretch is merely the ratio of the scale factor between the observed and emitted times.

$$\frac{\lambda_o}{\lambda_e} = \frac{a(t_o)}{a(t_e)} \tag{4.11}$$

Since observations are always made at the current epoch when $a(t_o) = 1$, the scale factor at the emitted time can be relabeled simply a, so that $a = \lambda_e/\lambda_o$. The observed redshift is the fractional difference between a photon's emitted wavelength λ_e and its observed wavelength λ_o.

$$z = \frac{\lambda_o - \lambda_e}{\lambda_e} \tag{4.12}$$

Therefore, redshift z measures scale factor a by way of the important relation

$$a = \frac{1}{1+z} \tag{4.13}$$

with intervals of z and a related by

$$da = -\frac{1}{(1+z)^2}dz = -a^2 dz \tag{4.14}$$

Connecting the time interval dt to the Hubble parameter H and scale factor a through equation 4.3,

$$dt = \frac{da}{aH} \tag{4.15}$$

using equation 4.14, and remembering that x is itself a function of r and t, equations 4.6 and 4.10 become

$$dr(z) = \frac{c}{H(z)}\, dz \tag{4.16}$$

$$dV(z) = x^2\, d\Omega\, \frac{c}{H(z)}\, dz \tag{4.17}$$

The geometry of a homogeneous and isotropic universe, characterized by its curvature κ and corresponding radius of curvature $\mathcal{R}$, is a function of its mass-energy content and is governed by General Relativity. This is described with the Friedmann-Lemaitre model, which uses the dynamical equation

$$\frac{\ddot{a}}{a} = -\frac{4}{3}\pi G\rho \tag{4.18}$$

where ρ is the mean energy density owing to matter, energy, and pressure. Note that in this context the symbol ρ as a density should not be confused with the same symbol used to signify proper distances, as in the discussion leading to equation 4.17.

Of course, the density ρ is itself a function of the scale factor a, which can be factored out along with a scale-independent density ρ_0, so that $\rho = \rho_0\, f(a)$. Multiplying equation

4.18 by a and using this substitution we obtain

$$\ddot{a} = -\frac{4\pi G\rho_0}{a^2}. \tag{4.19}$$

Equation 4.19 can be integrated once using energy conservation

$$\dot{\rho} = -3\frac{\dot{a}}{a}\Big(\rho + p\Big), \tag{4.20}$$

so long as we have an equation of state to relate the pressure p to the density ρ. If the pressure is proportional to the density with $p = w\,\rho$, then we obtain

$$\dot{a}^2 = \frac{8}{3}\pi G\rho_0 a^{-(1+3w)} + const. \tag{4.21}$$

The constant of integration in equation 4.21 relates to the global curvature of the Universe. Notwithstanding the radiation-dominated era at high redshift, and before Dark Energy dominates, the Universe is well-represented by a pressureless dust model with $w = 0$. If we imagine a flat Universe with zero curvature everywhere, from equation 4.21 we can define a critical density ρ_c which would bring it about,

$$\rho_c = \frac{3H_0^2}{8\pi G}. \tag{4.22}$$

This is a useful unit for measuring density and when factored out allows us to define a dimensionless density parameter Ω_0,

$$\Omega_0 = \frac{\rho_0}{\rho_c}. \tag{4.23}$$

In fact, we can define a family of density parameters for any given component x with density ρ_x—such as radiation or Dark Energy—in a similar way, so that

$$\Omega_x = \frac{\rho_x}{\rho_c}. \tag{4.24}$$

Equation 4.21 then becomes for a flat Universe, when incorporating the equation of state parameter w, the Hubble constant H_0, the density parameter Ω_0, and switching from scale factor a to its observable analog the redshift z

$$H^2(z) = \left(\frac{\dot{a}}{a}\right)^2 = H_0^2 E^2(z) = H_0^2 \left[\Omega_M (1+z)^3 + \Omega_\Lambda\right]. \tag{4.25}$$

This is another important relation, and $E(z)$ is one of the critical computations in a semi-analytical cosmology model.

4.2.1.7 Cluster Model

We assumed that the cosmological model of an expanding Universe is homogeneous and isotropic on large scales, because observations lead us to that conclusion. But observations closer to home also tell us that the Universe is decidedly not homogeneous on smaller scales, and this fact is captured by another of our assumptions. In the concordance model, we posit that the Universe at an early time received an imprint of density fluctuations in its Dark Matter component, and adopt a model in which these "primordial fluctuations" grow in contrast to the uniform background density under the influence of their own self-gravity, eventually collapsing into gravitationally-bound structures.

The natural framework for that discussion and the subject of structure formation begins with the density contrast

$$\delta(\mathbf{x}) = \frac{\rho(\mathbf{x}) - \langle\rho\rangle}{\langle\rho\rangle}. \tag{4.26}$$

We can relate the density contrast field $\rho(\mathbf{x})$ to an analogous mass perturbation field $\delta M/M(\mathbf{x})$ if we adopt some appropriate smoothing kernel $W_R(r)$ with a characteristic length scale R.

$$\left.\frac{\delta M}{M}\right|_R(\mathbf{x}) = \int \delta(\mathbf{x}) W_R(|\mathbf{x}-\mathbf{r}|) d^3r \tag{4.27}$$

Of course, we are not interested in the density contrast or mass perturbation fields at any particular location $\mathbf{x}$, but rather in their statistical properties. A useful starting point that paves the way to observable comparisons is to begin with the field's Fourier components

$$\delta_{\mathbf{k}}(k) = \int \delta(\mathbf{x}) e^{i\mathbf{k}\cdot\mathbf{x}} \tag{4.28}$$

and their isotropic power spectrum

$$P(k) = \langle|\delta_k|^2\rangle. \tag{4.29}$$

Building up our statistical picture, we can imagine sampling the perturbation field to obtain its variance on the length scale of the smoothing kernel W_R, using its Fourier transform W_k

$$\left.\sigma^2\right|_R = \frac{1}{(2\pi)^3} \int P(k)|W_k|^2 d^3k. \tag{4.30}$$

In all these relations, it is useful to consider the mass that would be contained within the smoothing kernel given the mean background density. In that case, equations like 4.30 pertain not just to a given length scale but also to a corresponding mass scale.

In our post-radiation era matter-dominated dust model, the amplitude of matter density fluctuations grows linearly with the scale factor a until they reach a density contrast $\delta\rho/\rho \approx 1$ at which point the growth rapidly becomes non-linear. The fluctuations become gravitationally bound collapsed structures that have "detached" from the global expansion of the Universe. In our model they are associated with the Dark Matter halos that trapped ordinary baryonic matter and are the sites of galaxy and cluster formation. In any case, the full treatment of the growth of perturbations through the radiation-dominated era and considering Dark Energy is a complex topic which will not be explored in detail here. Fortunately, numerically-integrated growth functions $G(z) \propto \delta\rho/\rho$ exist. While it is easy in CosmoSurvey to use different growth functions, we adopt that of Linder [Linder(2005)] because it opens the door to modeling the effects that departures from General Relativity might have on structure growth

$$G(z) = \frac{1}{1+z} \exp \int_z^\infty \frac{\Omega_M(z)^\gamma - 1}{1+z}. \tag{4.31}$$

which appears in figure 4.1 The level of departure from General Relativity is controlled by the γ parameter, with a value of 0.55 corresponding to no departure.

As the density fluctuations grow in contrast and approach $\delta\rho/\rho \approx 1$, the growth of their corresponding mass fluctuations becomes non-linear and we assume they collapse into bound Dark Matter halos. We need a prescription for modeling this, and an elegantly simple one can be found in the Press-Schechter formalism. Assuming the initial perturbation field to have a Gaussian sample variance σ, then the probability that any particular fluctuation has a contrast above some threshold δ_c is simply the error function $erfc[\delta_c/\sqrt{2}\sigma]$. Keep in mind that the variance σ will itself be be a function of the scale of the perturbation, according

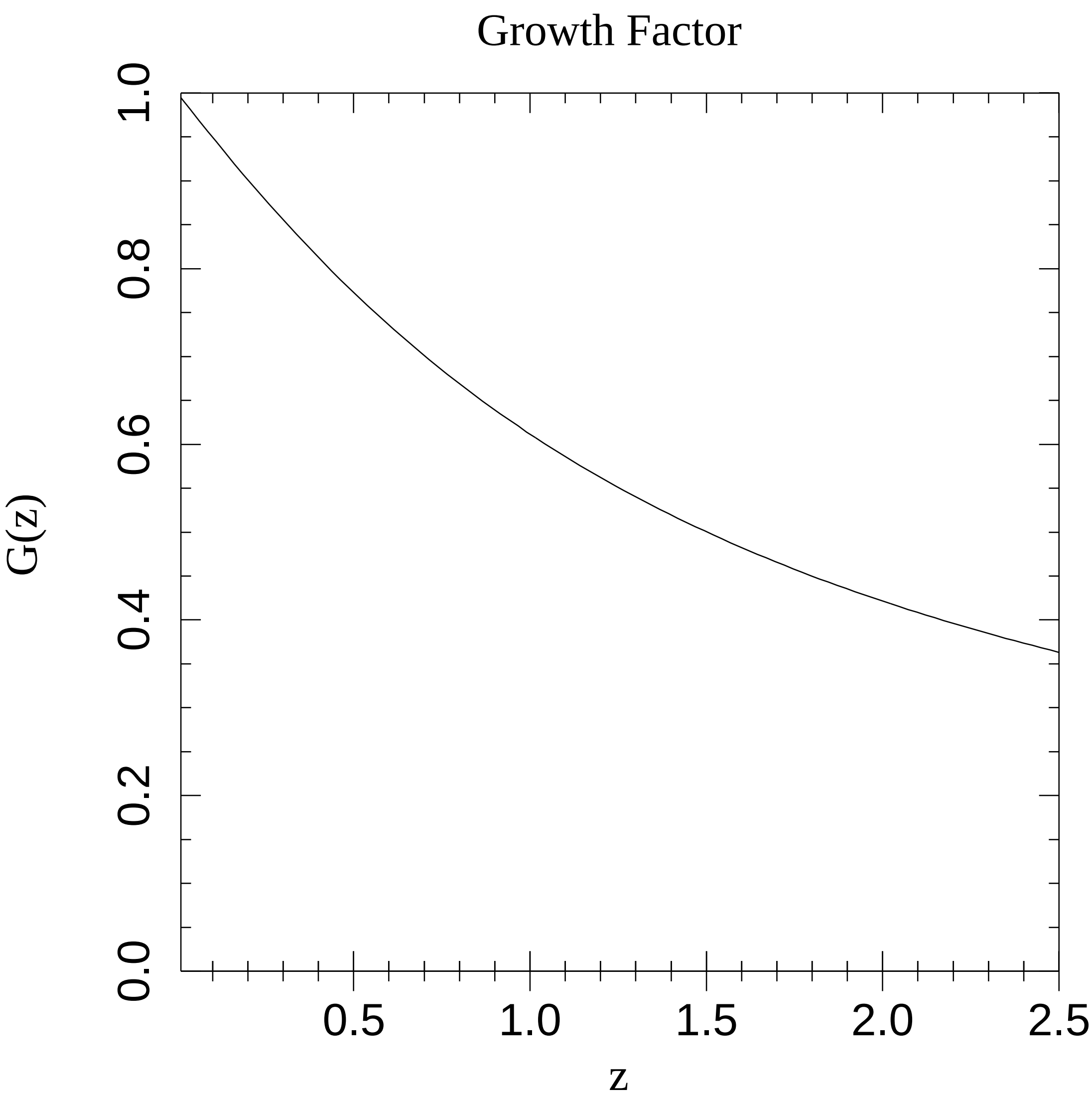

Figure 4.1: Growth factor $G(z)$ for the growth of density fluctuations.

to the power spectrum of initial perturbations. By "scale", that is the length-scale of the perturbation, the related wavenumber, or more usefully, the enclosed mass M. It will also be a function of the redshift z via the growth factor $G(z)$, with $\sigma(M,z) \propto G(z)$. Then with the number density of mass perturbations of mass M simply $\Omega_M \rho_c / M$, the density of collapsed halos will be

$$n(M,z) = \frac{\Omega_M \rho_c}{M} erfc\left[\frac{\sigma_c}{\sqrt{2}\sigma(M,z)}\right] \tag{4.32}$$

and the differential mass-function is then

$$\frac{dn}{d\ln\sigma} = -\sqrt{\frac{2}{\pi}} \frac{\Omega_M \rho_c}{M} \frac{\delta_c}{\sigma} \exp\left[-\frac{\delta_c^2}{2\sigma^2}\right]. \tag{4.33}$$

The Press-Schechter approach is an invaluable way to frame the issue of modeling the collapse of Dark Matter halos, but these days more accurate results are obtained via numerical simulations. CosmoSurvey adopts a mass function produced from simulations in just such a way [Jenkins et al.(2001)].

$$\frac{dn}{d\ln\sigma} = -A_J \frac{\Omega_M \rho_c}{M} \exp\left(-|B_J - \ln\sigma|^{\epsilon_J}\right) \tag{4.34}$$

where A_J, B_J, ϵ_J are parameters fit from numerical simulations with $A_J = 0.301$, $B_J = 0.64$, and $\epsilon_J = 3.82$.

Again, in these relations σ is the variance in density fluctuations on a given length scale, which can be mapped to a given mass. Simple application of the chain rule translates equations 4.33 and 4.34 into true mass functions. The number density of clusters of mass M is then

$$\frac{dn}{d\ln M} = \frac{\Omega_M(z)\rho_c}{M} A_J \exp\left(-|B_J - \ln\sigma|\right) \tag{4.35}$$

Mass functions like this appear in figure 4.2, where the exponential cutoff for the largest mass galaxy clusters is apparent.

The cosmological and cluster model provide the basic framework for the CosmoSurvey model. The final remaining ingredient for translating that into a model that could, in principle, be compared to observations, is a treatment of the survey itself. This necessarily also requires delving into the the observable properties of galaxy clusters, and how they relate to the only property we have considered so far, which is their mass.

4.2.1.8 Survey Model

As introduced above, the survey model necessarily must consider the observable properties of galaxy clusters. Two observables that are featured prominently in the CosmoSurvey model are the cluster luminosity in a broad X-ray band and the temperature of the hot, tenuous gas that emits the X-rays.

For it turns out that in certain respects galaxy clusters are only incidentally about galaxies. To start, the bulk of a cluster's mass is in its collapsed Dark Matter halo whose gravity binds the cluster together. In addition, the remaining baryonic matter comprises mostly a dilute, hot, ionized hydrogen gas that copiously emits X-rays in the 1-10 keV energy range via the thermal bremsstrahlung process. The X-ray luminosity in some well-defined suitably chosen range then offers one important observable. What is more, we can adopt a thermal model for the X-ray emitting intra-cluster medium (ICM) and infer temperatures for the components of that model. Chapter 3 of this work uses simulated galaxy clusters to examine models with multiple thermal components, but a common and useful starting point is simply to assume the entire ICM is in thermal equilibrium at one temperature. That is the approach CosmoSurvey uses, so that we can talk about "the temperature" as another observable in

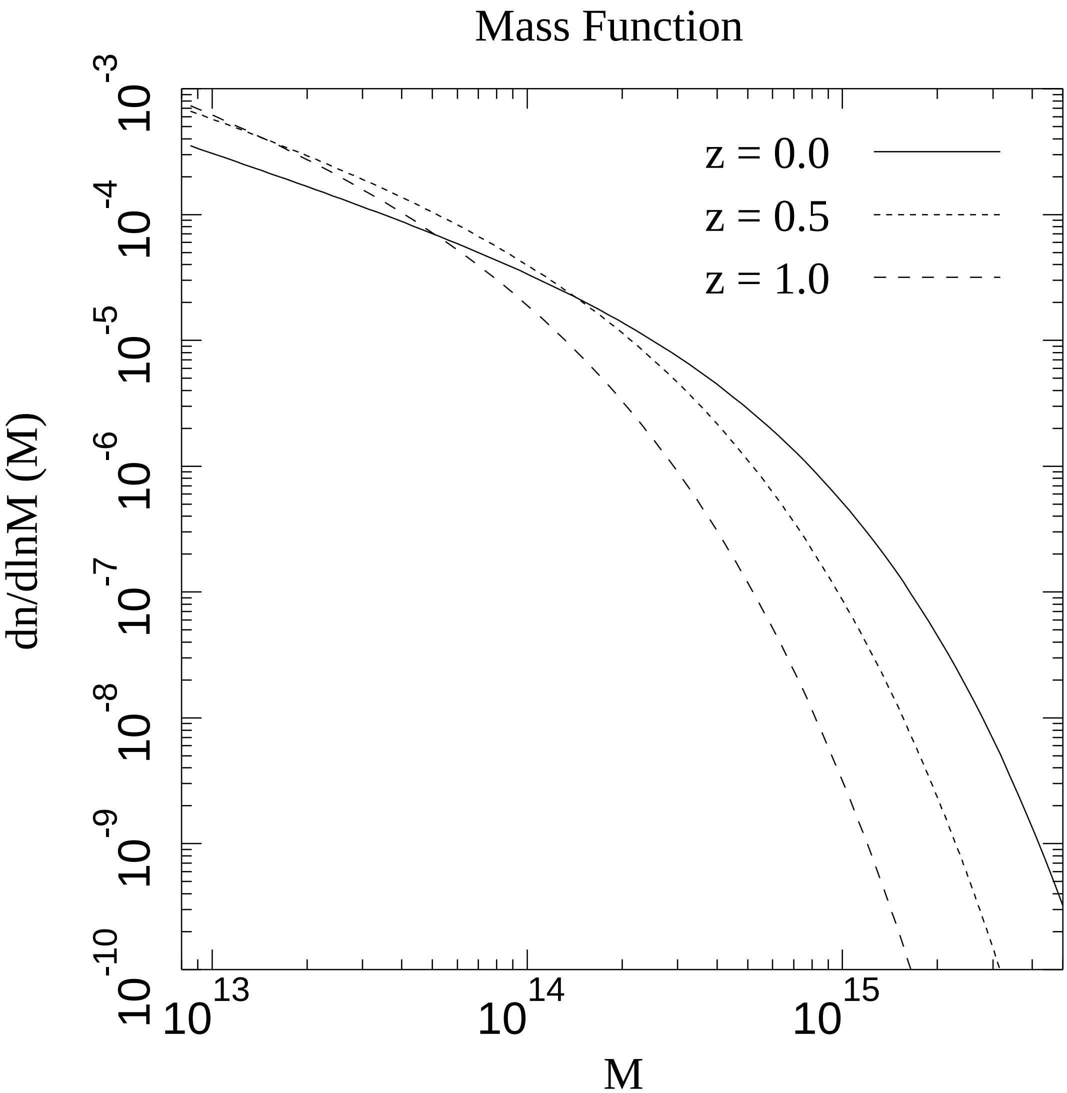

Figure 4.2: Differential mass function for the number density of collapsed Dark Matter halos, at three different redshifts

addition to luminosity.

Next, we need to link the X-ray luminosity and temperature to the theoretical model we have built up so far, which as equations 4.32, 4.33, and 4.34 show has only considered a cluster's mass. The simplest non-trivial way we could relate mass M, X-ray luminosity L, and X-ray temperature T is in power-law form, and this turns out to be a good choice on both theoretical and observational grounds. Structure in general arises from initial density perturbations whose spectrum is assumed to be scale-free, and its growth is driven by gravitational processes that have no way to impart scale. If we assume that the processes that heat the ICM also to be scale free (significant line emission, non-linear thermal and dynamical instabilities, and cluster energy feedback will violate this assumption), then a scale-free power law is the only choice for relating galaxy cluster mass, X-ray luminosity, and X-ray temperature.

$$\frac{L}{L_0} = \left(\frac{M}{M_0}\right)^{\beta} \tag{4.36}$$

$$\frac{T}{T_0} = \left(\frac{M}{M_0}\right)^{\alpha} \tag{4.37}$$

Where L_0, T_0, and M_0 are some fiducial values for luminosity, temperature, and mass, and β and α are the power-law slopes for these relationships. Together, they comprise additional parameters for our model, made more vivid when equations 4.36 and 4.37 are cast in a more convenient logarithmic form. Defining $\lambda = \ln L$, $\tau = \ln T$, and $\mu = \ln M$, then equation 4.36 becomes

$$\lambda = \beta\mu + \ln L_0 - \beta \ln M_0. \tag{4.38}$$

Similarly, equation 4.37 becomes

$$\tau = \alpha\mu + \ln T_0 - \alpha \ln M_0. \tag{4.39}$$

This formulation for the luminosity-mass (L-M) and temperature-mass (T-M) relationships makes it easy to ratchet up by one notch the complexity and richness of what is otherwise still a very simple model. In particular, we can consider the phenomenon of scatter in these mass-observable relationships. Scaling arguments aside, we expect clusters not to adhere rigidly to the mass-observable relationships, and this expectation is supported by observations. There is scatter in the L-M and T-M relationships. Scale-imposing processes in the ICM, in galaxy cluster feedback, and in galaxy formation break the symmetry of self-similarity. X-ray luminous active galactic nuclei (AGN) may "contaminate" X-ray surveys for galaxy clusters and introduce confusion. Further complicating matters, scatter itself may evolve with redshift z. Still, given a model for scatter with new parameters, and enough of the right kind of data, perhaps we could fit for the scatter parameters. Whether that is practical or even possible for a given scatter model is the question CosmoSurvey originally was intended to help answer. CosmoSurvey adopts a simple model of log-normal scatter in the L-M and T-M relationships, constant in mass but evolving with redshift z. Defining σ_λ and σ_τ to be the standard deviations in log luminosity λ and log temperature τ, we adopt a simple power-law redshift evolution, with

$$\sigma_\lambda = \sigma_{\lambda 0}\,(1+z)^{\phi}, \tag{4.40}$$

$$\sigma_\tau = \sigma_{\tau 0}\,(1+z)^{\psi}. \tag{4.41}$$

The CosmoSurvey cluster model also treats covariance in luminosity and temperature scatter, with a covariance parameter ρ, and a covariance matrix $\mathbf{C}$

$$\mathbf{C} = \begin{pmatrix} \sigma_\lambda \sigma_\lambda & \rho \sigma_\lambda \sigma_\mathcal{T} \\ \rho \sigma_\mathcal{T} \sigma_\lambda & \sigma_\mathcal{T} \sigma_\mathcal{T} \end{pmatrix} \tag{4.42}$$

With this Gaussian scatter the likelihood that a cluster of log mass μ will have log luminosity λ and log temperature τ is straightforward. Its joint probability density function is merely the multivariate normal distribution. With two random variables λ and τ whose expectation values λ_0 and τ_0 at fixed μ are given by the L-M and T-M relationships we can define the vector $\mathbf{X}$ as

$$\mathbf{X} = \begin{pmatrix} \lambda - \lambda_0 \\ \tau - \tau_0 \end{pmatrix}. \tag{4.43}$$

The joint conditional probability $P(\lambda, \tau|\mu)$ that a cluster of log mass μ will have log luminosity λ and log temperature τ is

$$P(\lambda, \tau|\mu) = \frac{1}{2\pi\,|\mathbf{C}|} \exp\left(-\frac{1}{2}\mathbf{X}^T\mathbf{C}^{-1}\mathbf{X}\right) \tag{4.44}$$

where $|\mathbf{C}|$ is the determinant of the scatter covariance matrix $\mathbf{C}$ and $\mathbf{C}^{-1}$ is its inverse.

While CosmoSurvey easily could be adapted to support other survey types, out-of-the box it models flux-limited observations of galaxy cluster number counts in luminosity and redshift space. The product of equations 4.35 and 4.44 can be integrated over a log luminosity interval $\Delta\lambda = [\lambda_1, \lambda_2]$, a redshift interval $\Delta z = [z1, z2]$, and over all log mass μ and log temperature τ, multiplied by a solid angle $\Delta\Omega$, and restricted by a suitable flux limit calculation. The integrand is

$$\frac{dN}{d\mu\, d\tau\, d\lambda\, dz\, d\Omega} = \frac{dn}{d\ln M} P(\lambda, \tau|\mu) \tag{4.45}$$

The result is the expected number of observable clusters in that luminosity-redshift bin, N_i

$$N_i = \int_{z=z_1}^{z=z_2} \int_{\lambda=\lambda_1}^{\lambda=\lambda_2} \int_{\tau=-\infty}^{\tau=\infty} \int_{z=-\infty}^{z=\infty} \frac{dN}{d\mu\, d\tau\, d\lambda\, dz\, d\Omega} d\mu' d\tau' d\lambda' dz' \Delta\Omega. \tag{4.46}$$

CosmoSurvey adopts a hard flux limit by applying a redshift-dependent cutoff to the integration in log luminosity λ, given a flux f

$$\lambda_c = \ln\left(\frac{4\pi D_L^2 f}{L_0}\right) \tag{4.47}$$

where D_L is the luminosity distance measure D_L. This flux limit calculation is depicted in figure 4.3

With these labors and using an adaptive multi-dimensional integration package, CosmoSurvey obtains a matrix of observables $\mathbf{N}$ comprising counts N_{ij}. These are the expected galaxy cluster number counts in log luminosity and redshift bins. Partly as a computational convenience, but also to emphasize their role as independent observables, CosmoSurvey unrolls the matrix into a vector of observables $\theta = (\theta_1, \theta_2, \ldots, \theta_i, \ldots)$ when generating its final output. The matrix of observed number counts is plotted in figure 4.4.

4.3 Summary

CosmoSurvey is a program and a framework for quickly and easily modeling flux-limited galaxy cluster surveys on commodity hardware. Written in modern Fortran 95, it is fast,

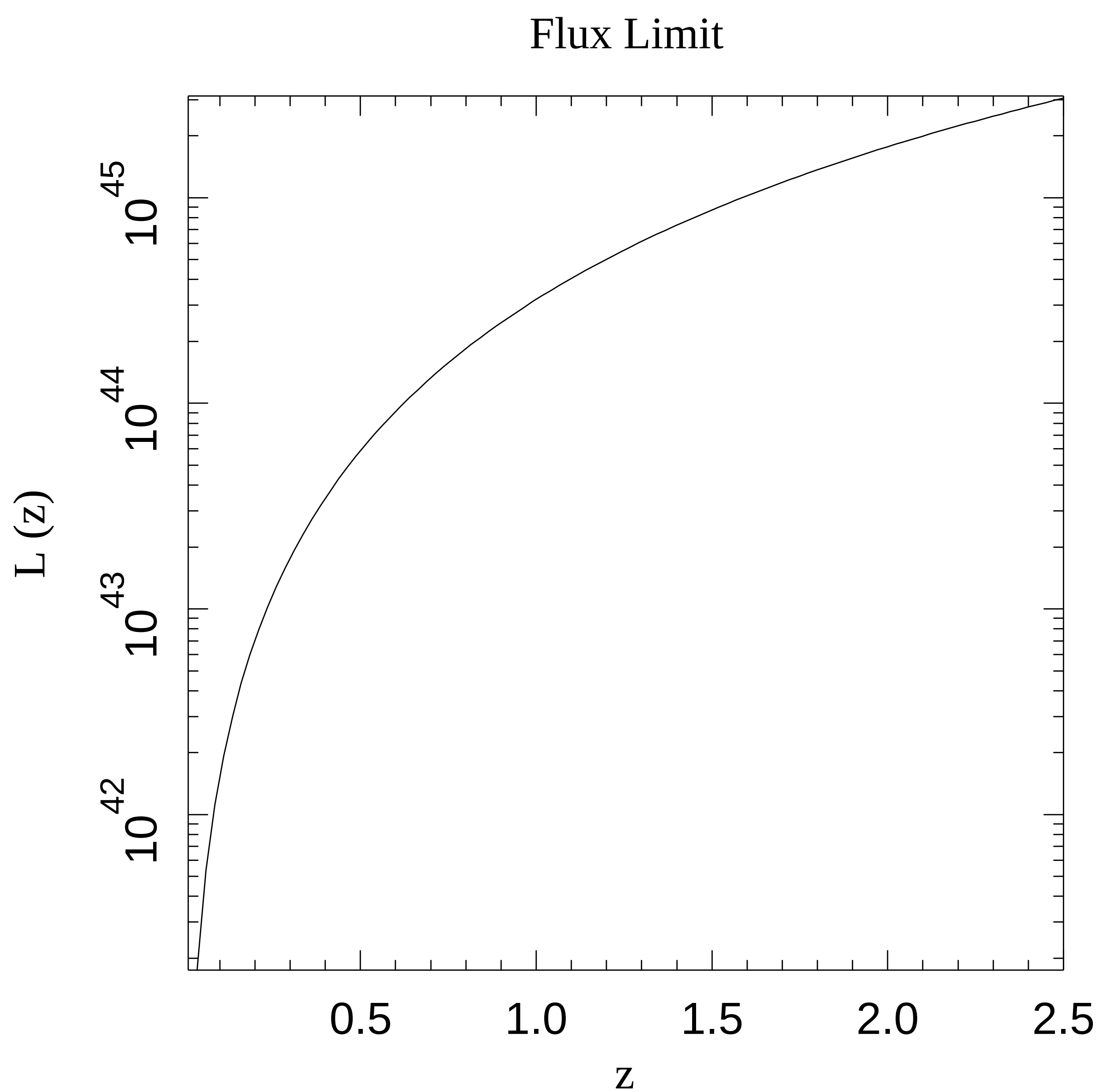

Figure 4.3: Flux limit calculation used to cut off the integration of galaxy cluster number counts over a luminosity bin.

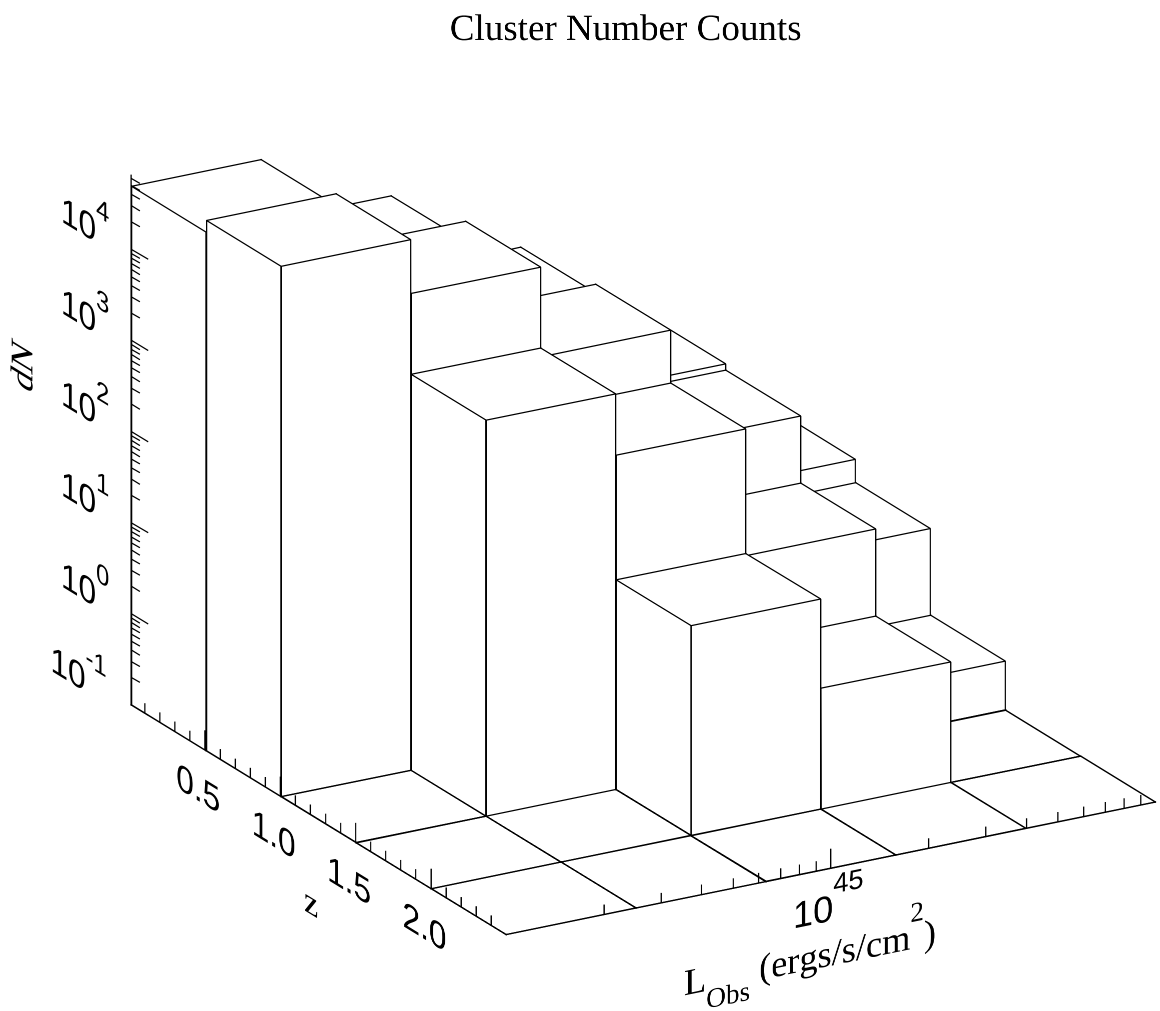

Figure 4.4: CosmoSurvey simulated cluster survey counts in observable bins, obtained using the cosmoplot program.

efficient, and easily adapted. It and programs written with its library run on the command-line, using a simple interface. It also emits estimated number counts of observed galaxy clusters in luminosity and redshift bins, straight to standard output, which is convenient for applications in a scripting environment. CosmoSurvey adopts the standard ΛCDM cosmological model, and its model for structure formation is rooted in the Press-Schechter formalism. It has found application in the evaluation of Monte Carlo Markov Chain (MCMC) engines, and future extensions may find application in modeling the effects of scatter in the mass-observable relations for clusters, redshift evolution in that scatter, and in the effect of point-source contamination of cluster surveys from X-ray luminous Active Galactic Nuclei (AGN).

Chapter 5

Summary

In this work analyze ways of coping with scatter in the mass-observable scaling relationships for clusters of galaxies, and present software components we have developed to aid in this effort.

We began by using a sample of galaxy clusters simulated with cooling and feedback. With this sample, we investigated three substructure statistics and their correlations with temperature and mass offsets from mean scaling relations in the M-$T_{\rm X}$ plane. First, we showed that the substructure statistics w, η, P_{20} and P_{30} all correlate significantly with $\delta \ln T_{\rm X}$, though with non-negligible scatter. In all cases this scatter is larger for $\delta \ln T_{\rm SL}$ than it is for $\delta \ln T_{\rm EW}$. Next, we considered the possibility that M-$T_{\rm X}$ scatter is driven by low-mass clusters. We tested the degree to which scatter can be reduced by filtering out these systems. This consisted of performing a cut at 2 keV, for which we saw that it yielded a modest improvement in mass estimates. To see whether incorporating substructure could refine these mass estimates, we first showed that w, η, P_{20}, and P_{30} correlate significantly with the difference $\delta \ln M$ between masses predicted from the mean $M(T_{\rm X})$ relation and the true cluster masses, with non-negligible scatter that again is less for $M(T_{\rm EW})$ than it is for $M(T_{\rm SL})$. Then we adopted a full three-parameter model, M-$T_{\rm X}$-S, which includes substructure information S estimated using w, η, P_{20}, and P_{30}. Scatter about the basic two-parameter M-$T_{\rm EW}$ relation was 0.094. Including substructure as a third parameter reduced the scatter to 0.072 for centroid variation, 0.084 for axial ratio, 0.081 for P_{20}, and 0.084

for P_{30}. Scatter about the basic two-parameter M-$T_{\rm SL}$ relation was 0.124, and including substructure as a third parameter reduced the scatter to 0.085 for centroid variation, 0.112 for axial ratio, 0.110 for P_{20}, and 0.108 for P_{30}. As one last test, and to increase our confidence that our substructure measures are not relying on potentially non-physical core structure in the simulations, we also repeated the comparison of mass-estimates for $T_{\rm EW}$, with the core regions of the clusters excised. First, removing the core slightly increased the scatter in M-$T_{\rm X}$ possibly by making the average temperature more sensitive to structure outside the core. Second, even with the cores removed the improvement in mass-estimates obtained using substructure information remains. Based on these results, it appears that centroid variation is the best substructure statistic to use when including a substructure correction in the M-$T_{\rm EW}$ relation. However, the correlations we have found in this sample of simulated clusters might not hold in samples of real clusters, because relaxed clusters in the real universe tend to have cooler cores than our simulated clusters do.

Next, we adopted two methods of quantifying temperature inhomogeneity spectroscopically, the temperature ratio $T_{\rm HBR}$ [Mathiesen & Evrard(2001), Cavagnolo et al.(2008)] and the cool residual RES_{cool}. The former is the ratio of a hardband X-ray spectral-fit temperature to a broadband temperature, and becomes greater than 1 for clusters whose ICM contains cool, over-luminous sub-components. The latter is the excess broadband count rate relative to the count rate predicted by a model fit to the hard X-ray band. Though our simulated clusters are typically less massive and have lower temperatures than the *Chandra* archive clusters in [Cavagnolo et al.(2008)], we find that their temperature ratios $T_{\rm HBR}$ occupy generally the same distribution as the observed clusters.

We also looked for an opportunity to combine $T_{\rm HBR}$ and the cool residual with the mean mass-temperature relation to obtain better mass estimates than are achieved just with the scaling relation alone. We find, however, that while both T_{HBR} and the RES_{cool} are correlated with offset from the M-T_{X} relation, these correlations are weak, at least for this sample. We conclude that these measures of temperature inhomogeneity are not very effective at reducing scatter in the mass-temperature relation.

In examining temperature inhomogeneity, we note a particular difficulty that arises when trying to use clusters from hydrodynamic simulations to calibrate scatter-correction observables based on temperature inhomogeneity, such as T_{HBR}. Historically, simulated clusters have tended to exhibit their own kind of "over-cooling problem", in which dense lumps of luminous, cool gas associated with merged sub-halos appear. These cool lumps are often excised from simulated clusters before their global properties are measured, but masking them appears to make the remaining temperature structure of the simulated clusters overly homogeneous. This finding suggests that real clusters may have cooler subcomponents, that are more diffuse and less concentrated than in their simulated counterparts. Some physical process, perhaps thermal conduction, turbulent heat transport [Dennis & Chandran(2005), Parrish et al.(2010), Ruszkowski & Oh(2011)], or a more aggressive form of feedback, prevents cool lumps from forming in real clusters and might not completely eliminate those temperature inhomogeneities. Newer simulations incorporate treatments of conduction and AGN feedback, as well as more accurate treatments of mixing, and it will be interesting to revisit these temperature inhomogeneity measures in simulated clusters when large samples of such simulated clusters become available.

Finally we present the CosmoSurvey software for quickly and efficiently modeling simple flux-limited galaxy cluster surveys on commodity hardware. The software and its library are easily adapted, and can find applications in a variety of settings. It has been used as the basis of the likelihood function in evaluating a Monte Carlo Markov Chain (MCMC) engine, and work is underway to adapt it for evaluating the effects of point-source contamination of flux-limited X-ray surveys, due to Active Galactic Nuclei (AGN). While limited in scope and sophistication, we hope that CosmoSurvey also helps illustrate an effective approach for building small, fast, efficient semi-analytical models using general purpose programming tools.

APPENDICES

Appendix A

CosmoSurvey User Guide

CosmoSurvey comprises a small set of simple tools and functions for modeling large-area survey of galaxy clusters. It is small, simple, and efficient on commodity hardware, and is easily adapted.

A.1 Quick Start

Getting started with CosmoSurvey is simple once a small set of requirements are met. These are laid out in detail in the rest of this user guide. This provides just the highlights, providing a quick path to using the tool for the first time.

A.1.1 Requirements

CosmoSurvey has these requirements.

- A POSIX-compliant operating system such as as Linux, MacOS, or Unix
- A Fortran90 compiler, such as GFortran or the Intel `ifort` compiler
- The PLPlot plotting library

  `http://http://plplot.sourceforge.net/`
- Version 1.6 of the Cuba numerical integration library

  `http://www.feynarts.de/cuba/Cuba-1.6.tar.gz`

A.1.2 Download

CosmoSurvey can be download as a ZIP archive or as a tar.gz archive from the following location.

`http://dventimi.github.com/CosmoSurvey/`

A.1.3 Install

Follow these steps to build and install CosmoSurvey.

- Download and install requirements: PLPlot and Cuba.
- Download the CosmoSurvey archive file.
- Unzip the archive file to any convenient temporary location.
- In CosmoSurvey's top-level directory, run the following commands.

```
./configure
make
make install
```

Note that the last command `make install` probably will need to be run with sufficient permissions. This can be achieved in a variety of ways, such as logging in as or changing to a "super-user" account, or by running `sudo make install`.

A.1.4 Run

Running CosmoSurvey evaluates the model for a given set of cosmological, cluster, and survey parameters. It then emits to standard output a list of numbers that represent galaxy cluster number counts in observable bins. Parameters may be supplied on the command line, though they are optional since there are a set of default values. For example, simply running from the command line

```
cosmosurvey
```

Produces this output

```
48926.125

10116.227

1412.8425

120.24377

5.5203319

...

1.55754946E-03
```

The number counts emitted serially correspond to number counts in observable bins N_{ij}, for i bins in redshift z and j bins in log luminosity $\ln L$. Essentially, it is a matrix of observables with rows for redshift and columns for luminosity, and unrolled into a flat list in a column-first order.

A.2 Simulating A Survey

As discussed above, simulating a survey, evaluating it at a given set of parameters θ_i, and emitting the observables to standard is the primary function of CosmoSurvey. The relevant input parameters are as follows, with the default values in parentheses.

```
-z1  (0.01)       Redshift start
```

```
-z2  (2.50)       Redshift end

-nz  (10)         Number of redshift bins

-l1  (44.0)       log10(L1) luminosity start, [L1] = ergs/s

-l2  (46.0)       log10(L2) luminosity end, [L2] = ergs/s

-nl  (10)         Number of luminosity bins

-do  (12.0)       Survey solid angle dOmega, [dOmega] = steradians

-fl  (1.25e-13)   Survey flux limit, [fl] = ergs/s/cm^2

-w   (-1.0)       Dark Energy equation of state parameter w

-om  (0.30)       Matter density parameter Omega_M

-ol  (0.70)       Dark Energy density parameter Omega_Lambda

-s8  (0.80)       Power spectrum normalization sigma_8

-g   (0.55)       Linder growth index gamma
```

A.3 Visualizing A Survey

While the `cosmosurvey` program itself probably is the most useful insofar as it can be adapted to other uses, such as integration into a Monte Carlo Markov Chain (MCMC) engine, it sometimes is helpful to visualize survey observables. Of course the output of `cosmosurvey`, being a series of numbers to standard out, can be plotted in any number of plotting tools (e.g., GNUplot, SuperMongo, and R). However, as a convenience the results of a survey can be plotted directly, using the `cosmoplot` program. The `cosmoplot` program takes the same set of cosmological, cluster, and survey parameters as the `cosmosurvey` program does. However, it also prompts the user for an output device, so that the plot can be displayed directly to the user or written out to a file in a variety of formats (e.g., SVG, JPEG, GIF, PostScript, and PDF). The output is displayed as a three-dimensional plot, with redshift bins in z along one horizontal axis, log luminosity bins along the other horizontal axis, and galaxy cluster number counts along the vertical axis. An example of its output for the same set of default parameters that `cosmosurvey` uses appears in figure A.1.

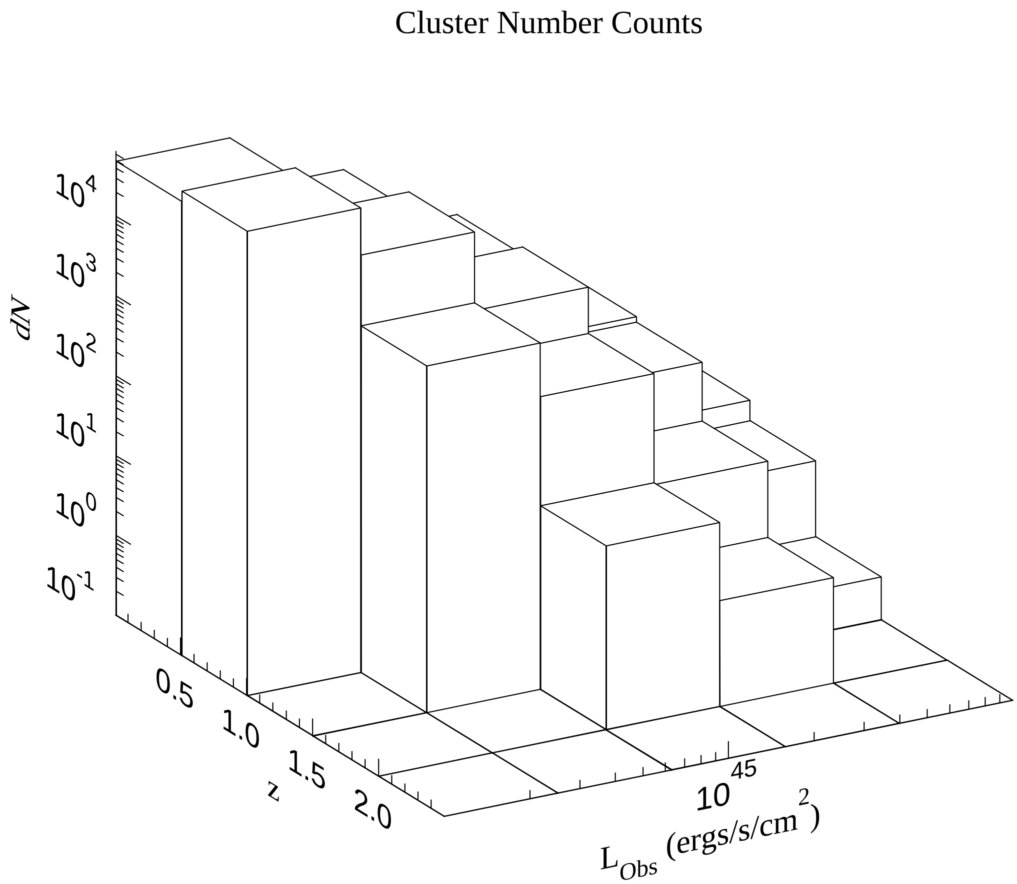

Figure A.1: CosmoSurvey simulated cluster survey counts in observable bins, obtained using the cosmoplot program.

A.4 Fortran API

The Fortran API comprises six Fortran95 modules. Along with programs, modules are the primary unit for code packaging and re-use in Fortran95. The CosmoSurvey packages are `quadpack`, `quadrature`, `utils`, `constants`, `cosmology`, and `structure`.

A.4.1 quadpack

The `quadpack` module is a Fortran 90 port of a Fortran 77 library for numerical integration of one-dimensional functions, and is in the public domain. The Fortran 77 version of the integration sub-programs are available on Netlib, a repository of software for scientific computing maintained by AT&T, Bell Laboratories, the University of Tennessee, and Oak Ridge National Laboratory.

A.4.2 quadrature

The `quadrature` module is an adapter for the one-dimensional integrators in the `quadpack` module and the multi-dimensional integrators in the `Cuba` library.

A.4.3 utils

The `utils` module is an assortment of "helper" functions that are optional and operate outside of the core CosmoSurvey functionality.

A.4.3.1 Subprograms

`hist3d` *dist x1 x2 y1 y2 file floor*: This is a subroutine that writes out the two-dimensional floating-point array *dist* to *file* in a format suitable for the 3-D histogram plotting functions in `GNUPlot`. The parameters *x1*, *x2*, *y1*, and *y2* define the range of the resulting plot data.

`isoline` *iso x1 x2 y1 y2 file i floor*: This is a subroutine that generates a GNUPlot-compatible isoline from one row of data in row *i* of the data in *iso*. The parameters *x1*, *x2*, *y1*, and *y2* define the range of the resulting plot data. The data are written out to *file*. The parameter *floor* represents the lowest value in the plot.

`hist_3d` *x y z*: This is a subroutine that regrids multi-dimensional data in z into bins, in a format compatible with the PLPlot plotting library. The parameters x and y are one-dimensional arrays representing the two independent coordinates.

`f_nvpair` *name*:

`f_split` *string char*:

`f_records` *filename*:

`f_record_count` *fu*:

`json_matrix` *m unit*:

A.4.4 constants

A.4.4.1 Data

A.4.5 cosmology

A.4.5.1 Subprograms

`f_lcdm` :

`f_lcdm_priors` :

`f_lcdm_names` :

`f_E` *z*:

$$E(z) = \sqrt{\Omega_M(1+z)^3 + \Omega_\Lambda(1+z)^{3(1+w)}} \tag{A.1}$$

`f_dr_dz` *z argv*:

$$\frac{dr}{dz} = \frac{c}{H(z)} \tag{A.2}$$

`f_r` *z1 z2*:

$$r = \int_{z_1}^{z_2} \frac{dr}{dz} dz' \tag{A.3}$$

`f_dV_dOmega_dz` *z argv*:

$$\frac{dV}{dz\, d\Omega} = \frac{r^2(z)}{H(z)} \tag{A.4}$$

`f_dV` *z1 z2 dOmega*:

$$V = \int_{z_1}^{z_2} \frac{dV}{dz\, d\Omega}\, dz'\, d\Omega \tag{A.5}$$

`f_Omega_M` *z*:

$$\Omega_M = \frac{\Omega_{M_0}(1+z)^3}{E^2(z)} \tag{A.6}$$

`f_Omega_lambda` z:

$$\Omega_\Lambda = \frac{1 - \Omega_{M_0}}{E^2(z)} \tag{A.7}$$

`f_D` z:

$$D = r(z) \tag{A.8}$$

`f_D_L` z:

$$D_L = (1+z)D(z) \tag{A.9}$$

A.4.6 structure

`f_Integrand_Linder`

$$\frac{dG}{dz} = \frac{\Omega_M(z)^{\gamma-1}}{1+z} \tag{A.10}$$

`f_G`

$$G(z) = \int_{z_1}^{z_2} \frac{dG}{dz} \tag{A.11}$$

`f_ln_inv_sigma`

$$\ln \sigma^{-1} = ax + bx^2 - \ln g(z) - \ln \frac{\sigma_8}{0.3} \tag{A.12}$$

`f_alpha_eff`

$$\alpha_{\texttt{eff}} = a + 2bx \tag{A.13}$$

`f_mass_fraction`

$$f(\ln \sigma^{-1}) = a \exp(-|\ln \sigma^{-1} + b|^\epsilon) \tag{A.14}$$

f_dN_dV_dmu

$$\frac{dN}{dV\,d\mu} = \Omega_M(z)\frac{\rho_c}{M}\,\alpha_{\texttt{eff}}(M)\,f(\ln\sigma^{-1}(M,z)) \tag{A.15}$$

f_tau_of_mu

$$\tau(\mu) = \tau_0 + \alpha\,\mu + \alpha\,\ln(E(z)) \tag{A.16}$$

f_dtau_dmu

$$\frac{d\mu}{d\tau} = \alpha \tag{A.17}$$

f_lambda_of_mu

$$\lambda(\mu) = \lambda_0 + \mu^\beta + \log E(z)^2 \tag{A.18}$$

f_mu_of_lambda

$$\mu(\lambda) = \lambda - \lambda_0 - \frac{\log E(z)^2}{\beta} \tag{A.19}$$

f_Cov

$$\mathbf{\Sigma} = \begin{pmatrix} \sigma_\tau\,\sigma_\tau & \rho\,\sigma_\tau\,\sigma_\lambda \\ \rho\,\sigma_\lambda\,\sigma_\tau & \sigma_\lambda\,\sigma_\lambda \end{pmatrix} \tag{A.20}$$

f_C_det

$$|\mathbf{\Sigma}|^{-1} = \mathbf{\Sigma}_{11}\,\mathbf{\Sigma}_{22} - \mathbf{\Sigma}_{12}\,\mathbf{\Sigma}_{21} \tag{A.21}$$

f_luminosity

$$L = 4\,\pi\,D_L(z)^2\,f \tag{A.22}$$

Appendix B

CosmoFisher Installation Guide

CosmoFisher comprises a small set of simple tools and functions for computing and working with Fisher Information matrices for a numerical model.

B.1 CosmoFisher Quick Start

Getting started with CosmoFisher is simple once a small set of requirements are met. These are laid out in detail in the rest of this user guide. This provides just the highlights, providing a quick path to using the tool for the first time.

B.1.1 Requirements

CosmoFisher has these requirements.

- A POSIX-compliant operating system such as as Linux, MacOS, or Unix
- The Python language interpreter
- The Numdifftools differentiation library

  `http://pypi.python.org/pypi/Numdifftools/0.3.1`
- The SciPy scientific analysis library

  `http://www.scipy.org/`

- The MatPlotLib plotting library `http://matplotlib.sourceforge.net/`

B.1.2 Download

CosmoFisher can be download as a ZIP archive or as a tar.gz archive from the following location.

`http://dventimi.github.com/CosmoFisher/`

B.1.3 Install

Follow these steps to build and install CosmoFisher.

- Download and install requirements: Python, NumDiffTools, SciPy, and MatPlotLib. x
- Download the CosmoFisher archive file.
- Unzip the archive file to any convenient temporary location.
- In CosmoFisher's top-level directory, run the following commands.

```
./configure
make
make install
```

Note that the last command `make install` probably will need to be run with sufficient permissions. This can be achieved in a variety of ways, such as logging in as or changing to a "super-user" account, or by running `sudo make install`.

BIBLIOGRAPHY

BIBLIOGRAPHY

[Abell(1958)] Abell, G. O. 1958, ApJ, 3, 211

[Arnaud(1996)] Arnaud, K. A. 1996, in Astronomical Society of the Pacific Conference Series, Vol. 101, Astronomical Data Analysis Software and Systems V, ed. G. H. Jacoby & J. Barnes, 17–+

[Borgani(2004)] Borgani, S. 2004, Astrophysics and Space Science, 294, 51

[Borgani & Kravtsov(2009)] Borgani, S., & Kravtsov, A. 2009, ArXiv e-prints

[Borgani et al.(2004)] Borgani, S., Murante, G., Springel, V., Diaferio, A., Dolag, K., Moscardini, L., Tormen, G., Tornatore, L., & Tozzi, P. 2004, MNRAS, 348, 1078

[Buote & Tsai(1995)] Buote, D. A., & Tsai, J. C. 1995, ApJ, 452, 522

[Buote & Tsai(1995)] Buote, D. A., & Tsai, J. C. 1995, Astrophysical Journal, 452, 522

[Cavagnolo et al.(2008)] Cavagnolo, K. W., Donahue, M., Voit, G. M., & Sun, M. 2008, Astrophysical Journal, 682, 821

[Cunha & Evrard(2010)] Cunha, C. E., & Evrard, A. E. 2010, Phys. Rev. D, 81, 083509

[Dennis & Chandran(2005)] Dennis, T. J., & Chandran, B. D. G. 2005, ApJ, 622, 205

[DES(2012)] DES. 2012, The Dark Energy Survey, http://www.darkenergysurvey.org

[Dolag & Stasyszyn(2009)] Dolag, K., & Stasyszyn, F. 2009, MNRAS, 398, 1678

[Eisenstein et al.(2005)] Eisenstein, D. J., Zehavi, I., Hogg, D. W., Scoccimarro, R., Blanton, M. R., Nichol, R. C., Scranton, R., Seo, H., Tegmark, M., Zheng, Z., Anderson, S. F., Annis, J., Bahcall, N., Brinkmann, J., Burles, S., Castander, F. J., Connolly, A., Csabai, I., Doi, M., Fukugita, M., Frieman, J. A., Glazebrook, K., Gunn, J. E., Hendry, J. S., Hennessy, G., Ivezi, Z., Kent, S., Knapp, G. R., Lin, H., Loh, Y., Lupton, R. H., Margon, B., McKay, T. A., Meiksin, A., Munn, J. A., Pope, A., Richmond, M. W., Schlegel, D., Schneider, D. P., Shimasaku, K., Stoughton, C., Strauss, M. A., SubbaRao, M., Szalay,

A. S., Szapudi, I., Tucker, D. L., Yanny, B., & York, D. G. 2005, Astrophysical Journal, 633, 560

[Evrard et al.(2008)] Evrard, A. E., Bialek, J., Busha, M., White, M., Habib, S., Heitmann, K., Warren, M., Rasia, E., Tormen, G., Moscardini, L., Power, C., Jenkins, A. R., Gao, L., Frenk, C. S., Springel, V., White, S. D. M., & Diemand, J. 2008, ApJ, 672, 122

[Evrard et al.(1993)] Evrard, A. E., Mohr, J. J., Fabricant, D. G., & Geller, M. J. 1993, ApJ, 419, L9

[Fabian et al.(1994)] Fabian, A. C., Crawford, C. S., Edge, A. C., & Mushotzky, R. F. 1994, MNRAS, 267, 779

[Fabjan et al.(2011)] Fabjan, D., Borgani, S., Rasia, E., Bonafede, A., Dolag, K., Murante, G., & Tornatore, L. 2011, MNRAS, 416, 801

[Forman et al.(1972)] Forman, W., Kellogg, E., Gursky, H., Tananbaum, H., & Giacconi, R. 1972, ApJ, 178, 309

[Frieman et al.(2008)] Frieman, J. A., Turner, M. S., & Huterer, D. 2008, Annual Review of Astronomy and Astrophysics, 46, 385

[Fruscione et al.(2006)] Fruscione, A., McDowell, J. C., Allen, G. E., Brickhouse, N. S., Burke, D. J., Davis, J. E., Durham, N., Elvis, M., Galle, E. C., Harris, D. E., Huenemoerder, D. P., Houck, J. C., Ishibashi, B., Karovska, M., Nicastro, F., Noble, M. S., Nowak, M. A., Primini, F. A., Siemiginowska, A., Smith, R. K., & Wise, M. 2006, in CIAO: Chandra's data analysis system, Vol. 6270, 60

[Gardini et al.(2004)] Gardini, A., Rasia, E., Mazzotta, P., Tormen, G., Grandi, S. D., & Moscardini, L. 2004, Monthly Notices of the Royal Astronomical Society, 351, 505

[Hu(2003)] Hu, W. 2003, Phys. Rev. D, 67, 081304

[Jeltema et al.(2008)] Jeltema, T. E., Hallman, E. J., Burns, J. O., & Motl, P. M. 2008, ApJ, 681, 167

[Jeltema et al.(2008)] Jeltema, T. E., Hallman, E. J., Burns, J. O., & Motl, P. M. 2008, Astrophysical Journal, 681, 167

[Jenkins et al.(2001)] Jenkins, A., Frenk, C. S., White, S. D. M., Colberg, J. M., Cole, S., Evrard, A. E., Couchman, H. M. P., & Yoshida, N. 2001, MNRAS, 321, 372

[Kaiser(1986)] Kaiser, N. 1986, MNRAS, 222, 323

[Kaiser(1986)] Kaiser, N. 1986, Monthly Notices of the Royal Astronomical Society, 222, 323

[Kay et al.(2007)] Kay, S. T., da Silva, A. C., Aghanim, N., Blanchard, A., Liddle, A. R., Puget, J.-L., Sadat, R., & Thomas, P. A. 2007, MNRAS, 377, 317

[Kravtsov et al.(2006)] Kravtsov, A. V., Vikhlinin, A., & Nagai, D. 2006, ApJ, 650, 128

[Kravtsov et al.(2006)] Kravtsov, A. V., Vikhlinin, A., & Nagai, D. 2006, Astrophysical Journal, 650, 128

[Levine et al.(2002)] Levine, E. S., Schulz, A. E., & White, M. 2002, ApJ, 577, 569

[Lima & Hu(2005)] Lima, M., & Hu, W. 2005, Phys. Rev. D, 72, 043006

[Lima & Hu(2005)] Lima, M., & Hu, W. 2005, Physical Review D, 72, 43006

[Linder(2005)] Linder, E. V. 2005, Phys. Rev. D, 72, 043529

[Longair(2008)] Longair, M. 2008, Galaxy Formation, Astronomy and Astrophysics Library (Springer)

[LSST(2012)] LSST. 2012, LSST, http://www.lsst.org/lsst/scibook

[Majumdar & Mohr(2004)] Majumdar, S., & Mohr, J. J. 2004, ApJ, 613, 41

[Mantz et al.(2010)] Mantz, A., Allen, S. W., Rapetti, D., & Ebeling, H. 2010, MNRAS, 406, 1759

[Mathiesen & Evrard(2001)] Mathiesen, B. F., & Evrard, A. E. 2001, ApJ, 546, 100

[Mathiesen & Evrard(2001)] Mathiesen, B. F., & Evrard, A. E. 2001, Astrophysical Journal, 546, 100

[Mazzotta et al.(2004)] Mazzotta, P., Rasia, E., Moscardini, L., & Tormen, G. 2004, MNRAS, 354, 10

[Merloni et al.(2012)] Merloni, A., Predehl, P., Becker, W., Böhringer, H., Boller, T., Brunner, H., Brusa, M., Dennerl, K., Freyberg, M., Friedrich, P., Georgakakis, A., Haberl, F., Hasinger, G., Meidinger, N., Mohr, J., Nandra, K., Rau, A., Reiprich, T. H., Robrade, J., Salvato, M., Santangelo, A., Sasaki, M., Schwope, A., Wilms, J., & German eROSITA Consortium, t. 2012, ArXiv e-prints

[Mohr & Evrard(1997)] Mohr, J. J., & Evrard, A. E. 1997, Astrophysical Journal, 491, 38

[Mohr et al.(1993)] Mohr, J. J., Fabricant, D. G., & Geller, M. J. 1993, Astrophysical Journal, 413, 492

[Nagai et al.(2007)] Nagai, D., Kravtsov, A. V., & Vikhlinin, A. 2007, ApJ, 668, 1

[Nagai et al.(2007)] Nagai, D., Kravtsov, A. V., & Vikhlinin, A. 2007, Astrophysical Journal, 668, 1

[Navarro et al.(1995)] Navarro, J. F., Frenk, C. S., & White, S. D. M. 1995, MNRAS, 275, 720

[Navarro et al.(1995)] Navarro, J. F., Frenk, C. S., & White, S. D. M. 1995, Monthly Notices of the Royal Astronomical Society, 275, 720

[Norman & Bryan(1999)] Norman, M. L., & Bryan, G. L. 1999, in Cosmological Adaptive Mesh RefinementCD, Vol. 240, 19

[O'Hara et al.(2006a)] O'Hara, T. B., Mohr, J. J., Bialek, J. J., & Evrard, A. E. 2006a, ApJ, 639, 64

[O'Hara et al.(2006b)] O'Hara, T. B., Mohr, J. J., Bialek, J. J., & Evrard, A. E. 2006b, Astrophysical Journal, 639, 64

[O'Shea et al.(2004)] O'Shea, B. W., Bryan, G., Bordner, J., Norman, M. L., Abel, T., Harkness, R., & Kritsuk, A. 2004, Introducing Enzo, an AMR Cosmology Application, http://adsabs.harvard.edu/abs/2004astro.ph..3044O

[PanSTARRS(2012)] PanSTARRS. 2012, Pan-STARRS, http://pan-starrs.ifa.hawaii.edu

[Parrish et al.(2010)] Parrish, I. J., Quataert, E., & Sharma, P. 2010, ApJ, 712, L194

[Pearce et al.(1994)] Pearce, F. R., Thomas, P. A., & Couchman, H. M. P. 1994, MNRAS, 268, 953

[Perlmutter et al.(1999)] Perlmutter, S., Aldering, G., Goldhaber, G., Knop, R. A., Nugent, P., Castro, P. G., Deustua, S., Fabbro, S., Goobar, A., Groom, D. E., Hook, I. M., Kim, A. G., Kim, M. Y., Lee, J. C., Nunes, N. J., Pain, R., Pennypacker, C. R., Quimby, R., Lidman, C., Ellis, R. S., Irwin, M., McMahon, R. G., Ruiz-Lapuente, P., Walton, N., Schaefer, B., Boyle, B. J., Filippenko, A. V., Matheson, T., Fruchter, A. S., Panagia, N., Newberg, H. J. M., Couch, W. J., & Project, T. S. C. 1999, Astrophysical Journal, 517, 565

[Phillips(1993)] Phillips, M. M. 1993, ApJ, 413, L105

[Piffaretti & Valdarnini(2008)] Piffaretti, R., & Valdarnini, R. 2008, A&A, 491, 71

[Poole et al.(2007)] Poole, G. B., Babul, A., McCarthy, I. G., Fardal, M. A., Bildfell, C. J., Quinn, T., & Mahdavi, A. 2007, MNRAS, 380, 437

[Press & Schechter(1974)] Press, W. H., & Schechter, P. 1974, ApJ, 187, 425

[Rasia et al.(2006)] Rasia, E., Ettori, S., Moscardini, L., Mazzotta, P., Borgani, S., Dolag, K., Tormen, G., Cheng, L. M., & Diaferio, A. 2006, MNRAS, 369, 2013

[Rasia et al.(2008)] Rasia, E., Mazzotta, P., Bourdin, H., Borgani, S., Tornatore, L., Ettori, S., Dolag, K., & Moscardini, L. 2008, Astrophysical Journal, 674, 728

[Rasia et al.(2012)] Rasia, E., Meneghetti, M., Martino, R., Borgani, S., Bonafede, A., Dolag, K., Ettori, S., Fabjan, D., Giocoli, C., Mazzotta, P., Merten, J., Radovich, M., & Tornatore, L. 2012, ArXiv e-prints

[Riess et al.(1998)] Riess, A. G., Filippenko, A. V., Challis, P., Clocchiatti, A., Diercks, A., Garnavich, P. M., Gilliland, R. L., Hogan, C. J., Jha, S., Kirshner, R. P., Leibundgut, B., Phillips, M. M., Reiss, D., Schmidt, B. P., Schommer, R. A., Smith, R. C., Spyromilio, J., Stubbs, C., Suntzeff, N. B., & Tonry, J. 1998, Astronomical Journal, 116, 1009

[Riess et al.(1996)] Riess, A. G., Press, W. H., & Kirshner, R. P. 1996, ApJ, 473, 88

[Ruszkowski & Oh(2011)] Ruszkowski, M., & Oh, S. P. 2011, MNRAS, 414, 1493

[Song et al.(2012)] Song, J., Zenteno, A., Stalder, B., Desai, S., Bleem, L. E., Aird, K. A., Armstrong, R., Ashby, M. L. N., Bayliss, M., Bazin, G., Benson, B. A., Bertin, E., Brodwin, M., Carlstrom, J. E., Chang, C. L., Cho, H. M., Clocchiatti, A., Crawford, T. M., Crites, A. T., de Haan, T., Dobbs, M. A., Dudley, J. P., Foley, R. J., George, E. M., Gettings, D., Gladders, M. D., Gonzalez, A. H., Halverson, N. W., Harrington,

N. L., High, F. W., Holder, G. P., Holzapfel, W. L., Hoover, S., Hrubes, J. D., Joy, M., Keisler, R., Knox, L., Lee, A. T., Leitch, E. M., Liu, J., Lueker, M., Luong-Van, D., Marrone, D. P., McDonald, M., McMahon, J. J., Mehl, J., Meyer, S. S., Mocanu, L., Mohr, J. J., Montroy, T. E., Natoli, T., Nurgaliev, D., Padin, S., Plagge, T., Pryke, C., Reichardt, C. L., Rest, A., Ruel, J., Ruhl, J. E., Saliwanchik, B. R., Saro, A., Sayre, J. T., Schaffer, K. K., Shaw, L., Shirokoff, E., Suhada, R., Spieler, H. G., Stanford, S. A., Staniszewski, Z., Stark, A. A., Story, K., Stubbs, C. W., van Engelen, A., Vanderlinde, K., Vieira, J. D., Williamson, R., & Zahn, O. 2012, ArXiv e-prints

[Springel(2005)] Springel, V. 2005, Monthly Notices of the Royal Astronomical Society, 364, 1105

[Springel(2005)] Springel, V. 2005, MNRAS, 364, 1105

[Stanek et al.(2010)] Stanek, R., Rasia, E., Evrard, A. E., Pearce, F., & Gazzola, L. 2010, ApJ, 715, 1508

[Tormen(1997)] Tormen, G. 1997, Monthly Notices of the Royal Astronomical Society, 290, 411

[Tormen(1997)] Tormen, G. 1997, MNRAS, 290, 411

[Tornatore et al.(2003)] Tornatore, L., Borgani, S., Springel, V., Matteucci, F., Menci, N., & Murante, G. 2003, MNRAS, 342, 1025

[Valdarnini(2006)] Valdarnini, R. 2006, New A, 12, 71

[Ventimiglia et al.(2008)] Ventimiglia, D. A., Voit, G. M., Donahue, M., & Ameglio, S. 2008, Astrophysical Journal, 685, 118

[Ventimiglia et al.(2012)] Ventimiglia, D. A., Voit, G. M., & Rasia, E. 2012, ApJ, 747, 123

[Vikhlinin(2006)] Vikhlinin, A. 2006, ApJ, 640, 710

[Vikhlinin et al.(2009)] Vikhlinin, A., Kravtsov, A. V., Burenin, R. A., Ebeling, H., Forman, W. R., Hornstrup, A., Jones, C., Murray, S. S., Nagai, D., Quintana, H., & Voevodkin, A. 2009, Astrophysical Journal, 692, 1060

[Voit(2005)] Voit, G. M. 2005, Reviews of Modern Physics, 77, 207

[Voit(2005)] Voit, G. M. 2005, Reviews of Modern Physics, 77, 207

[Wang & Steinhardt(1998)] Wang, L., & Steinhardt, P. J. 1998, ApJ, 508, 483

[Yang et al.(2009)] Yang, H. K., Ricker, P. M., & Sutter, P. M. 2009, Astrophysical Journal, 699, 315